JSCSEN 73(11)1021–1138(2008)

Journal of the Serbian Chemical Society

Electronic version

VOLUME 73

NO 11

BELGRADE 2008

Available on line at

www.shd.org.rs/JSCS

The full search of JSCS is available through

DOAJ DIRECTORY OF OPEN ACCESS JOURNALS

www.doaj.org

Journal of the Serbian Chemical Society
JSCS@tmf.bg.ac.yu • www.shd.org.yu/JSCS

J. Serb. Chem. Soc. Vol. 73, No. 11 (2008)

CONTENTS

Published by the Serbian Chemical Society
Karnegijeva 4/III, 11000 Belgrade, Serbia
Printed by the Faculty of Technology and Metallurgy
Karnegijeva 4, P.O. Box 35-03, 11120 Belgrade, Serbia

www.shd.org.rs

Journal of the Serbian Chemical Society

JSCS@tmf.bg.ac.yu • www.shd.org.rs/JSCS

J. Serb. Chem. Soc. 73 (11) 1021–1025 (2008) UDC **P. falciparum*:546.174+547.567:615.281
JSCS–3783 *Original scientific paper*

Ribofuranose as a carrier of tetraoxane and 4-aminoquinoline antimalarial pharmacophores

IGOR M. OPSENICA[1#], KIRSTEN K. SMITH[2], LUCIA GERENA[2], SANDRA GAICA[3] and BOGDAN A. ŠOLAJA[1*#]

[1]*Faculty of Chemistry, University of Belgrade, Studentski trg 16, P.O. Box 158,11001 Belgrade, Serbia,* [2]*Division of Experimental Therapeutics, Walter Reed Army Institute of Research, Washington, DC 20307-5100, USA and* [3]*Institute of Chemistry, Technology and Metallurgy, Njegoševa 12, 11000 Belgrade, Serbia*

(Received 13 February 2008)

Abstract: Several tetraoxane and 4-aminoquinoline molecules were prepared in order to examine the influence of ribofuranose as a carrier molecule on the antimalarial activity of test compounds. The synthesized compounds showed pronounced antimalarial activity against *Plasmodium falciparum* chloroquine susceptible D6, chloroquine resistant W2 and multidrug-resistant TM91C235 (Thailand) strains. The aminoquinoline derivative **4** was more active against W2 and TM91C235 strains than the control compounds (CQ and MFQ).

Keywords: tetraoxanes; 4-aminoquinolines; malaria; *P. falciparum*.

INTRODUCTION

Malaria is an infectious disease that affects more than 500 million people per annum, causing approximately two million deaths.[1] It is most common in tropical and subtropical areas and 90 % of all cases are found in sub-Saharan Africa. Antimalarial drug resistance, particularly the widespread resistance of many *Plasmodium falciparum* strains to most readily available drugs, such as chloroquine (CQ), hinders malaria control and is therefore a major public health problem. Resistance to antimalarial drugs has increased the global cost of controlling the disease. So far, no resistance to artemisinin (ART) or ART derivatives has been reported. Resistance, as well as the absence of a vaccine for protection against malaria causes an urgent need for new effective, safe and affordable drugs.

Following previous results,[2] new tetraoxanes and 4-aminoquinoline molecules with ribofuranose as carrier molecules were synthesized. The synthesized tetraoxanes were screened *in vitro* against three *P. falciparum* strains: D6 (chloro-

* Corresponding author. E-mail: bsolaja@chem.bg.ac.yu
# Serbian Chemical Society member.
doi: 10.2298/JSC0811021O

quine-susceptible), W2 (chloroquine-resistant), and TM91C235, a multidrug-resistant strain.

RESULTS AND DISCUSSION

Chemistry

Methyl 2,3-*O*-isopropylidene-D-ribofuranoside **2** was prepared from D-ribose using a mixture of acetone/methanol and HCl (Scheme 1). Compound **2** was isolated in 64 % yield as a mixture of α- and β-anomers, and was pure enough to be used directly in the subsequent step. Oxidation using pyridinium chlorochromate (PCC) afforded the aldehyde **3**, which was further transformed into amine **4** by reductive amination. Amine **4** was isolated as the salt **5** and after treatment with 1.0 % NaOH, the free amine was obtained.

The synthesis of the tetraoxane derivative was accomplished starting from ester **6**, which was hydrolyzed into acid **7** in 88 % yield, followed by further transformation *via* a mixed anhydride procedure into the corresponding ester **8** in 82 % yield.

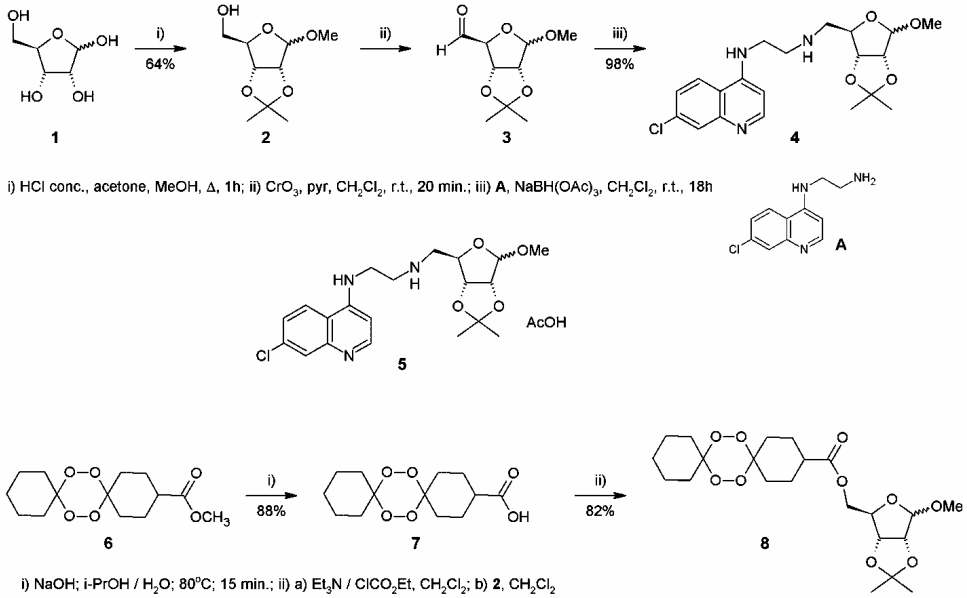

Scheme 1.

Antimalarial activity

The synthesized compounds were screened *in vitro* against three *P. falciparum* strains: D6 (chloroquine and mefloquine (MFQ) susceptible strain), W2 (chloroquine-resistant, MFQ susceptible), and TM91C235 (multidrug-resistant strain) following the protocol given in the literature (Table I).[2b]

TABLE I. *In vitro* antimalarial activities of tetraoxanes **4**–**8** against *P. falciparum* D6,[a] W2,[b] and TM91C235[c] strains

Compound	IC_{50} / nM			IC_{90} / nM		
	D6	W2	TM91C235	D6	W2	TM91C235
4	40.37	141.35	58.25	72.77	232.96	134.45
5	40.03	176.82	61.39	76.77	282.75	127.99
8	115.97	599.23	701.38	405.63	1454.42	2286.79
6	29.20	40.41	26.96	83.92	62.48	110.22
MFQ[d]	7.38	4.99	51.92	16.83	11.28	102.47
CQ[d]	13.62	371.65	178.07	19.89	662.35	391.42

[a]*P. falciparum* African D6 clone; [b]*P. falciparum* Indochina W2 clone; [c]*P. falciparum* multidrug resistant TM91C23 strain (Thailand); [d]control compounds

The synthesized aminoquinoline derivatives **4** and **5** had similar activity; the amine **4** was less active against *P. falciparum* strain D6 in comparison to the controls CQ and MFQ. Compound **4** was 2.5−3 times more active than CQ against W2 and TM91C235 strains.

On the other hand, the tetraoxane **8** was less active than CQ and MFQ, and significantly less active than the corresponding ester **6** against the three *P. falciparum* strains. According to these results, it is suggested that increased polarity of molecule, caused by hydrolysis of the isopropylidene and/or methoxy group in the *in vitro* test may be the cause of the observed small activity. Increasing the polarity of the molecules impedes their transport through biological membranes. In addition, the presence of hydroxy groups can cause facilitated secretion as a consequence of phase II metabolism.

EXPERIMENTAL

For general remarks, see references 2a, 2b, and 2c.

ESI–MS spectra of the synthesized compounds were recorded on an Agilent Technologies 6210 Time-of-Flight LC/MS instrument in the positive ion mode using CH_3CN/H_2O = 1/1 with 0.20 % HCOOH as the carrying solvent solution. The samples were dissolved in pure acetonitrile (HPLC grade). The selected values were as follows: capillary voltage 4 kV; gas temperature 350 °C; drying gas 12 L min^{-1}; nebulizer pressure 45 atm; fragmentator voltage: 70 V.

Methyl 2,3-*O*-isopropylidene-D-ribofuranoside,[3] 7,8,15,16-tetraoxadispiro[5.2.5.2]hexadecane-3-carboxylic acid,[4] N^1-(7-chloroquinolin-4-yl)-ethane-1,2-diamine[5] were prepared according to known procedures.

*N[1]-(7-Chloro-4-quinolinyl)-1,2-ethanediamine-*N[2]*-{[(3*aS*,4*R*,6a*S*)-6-methoxy-2,2--dimethyltetrahydrofuro[3,4-*d*][1,3]dioxol-4-yl]methyl} (4)*

Anhydrous CrO_3 (1.02 g) was suspended in dry CH_2Cl_2 (25 mL) and pyridine (1.65 mL). The alcohol **2** (170 mg, 0.830 mmol) in anhydrous CH_2Cl_2 (2.0 mL) was added after 15 min into the resultant red solution and the reaction mixture was stirred for 20 min. Then the mixture was poured onto cold saturated aqueous $NaHCO_3$. The organic layer was separated and the aqueous layer was extracted with CH_2Cl_2 (2×20 mL). The combined organic layers were

dried (Na_2SO_4) and the solvent evaporated. The crude product was purified by dry-flash chromatography, eluent CH_2Cl_2, to afford the known[6] aldehyde **3** (160 mg, 95.0 %).

Sodium triacetoxyborohydride (168 mg, 0.790 mmol) was added to a mixture of aldehyde (80 mg, 0.39 mmol) and amine **A** (175 mg, 0.790 mmol) in CH_2Cl_2 (20 mL) and the reaction mixture was stirred at room temperature for 18 h. The reaction mixture was poured onto 1.0 % NaOH (20 mL) and extracted with CH_2Cl_2 (2×50 mL). The combined organic layers were dried over anh. Na_2SO_4 and evaporated to dryness. The crude product was purified by dry-flash chromatography, eluent EtOAc/MeOH = 9/1. Yield: 156 mg (98.0 %). Oil. **4**: IR (KBr, cm^{-1}): 3302*w*, 2936*w*, 2361*w*, 1611*w*, 1580*s*, 1535*w*, 1451*m*, 1371*m*, 1331*w*, 1274*w*, 1239*w*, 1209*m*, 1158*m*, 1105*s*, 962*m*; ^{1}H-NMR (200 MHz, $CDCl_3$, δ / ppm): 8.52 (*m*, H–C(2')), 7.95 (*m*, H–C(5')), 7.75 (*m*, H–C(8')), 7.34 (*m*, H–C(6')), 6.38 (*m*, H–C(3')), 5.92 (1H, *bs*), 4.62 (2H, *m*), 4.33 (1H, *m*), 3.32 (5H, *m*), 3.06 (2H, *m*), 2.79 (2H, *d*), 1.97 (2H, *bs*), 1.49 (3H, *s*), 1.31 (3H, *s*); ^{13}C-NMR (50 MHz, $CDCl_3$, δ / ppm): 151.99, 149.87, 149.05, 134.83, 128.62, 125.23, 121.28, 116.23, 112.47, 109.74, 99.16, 86.05, 85.30, 82.61, 55.15, 52.15, 47.12, 41.89, 26.44, 24.87; (+)ESI–HRMS (*m*/*z*, %): 408.18229 ([M+H]$^+$, 100); calculated 408.16845.

*(3*aS*,4*R*,6*aS*)-6-Methoxy-2,2-dimethyltetrahydrofuro[3,4-*d*][1,3]dioxol-4-yl]methyl 7,8,15,16-tetraoxadispiro[5.2.5.2]hexadecane-3-carboxylate (**8**)*

A solution of carboxylic acid **7** (120 mg, 0.440 mmol) in dry CH_2Cl_2 (15 mL) was stirred for 90 min at room temperature upon adding Et_3N (61.4 μL, 0.440 mmol) and $ClCO_2Et$ (42.1 μL, 0.440 mmol). Then a solution of alcohol **2** (90 mg, 0.44 mmol) in dry CH_2Cl_2 (5.0 mL) and a catalytic amount of DMAP (5.0 mg) were added. After 120 min, the reaction mixture was diluted with H_2O, the layers were separated and the organic layer was washed with brine, dried over anh. Na_2SO_4 and evaporated to dryness. The crude product was purified by dry-flash chromatography, eluent: hexane/EtOAc (9/1). Yield: 165 mg (82.0 %). Colorless foam, softening at 87−89 °C. IR (KBr, cm^{-1}): 3441*w*, 2986*m*, 2939*s*, 2866*m*, 1737*s*, 1449*m*, 1381*m*, 1318*s*, 1259*m*, 1194*m*, 1159*m*, 1094*s*, 1060*s*, 1016*s*, 944*m,* 926*m*. ^{1}H-NMR (200 MHz, $CDCl_3$, δ / ppm): 4.62 (2H, *m*), 4.36 (1H, *m*), 4.12 (2H, *m*), 3.31 (3H, *m*), 3.00–1.40 (20H, *m*), 1.48 (3H, *s*), 1.32 (3H, *s*); ^{13}C-NMR (50 MHz, $CDCl_3$, δ / ppm): 174.12, 112.58, 109.34, 108.41, 107.19, 85.14, 84.19, 81.75, 64.69, 54.88, 41.42, 29.44, 26.38, 25.27, 24.94, 21.99; (+)ESI–HRMS (*m*/*z*, %): 481.20359 ([M+Na]$^+$, 100); calculated 481.20442.

In vitro *antimalarial activity*

The *in vitro* antimalarial drug susceptibility screen is a modification of the procedures first published by Desjardins *et al.*,[7] with modifications developed by Milhous *et al.*,[8] and the details are given elsewhere.[2a]

Acknowledgements. This work was supported by the Ministry of Science of the Republic of Serbia (Grant No. 142022) and the Serbian Academy of Sciences and Arts. The material has been reviewed by the Walter Reed Army Institute of Research. There is no objection to its presentation or publication. The opinions or assertions contained herein are the private views of the authors and are not to be construed as official or as reflecting the true views of the Department of the Army or the Department of Defense.

И З В О Д

РИБОФУРАНОЗА КАО НОСАЧ ТЕТРАОКСАНСКЕ И 4-АМИНОХИНОЛИНСКЕ АНТИМАЛАРИЈСКЕ ФАРМАКОФОРЕ

ИГОР М. ОПСЕНИЦА[1], KIRSTEN K. SMITH[2], LUCIA GERENA[2], САНДРА ГАИЦА[3] и БОГДАН А. ШОЛАЈА[1]

[1]Хемијски факултет Универзитета у Београду, п. пр. 158, 11000 Београд, [2]Division of Experimental Therapeutics, Walter Reed Army Institute of Research, Washington, DC 20307-5100, USA и [3]Институт за хемију, технологију и металургију, Његошева 12, 11000 Београд

У овом раду приказана је синтеза неколико рибофуранозидних тетраоксана и 4-аминохинолина у циљу сагледавања односа структура–активност ове врсте антималарика. Једињења су показала изражену антималаријску активност према хлорокин-осетљивом (D6), хлорокин-резистентном (W2) и вишеструко резистентном (TM91C235 (Thailand)) сојy *Plasmodium falciparum*. Аминохинолински дериват **4** је активнији према W2 и TM91C235 сојевима од контролних једињења (хлорокин и мефлокин).

(Примљено 13. фебруара 2008)

REFERENCES

1. Malaria Foundation International, http://www.malaria.org (October 14, 2008), and the sites for which the links are given therein
2. (a) D. Opsenica, G. Pocsfalvi, Z. Juranić, B. Tinant, J.-P. Declercq, D. E. Kyle, W. K. Milhous, B. A. Šolaja, *J. Med. Chem.* **43** (2000) 3274; (b) B. A. Šolaja, N. Terzić, G. Pocsfalvi, L. Gerena, B. Tinant, D. Opsenica, W. K. Milhous, *J. Med. Chem.* **45** (2002) 3331; (c) D. Opsenica, D. E. Kyle, W. K. Milhous, B. A. Šolaja, *J. Serb. Chem. Soc.* **68** (2003) 291; (d) I. Opsenica, N. Terzić, D. Opsenica, D. Angelovski, M. Lehnig, P. Eilbracht, B. Tinant, Z. Juranić, K. S. Smith, Y. S. Yang, D. S. Diaz, P. L. Smith, W. K. Milhous, D. Doković, B. A. Šolaja, *J. Med. Chem.* **49** (2006) 3790; (e) I. Opsenica, D. Opsenica, M. Jadranin, K. S. Smith, W. K. Milhous, M. Stratakis, B. Šolaja, *J. Serb. Chem. Soc.* **71** (2007) 1181; (f) N. Terzić, D. Opsenica, D. Milić, B. Tinant, K. S. Smith, W. K. Milhous, B. A. Šolaja, *J. Med. Chem.* **50** (2007) 5118; (g) I. Opsenica, D Opsenica, K. S. Smith, W. K. Milhous, B. A. Šolaja, *J. Med. Chem.* **51** (2008) 2261
3. L. A. Paquette, S. Bailey, *J. Org. Chem.* **60** (1995) 7849
4. I. Opsenica, N. Terzić, D. Opsenica, W. K. Milhous, B. Šolaja, *J. Serb. Chem. Soc.* **69** (2004) 919
5. C. C. Musonda, J. Gut, P. J. Rosenthal, V. Yardley, R. C. Carvalho de Souza, K. Chibale, *Bioorg. Med. Chem.* **14** (2006) 5605
6. R. F. Butterworth, S. Hannesian, *Can. J. Chem.* **49** (1971) 2755
7. R. E. Desjardins, C. J. Canfield, D. E. Haynes, J. D. Chulay, *Antimicrob. Agents Chemother.* **16** (1979) 710
8. W. K. Milhous, N. F. Weatherly, J. H. Bowdre, R. E. Desjardins, *Antimicrob. Agents Chemother.* **27** (1985) 525.

www.shd.org.rs

Journal of the Serbian Chemical Society

JSCS@tmf.bg.ac.yu • www.shd.org.rs/JSCS

J. Serb. Chem. Soc. 73 (11) 1027–1037 (2008)
JSCS–3784

UDC *Resveratrol:663.253:615–188(497.11)
Original scientific paper

Trans- and *cis*-resveratrol concentration in wines produced in Serbia

SANJA ĐEKIĆ[1], SLOBODAN MILOSAVLJEVIĆ[1#], VLATKA VAJS[2#], SLOBODAN JOVIĆ[3], ALEKSANDAR PETROVIĆ[3], NINOSLAV NIKIĆEVIĆ[3], VERICA MANOJLOVIĆ[4], VIKTOR NEDOVIĆ[3] and VELE TEŠEVIĆ[1*#]

[1]Faculty of Chemistry, University of Belgrade, Studentski trg 16, 11000 Belgrade, [2]Institute for Chemistry, Technology and Metallurgy, University of Belgrade, Njegoševa 12, 11000 Belgrade, [3]Faculty of Agriculture, University of Belgrade, Nemanjina 6, 11080 Zemun and [4]Faculty of Technology and Metallurgy, Karnegijeva 4, 11000 Belgrade, Serbia

(Received 3 March, revised 22 May 2008)

Abstract: Resveratrol, which occurs in two isomeric forms, *trans* and *cis*, is a phytoalexin with numerous pharmacological activities, such as anti-cancer, antiviral, neuroprotective and anti-aging. Red wine is the main source of the compound and an easy way of including resveratrol in the human diet. In this study, the most popular commercial Serbian wines (red, white and rosé-type) were analyzed for their content of *trans*- and *cis*-resveratrol. The analysis was performed by HPLC with a UV detector. Prior to the injection, phenolic compounds were extracted onto a LiChrolut RP18 bonded silica cartridge. The concentration of *trans*-resveratrol ranged from 0.11 to 1.69 mg L^{-1} and *cis*-resveratrol from 0.12 to 1.49 mg L^{-1}.

Keywords: *trans*/*cis*-resveratrol; wine; HPLC.

INTRODUCTION

Wine is defined as the fermented juice of *Vitis vinifera* grapes used as a beverage, while viticulture is the cultivation of grapes especially for wine making.[1] Wine has been produced and enjoyed for thousands of years. References to wine can be seen in writings dating back to the days of Hammurabi and to the Bible.

Wines are known to contain many biologically active compounds. The amounts and compositions of these compounds depend on the type of grapes and their degree of ripeness, climate and soil of the viticultural area, as well as vinification techniques.

There are many different types of wines that can be produced by a variety of different methods. From red to rosé to white and from fortified to sparkling,

* Corresponding author. E-mail: vtesevic@chem.bg.ac.yu
# Serbian Chemical Society member.
doi: 10.2298/JSC0811027D

wines can be produced with a variety of different flavors, aromas, in addition to alcohol contents.

Phenolic compounds are an important group of substances in wine that contribute to several sensory characteristics, such as color, flavor and astringency. Furthermore, it has been reported that phenols have multiple biological effects, such as antioxidant activity, anti-inflammatory action, inhibition of platelet aggregation and antimicrobial activity.[2]

Several beneficial physiological properties have been attributed to wine. It has been shown to have anticancer (chemo-preventive), anti-inflammatory, antifungal, and anti-microbial properties. There is also considerable evidence that a correlation exists between red wine consumption and the prevention of coronary heart disease, due to its beneficial anti-oxidant effect on low-density lipoprotein (LDL), which causes arteriosclerosis.[3] The cancer chemopreventive properties of resveratrol were first appreciated when Jang *et al*. demonstrated that resveratrol possesses cancer chemopreventive activity against all the three major stages of carcinogenesis *i.e*., initiation, promotion and progression.[4] Some findings suggest that resveratrol may also be anticarcinogenic and a potent chemopreventive agent for breast cancer.[5] Traditional Japanese and Chinese folk medicine use root extract of the weed *Polygonum cuspidatum*, which contains resveratrol, to fight liver, skin and circulatory-diseases.[6,7]

One of the important phenolic bioactive constituents in wine is resveratrol (3,4',5-trihydroxystilbene), a naturally occurring phytoalexin produced by some spermatophytes, such as grapevines, in response to injury. In grape species, resveratrol reaches concentrations of 50–400 μg/g fresh weight in the leaves. Resveratrol is also synthesized in the berries and in lignified plant tissues. Concentrations in the skin (pericarp) of the berries are high compared with those in the flesh. During mashing, a part of the resveratrol from the skins is dissolved in the must. However, only low levels occur in white wine (≤ 1 mg L^{-1}), whereas red wines contain on average 2 mg L^{-1}.[8–10]

Resveratrol exists in *cis*- and *trans*- isomeric forms (Fig. 1), but the *cis*-isomer is present only in small amounts.[11–13] However, *cis*-resveratrol and its glucoside have been detected in almost all wines analyzed to date, regardless of the origin and the technology applied. Both isomeric forms were detected in white, rosé, and red wine. The *cis*-isomer is probably transformed during the vinification process but usually does not reach the concentration of the *trans*-isomer in the wine.[14]

Resveratrol is the parent molecule of a family of polymers named viniferins. Plants also synthesize glucosides (piceid = resveratrol 3-*O*-*β*-glucoside).

The concentrations in the form of *trans*- and *cis*-isomers of aglycone and glucosides are subject to numerous variables. In red wine, the concentrations of the *trans*-isomer, which is the major form, generally ranges between 0.10 and 15 mg L^{-1}.[2]

Wines of the rosé type exhibit intermediate values between red and white wines. This is presumably due to the longer extraction time during contact between grape skin and juice in the production of red wine.[15,16]

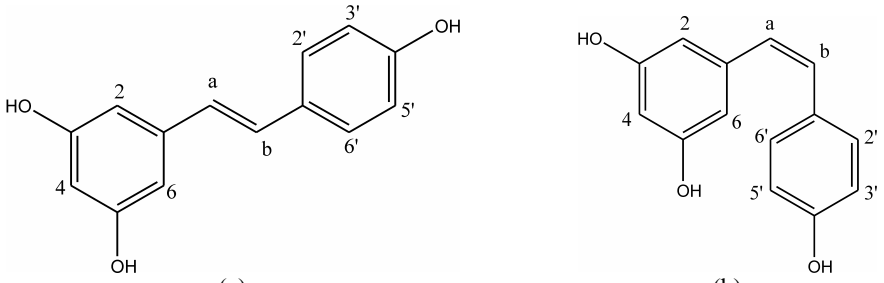

Fig. 1. a) *trans*-resveratrol, b) *cis*-resveratrol.

Resveratrol concentrations increase during fermentation of the skins but the amount extracted is dependent on the variety and enological conditions.[17–19] The extraction of resveratrol from the skin may be facilitated by the production of ethanol during the fermentation process.

Resveratrol is synthesized in response to microbial infection or stress.[18] However, it is also produced after chemical treatment, such as herbicide or fungicide application, and by exposure to UV light.[20,21]

The complexity of the wine matrix makes analysis by a single technique difficult. Usually, purification prior to the analysis is crucial. Thus, solid phase microextraction, solvent extraction, and elution through preconcentration columns are performed. High performance liquid chromatography (HPLC) and gas chromatography (GC) are the two major techniques used. Furthermore, these instruments can be coupled to various types of detectors, including UV, photodiode array (DAD),[22] chemiluminescent detection (CL),[23] fluorescence detection (FD),[24] and mass spectrometry (MS).[13,25]

The aim of the present study was to determine the *trans*- and *cis*-resveratrol content in 18 commercial samples of wines produced in Serbia. At the present time, there are no reports in the literature about the resveratrol content in wines from Serbia.

EXPERIMENTAL

Wine samples and standards

The analyses were performed on eighteen commercial Serbian wine samples (10 red, 7 white and 1 rosé), from six different producers. All wines were stored in the dark at 4.0 °C and analyzed immediately after bottle opening. *trans*-Resveratrol was purchased from Sigma Chemical Co. (St. Louis, MO). *cis*-Resveratrol is not commercially available and was therefore obtained through UV-photoisomerization (280–310 nm, for 10 h) of a standard solution (100 mg L^{-1}) of *trans*-resveratrol. Under these conditions, 80 % of the *trans*-resveratrol

was converted into the *cis*-isomer (examined by HPLC and ^{1}H-NMR spectroscopy). The ^{1}H-NMR spectra and HPLC chromatograms of *trans*-resveratrol prior and after UV treatment are shown in Figs. 2–4.

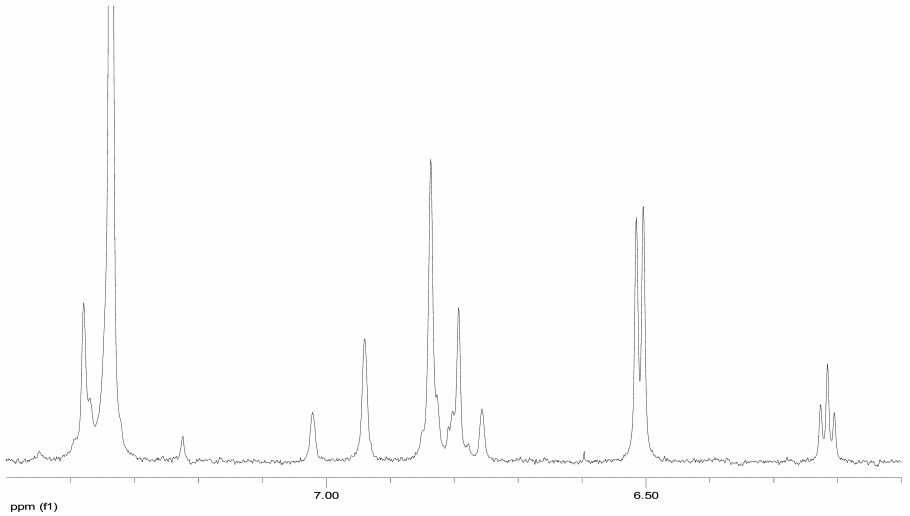

Fig. 2. ^{1}H-NMR (200 MHz) spectra of *trans*-resveratrol in $CDCl_3$ before UV-photoisomerization (δ/ ppm: 6.51 (2H, *d*, H-2/6, *J* = 2.0 Hz), 6.21 (1H, *t*, H-4, *J* = 2.0 Hz), 7.35 (2H, *d*, H2'/6', *J* = 8.5 Hz), 6.81 (2H, *d*, H3'/5', *J* = 8.5 Hz), 6.80 (lH, *d*, Ha, *J* = 16.5 Hz), 6.97 (lH, *d*, Hb, *J* = 16.5Hz)).

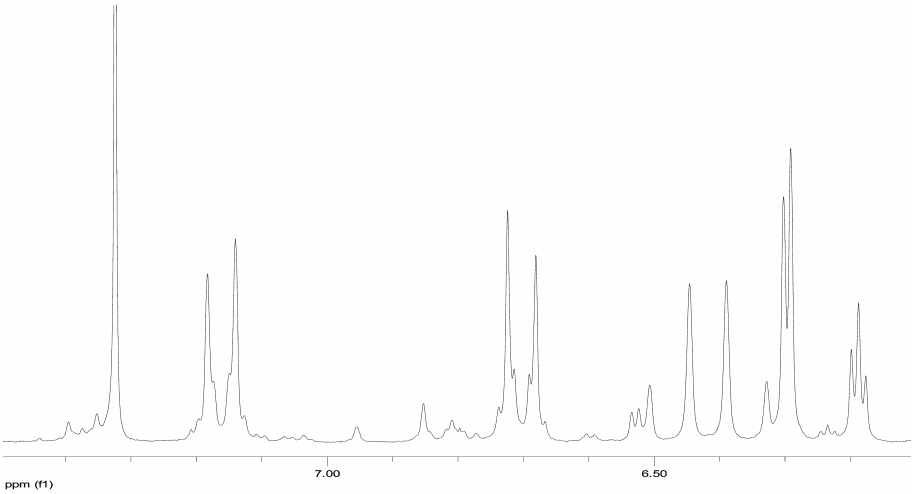

Fig. 3. ^{1}H-NMR (200 MHz) spectra in $CDCl_3$ of *cis*-resveratrol obtained after UV-photoisomerization of *trans*-resveratrol (δ/ ppm: 6.30 (2H, *d*, H-2/6, *J* = 2.0 Hz), 6.19 (1H, *t*, H-4, *J* = 2.0 Hz), 7.16 (2H, *d*, H2'/6', *J* = 8.5 Hz), 6.70 (2H, *d*, H3'/5', *J* = 8.5 Hz), 6.35 (lH, *d*, Ha, *J* = 12.0, Hz), 6.47 (lH, *d*, Hb, *J* = 12.0 Hz)).

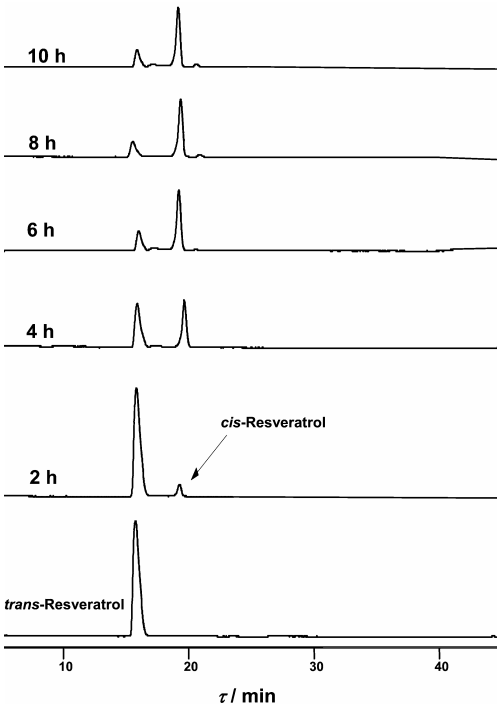

Fig. 4. LC chromatograms of the *cis*-resveratrol obtained during irradiation of *trans*-resveratrol.

Analytical HPLC procedure

A Hitachi HPLC system consisting of two pumps (Model 655A-11), a Hitachi automated gradient controller (Model L-5000) and autosampler Hitachi (Model 655A-40) was used. The chromatograms where recorded using a Gilson 117 UV dual wavelength detector. A Baseline Workstation CSW32 and a personal computer were employed for data storage and evaluation. The analytical column was a Bishoff Hyperchrome, ODS Hypersil (25 cm×4.6 mm ID, 5 μm particle diameter).

The HPLC column was initially equilibrated with acetonitrile–acetic acid–water (20:2:78, v/v) as solvent A for 10 min. The chromatographic separation was performed using a six stage linear gradient: from 100 to 90 % of A in 8 min, from 90 to 85 % of A in 12 min, from 85 to 70 % of A in 15 min, from 70 to 50 % of A in 5 min and from 50 to 0 % of A in 5 min, with a total flow rate of 1.0 ml min^{-1}. The total gradient time was 42 min. A mixture of acetonitrile––acetic acid–water (90:2:8, v/v) was used as solvent B. The eluent was monitored at 306 and 286 nm, the optimum UV absorbances of *trans*- and *cis*-resveratrol, respectively.

Calibration and recovery

Calibration graphs were obtained by plotting the peak area against the concentration. Six standards of *trans*- and *cis*-resveratrol covering the range 0.10–15 and 0.25–10 mg L^{-1} were made up in methanol and analyzed in duplicate. The constructed calibration curves showed excellent linearity (Table I).

The precision of the method was confirmed by repetitive analyses, calculating the average relative standard deviation (*RSD*) for 6 replicate determinations. The limit of detection (*LOD*, $S/N = 3$) of the individual compounds was calculated at their absorbance maxima. The

recoveries for *trans*- and *cis*-resveratrol were determined by adding known amounts of resveratrol to the wine sample and by performing assays before and after addition. The recovery was 94.56 and 95.61 % for *trans*- and *cis*-resveratrol, respectively (Table I).

TABLE I. Analytical characteristics for the determination of resveratrol in wine samples by HPLC–UV (t_R – retention time; λ – wavelength of absorbance maxima; R^2 – correlation coefficient; *RSD* – repeatability)

Compound	t_R / min	λ / nm	Linearity interval mg L^{-1}	*LOD* / mg L^{-1}	R^2	*RSD* %	Recovery %
trans-Resveratrol	16.02	306	0.10–15	0.02	0.9998	3.3	94.56
cis-Resveratrol	18.53	286	0.25–10	0.05	0.9994	5.8	95.61

Solid-phase extraction (SPE) of wine samples

The determination of polyphenolic compounds in wine samples usually requires extraction and preconcentration procedures prior to the HPLC analysis. This is because wine has very complex composition and many phenolic compounds are present at very low concentrations.

A sample of wine was first filtered through a 0.45 μm membrane filter. The solid-phase extraction was performed using a LiChrolut RP18 bonded porous silica cartridge (3 ml, 300 mg), obtained from Merck. The cartridges were previously conditioned with 10 ml of methanol, followed by 5 ml of water. Then, 5 ml of wine were introduced. Then the cartridge was dried under vacuum and, finally, the compounds were eluted with 1 ml of methanol. All analyses were performed in triplicate and the data are presented as mean ± error (95 % confidence level, $F = 4$, $n = 5$).

NMR analysis

The ^{1}H-NMR (200 MHz) spectra were recorded on a Varian Gemini 2000 spectrometer in $CDCl_3$.

RESULTS AND DISCUSSION

The results of the chromatographic analyses of the 18 different Serbian wines are summarized in Table II. Typical chromatograms of red and white wine are shown in Figs. 5 and 6, respectively.

TABLE II. Concentrations of resveratrol in Serbian wines (mg L^{-1})

Wine and vintage	Wine producer	Alcohol content vol. %	*trans*-Resveratrol	*cis*-Resveratrol
Cabernet Sauvignon[a] 2000	Navip, Zemun	12.0	0.61±0.04	0.27±0.04
Cabernet Sauvignon[a] 2002	Podrum Radovanović, Krnjevo	12.5	1.69±0.04	0.81±0.04
Cabernet Sauvignon[a] 2004	Faculty of Agriculture, University of Belgrade, Zemun	13.0	0.18±0.04	0.19±0.04
Cabernet Sauvignon[a] 2002	Rubin, Kruševac	12.0	0.36±0.04	0.42±0.04

TABLE II. Continued

Wine and vintage	Wine producer	Alcohol content vol. %	*trans*-Resveratrol	*cis*-Resveratrol
Cabernet Sauvignon[a] 2004	VinoVita, Trstenik	12.5	1.00±0.04	1.49±0.04
Merlot "Dionis"[a], 2000	Navip, Zemun	12.0	1.00±0.04	0.53±0.04
Merlot[a], 2003	Faculty of Agriculture, University of Belgrade, Zemun	13.5	0.11±0.04	0.12±0.04
Royal[a], 2000	Navip, Zemun	11.5	0.72±0.04	0.66±0.04
Pinot Noir[a], 2001	Rubin, Kruševac	11.5	1.31±0.04	0.82±0.04
Vranac[a], 2000	Rubin, Kruševac	11.5	0.84±0.04	0.20±0.04
Rosé[b], 2004	Faculty of Agriculture, University of Belgrade, Zemun	12.0	0.29 ± 0.04	< 0.05 ± 0.04
Chardonnay[c], 2002	Podrum Radovanović, Krnjevo	12.5	0.29±0.04	< 0.05±0.04
Chardonnay[c], 2004	Faculty of Agriculture, University of Belgrade, Zemun	12.0	< 0.02 ± 0.04	< 0.05±0.04
Chardonnay blanc[c] 2002	Navip, Zemun	12.4	0.19±0.04	< 0.05±0.04
Chardonnay[c], 2003	Rubin, Kruševac	12.0	0.15±0.04	< 0.05±0.04
Chardonnay[c], 2002	Erdevik, Erdevik	12.5	0.34±0.04	0.40±0.04
Sauvignon[c], 2003	Rubin, Kruševac	12.1	0.11±0.04	< 0.05±0.04
Graševina[c], 2000	Erdevik, Erdevik	11.5	0.33±0.04	0.58±0.04

[a]Red wine; [b]rosé wine; [c]white wine

Only free forms of resveratrol were analyzed. The contents of resveratrol in red wines showed a relatively high variability. The concentration of *trans*-resveratrol ranged from 0.11 to 1.69 mg L^{-1} and that of *cis*-resveratrol from 0.12 to 1.49 mg L^{-1}.

The obtained resveratrol concentrations were compared with those reported for foreign wines. The concentrations of *trans*-resveratrol in the analyzed wines from Serbia were significantly lower than in wines produced in other countries. The average levels of *trans*-resveratrol in red and white wines vary greatly from one region to another. Although significant differences were found between regions, no specific region was significantly different from the others. A comparison of the content from different regions is given in Table III.

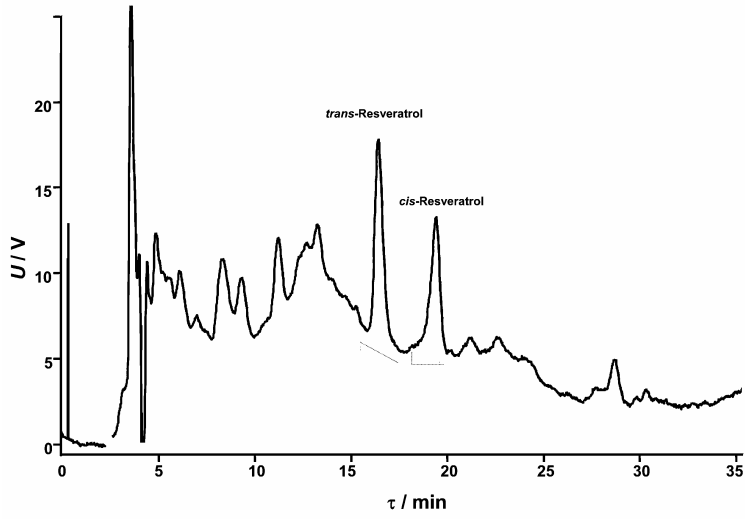

Fig. 5. Chromatogram of the red wine Cabernet Sauvignon (Vino Vita, Trstenik).

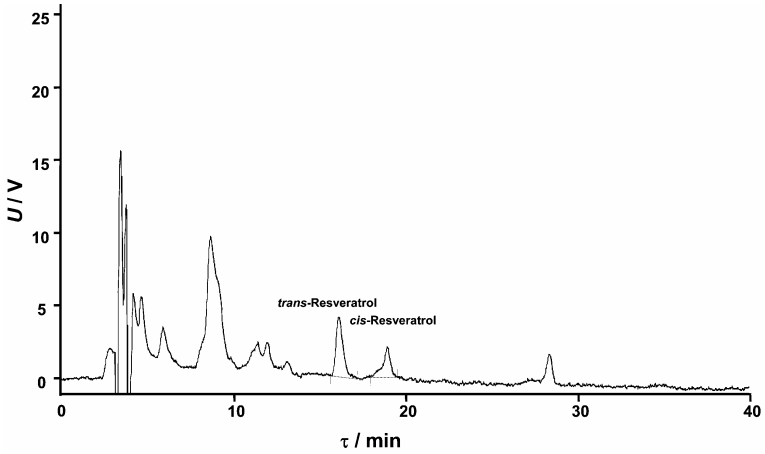

Fig. 6. Chromatogram of the white wine Chardonnay (Erdevik, Erdevik).

These differences could be attributed to environmental conditions, such as humidity and fungal disease, which are factors influencing the production of *trans*--resveratrol by grapevines.[26] However, Soleas *et al.*[26] stated that the difference between the statistical parameters, sample pretreatment (direct injection or not) and the chromatographic method (GC or HPLC) might cause different result. For example, wines from Italy presented mean values of resveratrol varying from 0.03 to 8.87 mg L^{-1}.

Seven white wines were analyzed. As it can be seen (Table II), the highest amount of *trans*-resveratrol was found in Chardonnay 2002 (0.34 mg L^{-1}). The highest value for *cis*-resveratrol in white wines was 0.58 mg L^{-1} (Table II).

TABLE III. Previous reports of *trans* and *cis*-resveratrol concentrations (mg l^{-1}) in red and white wines

Country	*trans*-Resveratrol		*cis*-Resveratrol		Reference
	Lowest	Highest	Lowest	Highest	
Red wines					
Brazil	0.82	5.75	1.70	22.9	27, 28
Italy	0.03	8.87	0.13	2.55	13, 24, 29, 30
France	0.30	7.62	0.30	5.30	31–36
Spain	0.18	8.00	0.02	2. 48	33, 37–40
Canada	0.15	5.79	1.48	6.52	27, 41
China	0.07	3.20	–	–	23
Portugal	0.20	5.70	0.03	9.50	32, 36, 41, 42
Greece	0.37	2.53	–	–	34, 43, 44
Chile	0.80	1.57	0.14	1.23	33, 36
Czech Republic	0.92	6.25	0.68	2.80	45
Slovenia	0.90	8.70	–	–	39
USA	0.23	5.81	0.07	2.96	33, 36
Korea	0.19	3.30	–	–	46
Japan	0.001	2.30	–	–	14, 18
Hungary	0.10	14.3	–	–	47
Australia	0.20	10.6	–	–	36, 38
White wines					
Italy	0.02	0.55	–	—	24, 29, 30
France	0.30	4.00	0.10	0.10	35, 49
Spain	0.07	2.50	n.d.	0.18	37, 38, 50, 51
Portugal	0.03	2.60	0.90	1.70	32, 41
Greece	0.03	0.14	–	–	43
Slovenia	n.d.	0.60	–	–	39

CONCLUSIONS

In this study, for the first time, focus was directed on the determination of *trans*-resveratrol and *cis*-resveratrol levels in red wines produced in Serbia.

The resveratrol content of a wine is related to the length of time the grape skins are present during the fermentation process. Thus, the concentration is significantly higher in red wines than in white wines, because the skins are removed earlier during white wine production, reducing the amount extracted.

cis-Resveratrol has been detected in almost all hitherto analyzed wines, regardless of the origin and the technology applied. Generally, the high levels of *cis*-resveratrol in Serbian wines support the assumption that resveratrol is initially produced as the *trans*-isomer and the *cis*-isomer is derived by subsequent isomerization of the *trans*-isomer, mainly during fermentation.

Acknowledgments. This research was supported by grant from the Ministry of Science of the Republic of Serbia (Project 142053).

И З В О Д

КОНЦЕНТРАЦИЈА *trans*- И *cis*-РЕЗВЕРАТРОЛА У ВИНИМА ПРОИЗВЕДЕНИМ У СРБИЈИ

САЊА ЂЕКИЋ[1], СЛОБОДАН МИЛОСАВЉЕВИЋ[1], ВЛАТКА ВАЈС[2], СЛОБОДАН ЈОВИЋ[3], АЛЕКСАНДАР ПЕТРОВИЋ[3], НИНОСЛАВ НИКИЋЕВИЋ[3], ВЕРИЦА МАНОЈЛОВИЋ[4], ВИКТОР НЕДОВИЋ[3] и ВЕЛЕ ТЕШЕВИЋ[1]

[1]Хемијски факултет, Универзитет у Београду, Студентски трг 16, 11000 Београд, [2]Институт за хемију, технологију и металургију, Његошева 12, 11000 Београд, [3]Пољопривредни факултет, Универзитет у Београду, Немањина 6, 11080 Земун и [4]Технолошко–металуршки факултет, Универзитет у Београду, Карнегијева 4, 11000 Београд

Методом течне хроматографије (HPLC) испитан је садржај слободног облика *trans*- і *cis*-резвератрола у осамнаест комерцијалних узорака (10 црвених, 7 белих и 1 розе) српских вина. Сви узорци су пре хроматографије екстраховани SPE техником на LiChrolut RP18 колони. *trans*-Резвератрол је детектован у 17 од 18 анализираних узорака вина са просечном концентрацијама од 0,78 mg l^{-1} за црвена вина и 0,23 mg l^{-1} за бела вина. Највиша концентрација *trans*-резвератрола је нађена у узорку црвеног вина Cabernet Sauvignon бербе 2002 године. *cis*-Резвератрол је детектован у 12 од 18 анализираних узорака вина са просечном концентрацијом 0,55 mg l^{-1} за црвена вина, док је у белим винима од анализираних 7 узорака детектован само у 2 узорка са концентрацијама 0,12 и 0,49 mg l^{-1}. Висок садржај *cis*-резвератрола у неким узорцима је вероватно последица изомеризације *trans*- у *cis*-резвератрол током процеса производње вина.

(Примљено 3. марта, ревидирано 22. маја 2008)

REFERENCES

1. Wikipedia, http://en.Wikipedia.org/wiki (retrieved 2008-05-15)
2. L. Frémont, *Life Sci.* **66** (2000) 663
3. J. C. Ruf, *Biol. Res.* **37** (2004) 209
4. M. Jang, L. Cai, G. O. Udeani, K. V. Slowing, C. F. Thomas, C. W. W. Beecher, H. H. S. Fong, A. D. Kighorn, R. G. Mehta, R. C. Moon, J. M. Pezzuto, *Science* **275** (1997) 218
5. O. P. Mgbonyebi, J. Russo, I. H. Russo, *Int. J. Oncol*. **12** (1998) 865
6. Y. Kimura, H. Ohminami, H. Okuda, K. Baba, M. Kozawa, S. Arichi, *Planta Med.* **49** (1983) 51
7. B. C. Vastano, Y. Chen, N. Zhu, C. T. Ho, Z. Zhou, R. T. Rosen, *J. Agric. Food Chem*. **48** (2000) 253
8. D. M. Goldberg, J. Yan, E. Ng, E. P. Diamandis, A.Karumanchiri, G. Soleas, A. L. Waterhouse, *Am. J. Enol. Vitic*. **46** (1995) 159
9. H. E. Siemann, L. L. Creasy, *Am. J. Enol. Vitic*. **43** (1992) 49
10. U. Strevbo, O. Vang, C. Bonnesen, *Food Chem.* **101** (2007) 449
11. P. Langcake, R. J. Pryce, *Physiol. Plant Pathol*. **9** (1976) 77
12. P. Jeandet, R. Bessis, B. Gautheron, *Am. J. Enol. Vitic*. **42** (1991) 41
13. M. Careri, C. Corradini, L. Elviri, I. Nicoletti, I. Zagnoni, *J. Agric. Food Chem.* **52** (2004) 6868
14. M. Sato, Y. Suzuki, T. Okuda, K. Yokotsuka, *Biosci. Biotechol. Biochem.* **61** (1997) 1800
15. A. Gonzalo, P. Vidal, S. Minguez, R. Antoli, *J. Wine Res.* **6** (1995) 213
16. A. I. Romero-Pérez, R. M. Lamuela-Raventós, A. L. Waterhouse, M. C. de la Torre-Bonorat, *J. Agric. Food Chem.* **44** (1996) 2124
17. P. Jeandet, R. Bessis, B. F. Maume, P. Meunier, D. Peyron, P. Trollat, *J. Agric. Food Chem*. **43** (1995) 316
18. T. Okuda, K. Yokotosuka, *Am. J. Enol. Vitic*. **47** (1996) 93

19. G. J. Soleas, D. M. Goldberg, A. Karumanchiri, E. P. Diamandis, E. Ng, *J. Wine Res*. **6** (1995) 107
20. P. Langcake, R. J. Pryce, *Phytochemistry* **16** (1976) 1193
21. R. T. Threlfall, J. R. Morris, A. Mauromoustakos, *Am. J. Enol. Vitic*. **50** (1999) 57
22. P. Jeandet, A. C. Breuil, M. Adrian, L. A. Weston, S. DeBord, P. Meuneir, G. Maume, R. Bessis, *Anal. Chem.* **69** (1997) 5172
23. J. Zhou, H. Cui, G. Wan, H. Xu, Y. Pang, C. Duan, *Food Chem.* **88** (2004) 613
24. F. Buiarelli, F. Coccioli, R. Jasionowska, M. Merolle, A. Terracciano, *Chromatographia* **7/8** (2006) 64
25. V. Ferreira, R. Lopez, A. Escudero, J. F. Cacho, *J. Chromatogr. A*. **806** (1998) 349
26. G. Soleas, D. M. Goldberg, E. P. Diamandis, A. Karumanchiri, J. Yan, E. Ng, *Am. J. Enol. Vitic*. **46** (1995) 346
27. X. Vitrac, A. Bornet, R. Vanderlinde, J. Valls, T. Richard, J. C. Delaunay, J. M. Mérillon, P. L. Teissédre, *J. Agric. Food Chem*. **53** (2005) 5664
28. A. A. Souto, M. C. Carneiro, M. Seferin, M. J. H. Senna, A. Conz, K. Gobbi, *J. Food Compos. Anal.* **14** (2001) 441
29. M. Castellari, E. Sartini, A. Fabiani, G. Arfelli, A. Amati, *J. Chromatogr. A* **973** (2002) 221
30. R. Lopez, P. Dugo, L. Mondello, *J. Sep. Sci.* **30** (2007) 669
31. M. Abert Vian, V. Tomao, S. Gallet, P. O. Coulomb, J. M. Lacombe, *J. Chromatogr. A* **1085** (2005) 224
32. M. T. Ribeiro de Lima, P. Waffo-Téguo, P. L. Teissedre, A. Pujolas, J. Vercauteren, J. C. Cabanis, J. M. Mérillon, *J. Agric. Food Chem.* **47** (1999) 2666
33. D. M. Goldberg, E. Ng, A. Karumanchiri, J. Yan, E. P. Diamandis, G. J. Soleas, *J. Chromatogr. A* **708** (1995) 89
34. A. V. Sakkiadi, S. A. Haroutounian, M. N. Stavrakakis, *Lebensm.Wiss. Technol.* **34** (2001) 410
35. X. Vitrac, J. P. Monti, J. Vercauteren, G. Deffieux, J. M. Mérillon, *Anal. Chim. Acta* **458** (2002) 103
36. X. Gu, L. Creasy, A. Kester, M. Zeece, *J. Agric. Food Chem.* **47** (1999) 3223
37. M. A. Rodríguez-Delgado, G. González, J. P. Pérez-Trujillo, F. J. García-Montelongo, *Food Chem.* **76** (2002) 371
38. P. Vinãs, C. López-Erroz, J. J. Marìn-Hernández, M. Hernández-Córdoba, *J. Chromatogr. A* **871** (2000) 85
39. U. Vrhovsek, R. Eder, S. Wendelin, *Acta Aliment.* **24** (1995) 203
40. M. Abril, A. I. Negueruela, C. Pérez, T. Juan, G. Estopañán, *Food Chem.* **92** (2005) 729
41. N. Ratola, J. L. Faria, A. Alves, *Food Technol. Biotechnol*. **42** (2004)125
42. J. A. B. Baptista, J. F. P. Tavares, R. C. B. Carvalho, *Food Res. Intern*. **34** (2001) 345
43. V. G. Dourtoglou, D. P. Makris, F. Bois-Dounasand, C. Zonas, *J. Food Compos. Anal.* **12**(1999) 227
44. S. Kallithraka, I. Arvanitoyannis, A. El-Zajouli, P. Kefalas, *Food Chem.* **75** (2001) 355
45. I. K. Hanzlikova, K. Melzoch, V. Filip, J. Smidrkal, *Food Chem.* **87** (2004) 151
46. K. S. Kim, S. Y. Ghim, Y. B. Seu, B. H. Song, *J. Microbiol. Biotechnol.* **9** (1999) 691
47. L. Mark, M. S. P. Nikfardjam, P. Avar, R. Ohmacht, *J. Chromatogr. Sci.* **43** (2005) 445
48. Y. Shao, P. Marriott, H. Hugel, *Chromatographia* **57** (2003) 349
49. M. Adrian, P. Jeandet, A. C. Breuil, D. Levite, S. Debord, R. Bessis, *Am. J. Enol. Vitic*. **51** (2000) 37.
50. M. Abril, A. I. Negueruela, C. Perez, G. Estopan, *Food. Chem*. **92** (2005) 729
51. M. V. Martinez-Ortega, M. C. Garcia-Parrilla, A. M. Troncoso, *Nahrung* **44** (2000) 253

www.shd.org.rs

Journal of the Serbian Chemical Society

JSCS@tmf.bg.ac.yu • www.shd.org.rs/JSCS

J. Serb. Chem. Soc. 73 (11) 1039–1049 (2008) UDC **Ambrosia artemisiifolia*:638.138:615.28–188
JSCS–3785 *Original scientific paper*

Chemical composition and biological activity of the acetone extract of *Ambrosia artemisiifolia* L. pollen

SLAVICA SOLUJIĆ[1]*, SLOBODAN SUKDOLAK[1], NENAD VUKOVIĆ[1], NEDA NIĆIFOROVIĆ[1] and SNEŽANA STANIĆ[2]

[1]*Department of Chemistry, Faculty of Science, University of Kragujevac, P.O. Box 12, 34000 Kragujevac and* [2]*Department of Biology, Faculty of Science, University of Kragujevac, P.O. Box 12, 34000 Kragujevac, Serbia*

(Received 10 December 2007, revised 21 May 2008)

Abstract: In this study, the chemical components, antimicrobial and genotoxic biological activities of the acetone extract of *Ambrosia artemisiifolia* L. pollen were examined. Two lactones were identified: ambrosin and artesovin. The antimicrobial activity of the acetone extract of *A. artemisiifolia* L. pollen was examined on ten different bacterial species using the disc diffusion method and the microdilution method in Mueller-Hinton broth dilution. The minimal inhibitory concentration of the acetone extract of *A. artemisiifolia* pollen varied between 1.25−6.50 mg mL^{-1}. The genotoxic effect of the acetone extract of *A. artemisiifolia* pollen on a eukaryotic model system *Drosophila melanogaster* was investigated using the SLRL test.

Keywords: *Ambrosia artemisiifolia* L.; pollen; extract; antimicrobial activity; genotoxicity.

INTRODUCTION

The *Ambrosia* (Asteraceae) genus is classified as belonging to the Heliantheae tribe. There are about 20 species of this genus in Europe and the ambrosia species is the most widespread one.[1] Ambrosia is conquering Europe with enormous speed due to the ability of its pollen to travel extremely fast, up to 300 km h^{-1}, if the wind is favourable.[2–5] Various measurements and testing have shown that the pollen concentrations in the European air have increased by up to 5 times in the last 10 years.

The *Ambrosia artemisiifolia* L. plant is an invasive, allergenic plant which produces large amounts of pollen.[6] The human immune system responds to the antigen present in the pollen through the so-called polinosis process.[7,8] During research of the *A. artemisiifolia* L. plant, the sesquiterpene lactones ambrosin, isa-

* Corresponding author. E-mail: ssolujic@kg.ac.yu
doi: 10.2298/JSC0811039S

belin, psilostachyn,[9,10] cumanin and peruvin,[11,12] as well as triterpenoids of the α- and β-amyrine type and derivatives of caffeic acid [6,13] were identified.

The sesquiterpene lactones are characterized by the presence of α,β-unsaturated γ-lactone moiety[14] and possess antibacterial, antifungal, antiprotozoal, anthelmintic, analgesic, schistosomicidal, genotoxic and mutagenic activities.[15–18]

In addition, various studies have suggested a presence of both genotoxic and mutagenic activities[19–21] of the sesquiterpene lactones. Genotoxic substances can perform deleterious actions on the genetic material of cells, thus affecting their integrity, and may, therefore, be potentially mutagenic or carcinogenic,[22–25] specifically those capable of causing genetic mutations and contributing to the development of tumours.[26–28] The sesquiterpene lactones go through a cellular metabolic transformation thereby acquiring the ability to damage DNA.[20,29–33] They operate by inhibiting certain enzymes responsible for maintaining the integrity of cells and, consequently, the integrity of an organism. The sesquiterpene lactones can react with the nucleophilic centres of intracellular macromolecules.[20] Such a reaction occurs with the thiol group of glutathione,[17] which is an important intracellular compound participating in the inactivation of chemical substances and it may be efficient in protecting cells and macromolecules such as DNA.[18,33]

Some of the above-mentioned examined lactones exhibit antimicrobial properties. Lactones exhibit bacteriostatic properties by inhibiting bacterial growth, or bactericidal, killing the bacteria. The critical attack site of anti-cell wall agents lies in the peptidoglycan layer. This layer is essential for the survival of bacteria in hypotonic environments. The loss or damage of this layer destroys the rigidity of the bacterial cell wall, resulting in death.[34–36]

This paper presents the results of the chemical isolation and identification of two lactones from the acetone extract of the pollen and some biological effects of this extract, *i.e.*, its antibacterial activity against some pathogenic bacteria and its genotoxic effect on a eukaryotic model system *Drosophila melanogaster* using the SLRL test.

EXPERIMENTAL

The melting points (m.p.) were recorded on a Kofler hot stage apparatus and are uncorrected. Microanalysis for carbon and hydrogen was performed using a Carlo Erba 1106 microanalyser. The IR spectra were run on Perkin-Elmer Grating Spectrophotometers, models 137 and 337. The NMR spectra were recorded on a Varian Gemini 200 spectrometer (^{1}H at 200 MHz and ^{13}C at 50 MHz) in $CDCl_3$, using TMS as the internal standard. The extract was monitored and separated by thin-layer chromatography (TLC) on MN-silica gel P/UV_{254} with $CaSO_4$.

Extraction of Ambrosia artemisiifolia *pollen*

Ambrosia artemisiifolia L. plants were collected from the region of Kragujevac, in central Serbia. The biomass was freeze-dried on the same day as it was collected. A voucher specimen of the plant (BEOU No. 16171) was deposited in the Herbarium of the Department of Biology of the Faculty of Science, University of Belgrade, Serbia. The pollen was separated from the plant leaves.

The pollen was first broken into small pieces using a cylindered crusher. Then, pollen pieces (60 g) were extracted with acetone (500 mL) using a Soxhlet apparatus.[37] The extract was filtered through a paper filter (Whatman, No. 1) and evaporated on a rotary evaporator. The crude acetone extract (1645 mg) of the pollen was washed with petroleum ether (70−90 °C) at room temperature during a 24 h period. The secondary petroleum ether extract (l430 mg) contained palmitic acid wax. The residue was dissolved in 50 mL of a 0.20 % solution of lead acetate in a 1:1 mixture of ethanol and water. After stirring over night, the solution was filtered, evaporated to a quarter of its volume, extracted with chloroform, dried over anhydrous sodium sulphate, evaporated and dissolved in acetone. The primary acetone extract pollen (820 mg) was stored in a dark glass bottle for further processing. The components were separated by preparative chromatography on MN-silica gel P/UV_{254} with $CaSO_4$ and a 6:4 mixture of benzene and ethyl acetate. The silica gel layer was extracted with ethyl acetate. The extracts were filtered and evaporated and the residues analysed spectroscopically. Two lactones were identified. The first was ambrosin (**1**), light white crystals with a m.p. 146–148 °C (ethanol) and R_f = 0.36 (benzene:ethyl acetate = 6:4). The second lactone was dihydroambrosin (**2**), white crystals with a m.p. 165–167 °C (diethyl ether) and R_f = 0.50 (benzene:ethyl acetate = 6:4).

Test microorganism

The bacterial strains used in these experiments were *Bacillus mycoides* (IPH), *Pseudomonas fluorescens* (B28), *Erwinia carotovora* (B31), *Enterobacter cloacae* (B22), *Klebsiella pneumoniae* (B26), *Agrobacterium tumefaciens* (B11), *Azotobacter chroococcum* (B14), *Staphylococcus aureus* (IHP), *Proteus* sp. (IHB) and *Pseudomonas aeruginosa* (IPH).

All of the tested bacteria cultures were obtained from the Institute for Health Protection (IPH) in Kragujevac and the Faculty of Agriculture, University of Belgrade, Serbia. The identity of the bacterial strains was confirmed in Laboratory for Microbiology at the Department of Biology, Faculty of Science, University of Kragujevac, Kragujevac, Serbia.

Antibacterial activity of the pollen acetone extract

The antibacterial activity of the acetone extract of the pollen was examined using the nutrient agar broth disc diffusion method and the microdilution method in Mueller-Hinton broth.[38,39] The disc diffusion method was performed using a 24 h culture which was reseeded on the nutrient broth at a temperature of 37 °C. The concentrations of the cultures were adjusted to 5.6×10^6 CFU mL^{-1} with sterile water. One mL of suspension was added over the plates containing nutrient agar broth in order to achieve a uniform microbial growth on both the control and test plates. The acetone extract of pollen was dissolved in 96 % ethanol (100 mg mL^{-1}) and sterilized. Under aseptic conditions, empty sterilized discs (Whatman No. 5, 14 mm diameter) were impregnated with 250, 100 and 50 μL of different concentrations (10 mg/disc and 5.0 mg/disc) of the respective extract, and placed on the agar surface. The plates were left for 30 min at room temperature to allow diffusion of the extract and then incubated at 37 °C.

After the incubation period (48 h), the zone of inhibition was measured and is presented in mm. A paper disc of the solvent (ethanol) was used as the control and Sinacilin® was used as a standard antibiotic for comparison. Each test was performed in triplicate and repeated three times.

The minimal inhibitory concentration (*MIC*) of the acetone extract was determined by the microdilution two-fold serial technique. A series of two-fold dilutions of the extract, ranging from 0.10 to 10 mg mL^{-1}, was prepared in Mueller-Hinton broth with the addition 0.10 mL of a suspension of the bacterial spores (5.4×10^6 CFU mL^{-1}). The results were determined after

24 h and the *MIC* values were determined as the lowest concentration of the extract which inhibited visible growth of each organism. Sinacilin (1.0 mg mL^{-1}) was chosen as the control drug.

Genotoxic activity of the pollen acetone extract

The sex-linked recessive lethal test for mutagenicity (or SLRL test) was performed with laboratory stocks of *Drosophila melanogaster* (obtained from the Umea Stock Centre, Sweden). The examined "Canton-S" types were individuals with a normal phenotype ("wild" type), while "Basc" line flies are characterized with individuals homozygous for a balancer X-chromosome, which carries two genetic markers: Bar (B) which produces a narrow shaped eye under homo- and hemizygous conditions and a kidney shaped eye when heterozygous in females. An eye restricted to a narrow vertical bar of 80 facets appears in males and 70 facets in homozygous females. Heterozygous females have an intermediate number of facets (360) compared to the homozygous females (70) and wild type (780).[40]

The character can be regarded as partially dominant; white-apricot (wa) – changes the red eye color into a light orange and is expressed only in homozygous females and hemizygous males (while in heterozygotes females are not expressed); scute (sc) – a recessive mutation that reduces the number of thoracic bristles. This mutation is linked with a long inversion on the X-chromosome, which is necessary for the suppression of crossing-over, which could change the existing gene combinations on the treated chromosome.[41-43]

Three-day old Canton-S males (N = 30) were starved in empty bottles for 5 h prior to treatment and then transferred and fed in bottles with a filter paper soaked with a 5.0 % solution of the acetone extract of *A. artemisiifolia* for 24 h. After another 24 h of recovery on standard medium, each male was mated individually to three Basc females in 30 bottles, which made brood I. After two days, the males were transferred to new vials with three Basc line virgins (brood II) and after three days, the males were transferred again into fresh vials with three Basc virgins (brood III). These males stayed with the females for three days and were then removed. The females were left for five days to lay eggs, and then they were removed. The solvent 1.0 % sucrose served as the negative control.

After F_1 emerged, brother–sister mating was allowed for several days and 10 females from each vial were placed individually into new vials. Each vial would give the progeny of one treated X-chromosome.

In F_2, the phenotypes were scored according to eye colour and shape. The absence of wild type males indicated the presence of a recessive lethal induced by the test substance.

The stocks were maintained and all experiments were performed under optimal conditions (t = 25 °C, relative humidity = 60 %, 12/12 h light/dark regime) on a standard nutritive medium for *Drosophila* (corn flour, yeast, agar, sugar and nipagin to prevent mould and infection).

The total number of treated X-chromosomes is equal to the sum of the lethal and non-lethal cultures and the frequency of sex-linked recessive lethal was calculated from the ratio of the number of lethal to the total number of treated X-chromosomes. The significance of the difference in the percentage of lethals was tested using the test for big independent samples (testing of difference between proportions).[44,45]

RESULTS AND DISCUSSION

Many different kinds of metabolites, including sesquiterpene lactones, phenolics, coumarins and flavonoids have been identified from *A. artemisiifolia* L.[9,11,13,15] In the above-ground parts of *A. artemisiifolia* L. species, many struc-

turally different sesquiterpene lactones were identified, among them coronopilin, dihydropartenolide, psilostachyin, cumanin, peruvin, artemisiifolin, isabelin, ambrosin and cumamin.[11]

The following lactones were identified in the methanol extract of common ragweed, *A. artemisiifolia*: the sesquiterpene lactones psilostachyins A, B and C, paulitin and isopaulitin. Psylostachyins A and C block cells in mitosis, which act as novel checkpoint inhibitors of G2/DNA damage.[46] It was suggested that these compounds can easily bind covalently to target proteins.[47]

On the basis the present experimental results, it was concluded that the ambrosia pollen acetone extract contained two lactones, ambrosin and artesovin in the ratio of 3:1 (Fig. 1). The structures of the sesquiterpene lactones ambrosin and artesovin were assigned on the basis of UV–Vis, IR, ^{1}H-NMR, ^{13}C-NMR and mass spectral data.

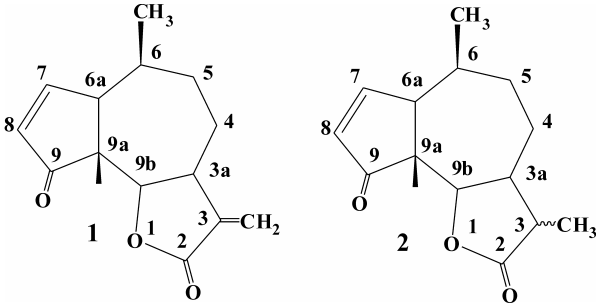

Fig. 1. Chemical structure of ambrosin (**1**) and artesovin (**2**).

*Ambrosin (6,9a-dimethyl-3-methylene-3,3a,4,5,6,6a-hexahydroazuleno[4,5-*b*]-furan-2,9(9a*H*,9b*H*)-dione*) ***(1)***. Light white crystals; m.p. 146−148 °C (ethanol); R_f = 0.36 (6:4 benzene:ethyl acetate); IR (KBr, cm^{-1}): 1755 (γ-lactone), 1710, 1660 (enone (lactone)), 1605 (enone (cyclpentenone)), 1420, 1378, 1140; ^{1}H-NMR (200 MHz, $CDCl_3$, δ, ppm): 1.01 (3H, *d*, CH_3–C_6, ^{3}J = 6.8 Hz), 1.12−1.48 (4H, *m*, C_4, C_5), 1.33 (3H, *s*, CH_3–C_{9a}), 1.71 (1H, *m*, C_6), 2.39 (1H, *t*, C_{6a}, $^{3}J_{6a,6}$ = 5.9 Hz, $^{3}J_{6a,7}$ = 5.8 Hz), 2.69 (1H, *bq*, C_{3a}, $^{3}J_{3a,9b}$ = 6.7 Hz, $^{3}J_{3a,4}$ = 6.2 Hz, $^{3}J_{3a,4}$ = 6.1 Hz), 4.21 (1H, *d*, C_{9b}, $^{3}J_{3a,9b}$ = 6.7 Hz), 5.65 (1H, *d*, CH_2 methylene, J = 1.3 Hz), 6.20 (1H, *d*, C_8, $^{3}J_{7,8}$ = 6.3 Hz), 6.25 (1H, *d*, CH_2 methylene, J = 1.3 Hz), 7.02 (1H, *dd*, C_7, $^{3}J_{7,8}$ = 6.3 Hz, $^{3}J_{6a,7}$ = 5.8 Hz); ^{13}C-NMR (50 MHz, $CDCl_3$, δ, ppm): 169.97 (C_2), 138.7 (C_3), 43.43 (C_{3a}), 24.8 (C_4), 31.15 (C_5), 33.9 (C_6), 49.56 (C_{6a}), 169.87 (C_7), 128.1(C_8), 211.8 (C_9), 53.47 (C_{9a}), 79.65 (C_{9b}), 18.79 (CH_3 at C_6), 17.6 (CH_3 at C_{9a}), 120.05 (CH_2 methylene); MS (*m*/*z*): 93, 125, 145, 166, 189, 204, 231, M^+ 246.1256; UV–Vis (EtOH) (λ_{max}, nm (ε, L mol^{-1} cm^{-1})): 217 (17100) (α,β-unsaturated ketone and α,β-unsaturated γ-lactone) and 343 (35) (carbonyl).

*Artesovin (3,6,9a-trimethyl-3,3a,4,5,6,6a-hexahydroazuleno[4,5-*b*]furan--2,9(9a*H*,9b*H*)- dione) (**2**)*. White crystals; m.p. 165–167 °C (diethyl ether), R_f = 0.50 (benzene:ethyl acetate = 6:4); IR (KBr, cm^{-1}): 1775 (γ-lactone), 1707, 1615 (eno-

ne (cyclpentenone)), 1420, 1370, 1140; ^{1}H-NMR (200 MHz, $CDCl_3$, δ, ppm): 1.01 (3H, *d*, CH_3–C_6, ^3J = 6.7 Hz), 1.12–1.48 (4H, *m*, C_4,C_5), 1.21 (3H, *d*, CH_3–C_6, ^3J = 7.7 Hz), 1.34 (3H, *s*, CH_3–C9a), 1.68 (1H, *m*, C_6), 2.47 (1H, *t*, C_{6a}, $^3J_{6a,6}$ = 7.9 Hz, $^3J_{6a,7}$ = 5.5 Hz), 2.61 (1H, *dq*, C_3, $^3J_{3,Me}$ = 7.7 Hz, $^3J_{3a,3}$ = 9.5 Hz), 2.81 (1H, *m*, C_{3a}, $^3J_{3a,9b}$ = 10.4 Hz, $^3J_{3a,3}$ = 9.5 Hz), 4.61 (1H, *d*, C_{9b}, $^3J_{3a,9b}$ = = 10.4 Hz), 6.07 (1H, *d*, C_8, $^3J_{7,8}$ = 5.9 Hz), 7.1 (1H, *dd*, C_7, $^3J_{7,8}$ = 5.9 Hz, $^3J_{6a,7}$ = 5.5 Hz); ^{13}C-NMR (50 MHz, $CDCl_3$, δ, ppm): 178.3 (C_2), 41.4 (C_3), 45.4 (C_{3a}), 26.7 (C_4), 30.1 (C_5), 35.2 (C_6), 51.6 (C_{6a}), 161.7 (C_7), 129.2(C_8), 209.8 (C_9), 54.7(C_{9a}), 85.6 (C_{9b}), 19.9 (CH_3 at C_6), 20.6 (CH_3 at C_{9a}), 12.9 (CH_3 at C_3); MS (*m*/*z*): 125, 145, 166, 189, 203, 218, 233, M^+ 248.1412; UV–Vis (EtOH) (λ_{max}, nm (ε, L mol^{-1} cm^{-1})): 212 (15100) (α,β-unsaturated ketone) and 347 (20) (carbonyl).

The presence of these lactones is in accordance with the presence of ambrosic acid,[15] which acts as a precursor in intra molecular cyclization to form ambrosin and ambrosin-like lactones.[48]

The bacterial strains used in the present study demonstrated the commercial potential of the pollen as an active allelochemical[36] and antimicrobial mixture for some human and phytopatogenic bacteria.[6]

The results of the antibacterial activity (disc diffusion and microdilution methods) of the primary acetone extract of the pollen of *A. artemisiifolia* L. on some bacteria are presented in Table I.

TABLE I. Antibacterial activity of the acetone extract of *A. artemisiifolia* pollen (*Pseudomonas fluorescens*, 0.063 mg ml^{-1}, *Bacillus mycoides*, 0.039 mg ml^{-1})

Microorganism	Zones of inhibition, mm[a,b,c]					*MIC*[e] mg mL^{-1}
	Concentration of extract				Standard[d]	
	5 mg	10 mg	5 mg	10 mg	10 mg	
	24 h		48 h		24 h	
B. mycoides	18.0±1	23.0±0.5	14.5±0.5	17.0±1	22.0±0.5	3.50
P. fluorescens	17.0±1	21.0±1	0	17.0±1	13.2±0.7	1.25
A. tumefaciens	19.0±0.5	24.0±1	18.0±0.5	23.0±0.5	15.0±0.5	2.50
E. carotovora	17.0±0.5	23.0±0.5	0	21.0±0.5	14.1±0.5	2.25
E. cloacae	19.0±1	26.0±0.5	0	24±1	10.6±0.5	2.50
A. chroococcum	18.0±1	23.0±0.3	0	22±1	10.6±0.5	2.50
K. pneumoniae	20.0±0.5	22.0±0.5	17±1	18±1	12.5±0.5	6.50
S. aureus	21.0±0.3	23.0±0.5	22.0±0.5	23±0.5	12.5±0.5	4.75
Proteus sp.	0	0	0	0	36.8±0.7	0
P. aeruginosa	0	0	0	0	0	0

[a]Mean value±*SD*, *N* = 3; [b]"0" absence of antimicrobial activity; [c]solvent control acetone was negative; [d]sinacilin, 10 mg/disc; [e]*MIC* standard: sinacilin, 1.0 mg mL^{-1}

These results show that the acetone extract has a high antibacterial activity against all ten investigated bacteria. All the cultures had in common the fact that the investigated concentrations had an inhibitory effect on the development of a

large number of bacteria. The 10 mg concentration exhibited a high degree of inhibition over the 24 h development period. The inhibition level varied from 21.0 to 26.0 mm. The extract demonstrated the highest inhibition of the growth of *Enterobacter cloacae*, with an inhibition zone of 26.0 mm, while the inhibition zone with the other bacteria ranged from 21.0 to 24.0 mm.[37]

In the 48 h-cultures, a slight decrease in the inhibition was registered, except for the *Staphylococcus aureus* culture.[49] There were two significant differences with this bacterium. The first one is that the inhibition ability of the extract was very similar for the samples of 5 and 10 mg of extract per disc and it varied from 21.0 to 23.0 mm. The second difference is that the level of inhibition remained the same as that after 24 h of development.[50,51] For most of the examined bacteria, after a time period of 48 h with 10 mg of extract, a slight decrease of the effect was observed, while no bacteriostatic effect was registered after 48 h with 5 mg of extract in the case of the *Pseudomonas fluorescens*, *Erwinia carotovora*, *E. cloacae* and *Azotobacter chroococcum* cultures. In general, this class of bacteria was more resistant.

Such a resistance could be due to the permeability barrier provided by the cell wall or the membrane accumulation mechanism.[34,35] Compared to the standard ability of sinacilin, with 10 mg per disc, all of the examined bacteria experienced an inhibitory growth in the presence of the acetone extract of 5−12 mm, *i.e.*, the bacterial growth was 1−1.5 times slower than the one in the presence of the antibiotic.

The examined concentration of the acetone extract did not demonstrate an inhibition effect on the growth of *Proteus* sp. and *Pseudomonas aeruginosa*. The absence of susceptibility of these bacteria to the pollen extract was not entirely unexpected, and it is based both on their anatomical and biochemical characteristics.[34]

At a concentration of 5 mg extract per disc during a 24-hour incubation, the extract was bacteriostatic towards eight of the ten examined bacteria, which can be the result of the inhibition process of the synthesized cell wall. At a concentration of 10 mg extract, the effect was bactericidal and is contingent to the inhibition of the bacterial metabolism, with the most prominent inhibition recorded on the ribosome protein synthesis.[34,35] The minimal inhibitory concentration of the acetone extract of *A. artemisiifolia* pollen varied between 1.25−6.50 mg mL^{-1}.

Previous literature geared us towards the fact that the existing pollen proteins are responsible for their allergenic activity,[52] although there is no proof whether the lactones present actually contribute to such a reaction using the existing proteins as their carriers.[53]

Using a short test for the detection of mutagenicity in *Drosophila melanogaster in vivo* conditions, it was found that the examined plant extract had mutagenic properties.[54] The results are given in Table II.

TABLE II. Frequencies of SLRL mutations after treatment of *D. melanogaster* males with the acetone extract of *A. artemisiifolia* L. pollen

	Sucrose (negative control)	*Ambrosia* (test group)	$t_{s/a}$
I brood ∑	300	244	1.65
No. of lethals	5	10	$p > 0.05$
% of lethals	1.67	4.10	
II brood ∑	269	204	4.40
No. of lethals	5	26	$p < 0.001$[a]
% of lethals	1.86	12.74	
III brood ∑	252	236	2.97
No. of lethals	6	20	$p < 0.01$
% of lethals	2.38	8.47	
I+II+III ∑	821	684	5.41
No. of lethals	16	56	$p < 0.001$
% of lethals	1.95	8.19	

[a]Statistically significant difference

At the 5 % concentration level, it induced sex-linked recessive lethal mutations on the X-chromosome of *Drosophila melanogaster* males, which were treated acutely with this extract (broods II and III). The frequency of the germinative mutations induced by the pollen components was significantly higher than the frequency of mutations induced by sucrose (negative control). The obtained results show that the spermatic cell line (brood II) was especially sensitive to the influence of the examined extract.

The results of the experiments showed that the tested extract induced recessive, lethal X-linked mutations in postmeiotic germinative cell lines – spermatids and premeiotic line – spermatocytes, while the spermatozoids were more resistant to the genotoxic effects of the examined agent.

Since the established statistically significant difference in the increase in the frequency of sex-related lethals in the tested group of *D. melanogaster* males, compared to the negative control, represents a positive result, it was concluded that a chemical component in the ambrosia pollen induced the mutations in male germinative cells of this eukaryotic species. The statistically significant differentces in the II and III broods, shown in Table II, confirm the same sensitivity of germinative cells of the premeiotic (diploid) and postmeiotic stage (haploidic spermatids).

The experimentally proven genotoxicity of the ambrosia pollen extract demands further examination, *i.e.*, determination of the chemical structure of the pollen agent which is capable of inducing hereditary genetic changes in this *in vivo* system.

CONCLUSIONS

Two lactones, ambrosin and artesovin (in the ratio of 3:1, respecttively), were identified in the acetone extract of *Ambrosia artemisiifolia* pollen.

At a 5.0 mg concentration, the acetone extract of ambrosia pollen was bacteriostatic for most of the examined bacteria during a 24-h development period, while at the 10 mg concentration, the acetone extract of ambrosia pollen was bactericidal for eight out of the ten examined bacteria. The *MIC* of the acetone extract of *A. artemisiifolia* pollen varied between 1.25−6.50 mg mL^{-1}.

The lactones mixture (3:1) of ambrosin and artesovin induced recessive lethal mutations on the X-chromosome of *Drosophilia melanogaster* in the II and III broods. As a result, it was concluded that spermatides and spermatocytes were the more sensitive stages of spermatogenesis than the others were.

Acknowledgement. This study was financially supported by Grants No. 142025 and 143008 from the Ministry of Science of the Republic of Serbia.

И З В О Д

ХЕМИЈСКИ САСТАВ И БИОЛОШКА АКТИВНОСТ АЦЕТОНСКОГ ЕКСТРАКТА ПОЛЕНА *Ambrosia artemisiifolia* L.

СЛАВИЦА СОЛУЈИЋ[1], СЛОБОДАН СУКДОЛАК[1], НЕНАД ВУКОВИЋ[1], НЕДА НИЋИФОРОВИЋ[1] и СНЕЖАНА СТАНИЋ[2]

[1]Институт за хемију и [2]Институт за биологију, Природно–математички факултет, п пр. 12, 34000 Крагујевац

У овом раду испитан је хемијски састав ацетонског екстракта полена *Ambrosia artemisiifolia* и његова антимикробна и генотоксична биолошка активност. Идентификована су два лактона: амброзин и артезовин. Антимикробна активност ацетонског екстракта полена *A. artemisiifolia* одређена је применом дифузионе и микродилуциона метода у Mueller-Hinton хранљивом агару. Различите количине екстракта су нанете на дискове (5 и 10 mg) и испитане на 10 различитих бактерија. Минимална инхибиторна концентрација је у опсегу од 1,25–6,50 mg mL^{-1}. Генотоксични ефекат ацетонског екстракта полена *A. artemisiifolia* испитан је применом SLRL теста на еукариотском модел систему *Drosophilia melanogaster.*

(Примљено 10. децембра 2007, ревидирано 21. маја 2008)

REFERENCES

1. M. Gajić, in *The Flora of Serbia*, M. Josifović, Ed., Vol. VIII, Serbian Academy of Sciences and Arts, Department of Natural and Mathematical Sciences, Belgrade, 1973, p. 63 (in Serbian)
2. H. L. Jones, *Plant Physiol.* **28** (1953) 123
3. B. J. Genton, J. A. Shykoff, T. Girand, *Mol. Ecol.* **14** (2005) 4275
4. P. Comtois, *Ragweed in Europe*, in *Proceedings of the 6th International Congress on Aerobiology Satellite Symposium*, (1998), ALK Abello, Horsholm, Denmark, (1998), p. 3
5. W. Deen, A. L. Hunt, J. C. Swanton, *Weed Sci.* **46** (1998) 561
6. P. Wang, Ch. H. Kong, Ch. X. Zhang, *Molecules* **11** (2006) 549
7. A. Avjioglu, T. Hough, M. Singh, R. B. Knox, *Adv. Cell.r Mol. Biol. Plants* **2** (1994) 336

8. C. Brunei, P. M. Bedard, M. Lavoie, M. Jobin, J. Hebert, *J. Allergy Clin. Immunol.* **89** (1992) 76
9. E. Bloszyk, U. Rychlewska, B. Czezapanska, M. Budesinsky, B. Drozdz, M. Holub, *Collect. Czech. Chem. Commun.* **57** (1992) 1092
10. K. J. Rugutt, F. R. Fronczek, S. G. Franzblau, I. M. Warner, *Acta Crystallogr. Sect. A: Struct. Rep. Online* **57** (2001) 323
11. A. Y. Parkhomenko, O. A. Andeeva, E. T. Oganesyan, M. N. Ivashev, *Pharm. Chem. J.* **5** (2005) 149
12. J. P. David, A. J. O. De Santos, M. L. S. Da Guedes, J. M. David, H. B. Chai, J. M. Pezzuto, C. K. Angerhoferand, A. Cordell, *Pharm. Biol.* **37** (1999) 165
13. Y. Tamura, M. Hatori, K. Konno, H. Honda, H. Ono, M. Yoshida, *Chemoecology* **14** (2004) 113
14. E. Rodriguez, G. H. N. Towers, J. C. Mitchell, *Phytochemistry* **15** (1976) 1573
15. S. Milosavljević, V. Bulatović, M. Stefanović, *J. Serb. Chem. Soc.* **64** (1999) 397
16. A. K. Picman, *Biochem. Syst. Ecol.* **14** (1986) 255
17. P. Bonnarme, A. Djian, A. Latrasse, G. Feron, C. Ginies, A. Durand, J. L. Le Quere, *J. Biotechnol.* **56** (1997) 143
18. G. Feron, L. Dufosse, E. Pierard, P. Bonnarme, J. L. Le Quere, H. E. Spinnler, *Appl. Environ. Microbiol.* **62** (1996) 2826
19. M. S. Mantovani, C. S. Takahashi, W. Vichnewiski, *Brazil. J. Genet.* **16** (1993) 967
20. D. H. Jones, H. J. Kim, H. C. Donnelly, *Res. Commun. Chem. Pathol. Pharmacol.* **34** (1981) 161
21. V. G. Vaidya, I. Kulkarni, B. A. Nagasampagi, *Indian J. Exp. Biol.* **16** (1978) 1117
22. J. T. MacGregor, *Food Cosmetics Toxicol.* **15** (1977) 225
23. R. V. Burin, R. Canalle, J. L. C. Lopes, W. Vichnewski, C. S. Takahashi, *Teratogen. Carcinogen. Mutagen.* **21** (2001) 383
24. J.-H. Kim, L. Liu, S.-O. Lee, Y.-T. Kim, K.-R You, D.-G. Kim, *Cancer Res.* **65** (2005) 6312
25. Y. Kishida, H. Yoshikawa, A. Myoui, *Clin. Cancer Res.* **13** (2007) 59
26. J. M. Woynarowki, J. Konopa, *J. Mol. Pharmacol.* **19** (1981) 97
27. T. J. Schmidt, *Bioorg. Med. Chem.* **5** (1997) 645
28. J. D. Haues, D. J. Pulford, *Mutagenesis* **12** (1995) 163
29. H. Nago, M. Matsumoto, S. Nakai, *Biosci. Biotech. Biochem.* **57** (1993) 2107
30. R. A. Sessa, M. H. Bennett, M. J. Lewis, J. W. Mansfield, M. H. Beale, *J. Biol. Chem.* **275** (2000) 26877
31. A. T. Y. Lau, Y. Wang, J.-F. Chiu, *J. Cell. Biochem.* **104** (2008) 657
32. J. J. Ross, J. T. Arnason, H. C. Birnboin, *Planta Med*. **65** (1999)126
33. S. Zhang, C. N. Ong, H. M. Shen, *Cancer Lett*. **208** (2004) 143
34. C. H. Neu, D. T. Gootz, *Antimicrobial Chemotherapy*, http://gsbs.utmb.edu/microbook/ /ch011.htm (October 13, 2008)
35. *General Principles of Antimicrobial Therapy: Introduction*, http://www.becomenatural.com (October 13, 2008)
36. Z. Kebede, *Allelopathic Chemicals*, www.colostate.edu/Depts/Entomology/courses/ en570/ /papers_1994/kebede.html (April 25, 1996)
37. N. D. Cheronis, J. B. Entrikin, E. M. Hodnett, *Semimicro Qualitative Organic Analysis*, Part 6, 3rd Edition, Interscience, New York, 1965, p. 90

38. NCCLS, *Methods for dilution antimicrobial susceptibility tests for bacteria that grow aerobically*, Approved Standard NCCLS Publication M7-A2, Vilanova, 1990
39. S. Umesha, P. A. Richardson, P. Kong, C. X. Hong, *J. Microbiol. Methods* **72** (2008) 95
40. W. R. Lee, S. Abrahamson, R. Valencie, E. S. von Halle, F. E. Wurgler, S. Zimmering, *Mutation Res.***123** (1983) 183
41. G. M. Williams, H. Mori, I. Hirono, M. Nagao, *Mutation Res.* 79 (1980) 1
42. R. W. Morgan, G. Hoffman, *Mutat. Res.* **114** (1983) 19
43. R. B. Haveland-Smith, *Mutat. Res.* **91** (1981) 285
44. D. Simić, J. Knežević-Vukčević, B. Vuković-Gačić, in *Proceedings of the First Conference on Medicinal and Aromatic Plants Southeast European Countries*, Arandjelovac, Serbia, Association for Medicinal and Aromatic Plants of Southeast European Countries, **97** (2000) 104
45. B. Petz, *Basic statistical method for non-mathematical use*, SNL Zagreb, Croatia, 1985 (in Serbian)
46. C. M. Sturgeon, K. Craig, C. Brown, N. T. Rundle, R. Anderson, M. Roberge, *Planta Med.***71** (2005) 938
47. S. A. Borchardt, E. J. Allain, J. J. Michels, G. W. Stearns, R. F. Kelly, W. F. McCoy, *Appl. Environ. Microbiol.* **67** (2001)3174
48. W. Herz, V. Heywood, B. L. Turner, J. B. Harborne, *Biology and Chemistry of the Compositeae*, Academic Press, New York, 1977
49. D. van den Berghe, A. J. Vlietinck, in *Methods in Plant Biochemistry Assays for Bioactivity 6*, P. M. Dey, J. B. Harborne, K. Hostettman, Eds., Academic Press, London, 1991, p. 47
50. J. C. Chalchat, Z. Maksimović, S. Petrović, M. Gorunović, *J. Essent. Oil Res.* **16** (2004) 270
51. J. A. Akande, Y. Hayashi, *World J. Microbiol. Biotechnol.* **14** (1998) 235
52. S. Wan, T. Yuan, S. Bowdish, L. Wallace, S. D. Russell, Y. Luo, *Am. J. Botany* **89** (2002) 1843
53. H. Moller, A. Spiren, A. Svensson, B. Gruvberger, M. Hindsen, M. Bruze, *Cont. Dermatitis* **47** (2002) 157
54. B.-Y. Zhi, Y. Yan , Z.-L. Yi, *J. Ethnopharmacol.* **116** (2008) 89.

www.shd.org.rs

Journal of the Serbian Chemical Society

JSCS@tmf.bg.ac.yu • www.shd.org.rs/JSCS

J. Serb. Chem. Soc. 73 (11) 1051–1061 (2008)
JSCS–3786

UDC 535–31+665.7.038.5–188:547.979.8+
+547.953
Original scientific paper

UV-effects on antioxidant activity of selected carotenoids in the presence of lecithin estimated by DPPH test

DRAGAN CVETKOVIĆ and DEJAN MARKOVIĆ*

Faculty of Technology, University of Niš, Bulevar oslobođenja 124, Leskovac, Serbia

(Received 19 March, revised 29 May 2008)

Abstract: The effects of ultraviolet radiation (UV) on the antioxidant action of three selected carotenoids (*β*-carotene, lycopene and lutein) in the presence of a lipoidal lecithin mixture were studied by the DPPH (1,1-diphenyl-2-picrylhydrazyl) test. The test is based on the measurement of the decrease of the free DPPH radical absorbance at 517 nm caused by the antioxidant action of carotenoids, which appeared to be strongly affected by UV-action. The high-energy input of the involved UV-photons plays a major governing role.

Keywords: carotenoids; UV-light; lipids; antioxidants.

INTRODUCTION

The destruction of stratospheric ozone has led to an increase of biologically damaging UV radiation at ambient levels (mainly UV-B, 280–320 nm). As a consequence, many crucial, biologically important, processes of global importance have been affected, such as DNA replication[1] and photosynthesis,[2] among others. UV radiation can generally initiate many harmful free radical mediated processes, lipid peroxidation (LP) being one of most important among them. Lipid peroxidation appears as a precursor of many pathological processes which finish in some form of cancer, such as skin melanoma.[3,4]

Reactive oxygen species (ROS), such as hydroxy (•OH) or peroxy (ROO•) radicals, are known as typical lipid peroxidation initiators. They can be created either through a variety of chemical reactions, by typical lipid radicals producers,[5] or by external stresses, implying very commonly external radiation and UV light.[6–9]

Lipid peroxidation is partly controlled *in vivo* by antioxidants action.[10] In recent years, carotenoids have attracted wide research interest as potential antioxidants. Numerous studies report that higher consumption of carotenoids and lower risk of cancer and cardiovascular diseases are mutually connected; the antioxidant action of carotenoids is attributed to their conjugated chemical structures, having multiple potential sites approachable for attack by ROS species.[11–13]

* Corresponding author. E-mail: markovic57@info-net.co.yu
doi: 10.2298/JSC0811051C

It is already known that UV radiation certainly affects carotenoids antioxidant function *in vivo*,[2] although the involved mechanisms have not yet been elucidated. The aim of this paper was to study *in vitro* the effects of UV radiation on the antioxidant activities of three plants photosynthetic accessory pigments (*β*-carotene, lycopene and lutein), in the presence of a lipoidal target (lecithin). The mixture was irradiated with UV-B and UV-C light. The antioxidant activities of investigated carotenoids (and their dependence on UV radiation) were monitored by the DPPH test.

EXPERIMENTAL

The pigments were isolated from two plant species (*β*-carotene and lutein from spinach (*Spinacia oleracea*) leaves, and lycopene from tomato (*Lycopersicon esculentum*) fruits purchased at a local market.

Lecithin Epikuron 100 P, a mixture of phospholipids, was a gift from ICN Galenika, Belgrade. It was manufactured by Degusa Texturant Systems, Hamburg, Germany. The lipid content was: phosphatidylethanolamine 18.0 %, phosphatidic acid 8.3 %, phosphatidylinositol 14.1 % and phosphatidylcholin 21.7 %.* The lecithin mixture was kept in the dark to prevent the auto-oxidation process during daylight. Although dark auto-oxidation could not be eliminated, it was taken into account during the calculation of LP yield.

Pigments extraction from spinach leaves

The photosynthetic pigments were extracted using a modified method of Svec.[14,15] Leaves without midribs (FW 30 g) were dropped into boiling water, which was quickly replaced (after 1–2 min) with cold water. After drying between paper towels at 40–75 °C, the leaves were separated and placed in a methanol/petroleum ether mixture (60:30 v/v), with occasional agitation, for 30 min. The methanol removes water from the plant material and the petroleum ether picks up the pigments before they undergo secondary reactions. The deep-green extract was decanted through a cotton pad. The leaves were re-extracted twice with an equal volume of the extraction mixture. The pooled extracts were diluted with 120 ml of saturated NaCl solution, whereby most of the pigments remained in the petroleum ether layer. The remaining aqueous methanol layer was re-extracted with 40 ml of a mixture containing 40–75 °C petroleum ether and diethyl ether (1:1 v/v), to ensure the solubility of pigments in the organic phase. The successive extracts were treated by the same procedure. The final pigment extract contained various forms of chlorophyll as well as the accessory pigments, carotenoids (carotenes and xanthophylls).

Isolation of carotenoids from spinach extract by column chromatography

The carotenoid fractions were isolated using a modified procedure of Svec[15] and Brockman[16] – column chromatography with silica gel (silica gel 60, Merck, 0.063–0.200 mm) as adsorbent and benzene/acetone mixture for the elution. The benzene/acetone ratio was changed from the initial 1:0 to the final 1:1, to permit an easier elution of the polar fractions. *β*-Carotene appears first (eluted with benzene only), followed by the chlorophylls (eluted with benzene/acetone, 7:1) and the xanthophylls fraction – lutein (eluted with benzene/acetone, 6:1–1:1). The column chromatogram is shown in the supplement (Fig. S1). The fractions were dried and resuspended in hexane. The fractions were identified by comparing their Vis spectra with standards spectra (Fig. S2).

* The acid value, peroxide number and iodine number were controlled and found to be correct.

Pigments extraction from tomato fruits

Tomato fruit (FW 8.0 g) was thoroughly mixed with 40 ml of ethanol. The slurry was stirred until the tomato material was no longer sticky (about 3 min). Ethanol was removed by vacuum filtration. The tomato residue was mixed with 60 ml of a mixture of acetone and petroleum ether (1:1). The extract was collected by vacuum filtration and the residue rewashed with the same solvent mixture (20 ml) in order to improve the yield. The filtrate was transferred to a small separating funnel and mixed with 50 ml of saturated NaCl solution. The organic layer was rewashed twice, the first one with 50 ml of 10 % K_2CO_3 and then with 50 ml of distilled water. Finally, approximately 1 g of anhydrous $MgSO_4$ was added to dry the organic layer. After 10–15 min the solution was vacuum filtered to remove the drying agent.

Isolation of carotenoids from tomato extract by column chromatography

The lycopene fraction was isolated by column chromatography with alumina (aluminum oxide 90, Merck, 0.063–0.200 mm) as adsorbent and petroleum ether/acetone mixture for the elution. The mixture ratio was changed from an initial 10:0.1 to a final 9:1, to permit the easier elution of lycopene. β-Carotene appeared first (eluted with petroleum ether/acetone mixture of 10:0.1), followed by the lycopene fraction (eluted with a 9:1 ratio of the mixture). The column chromatogram is shown in the supplement (Fig. S3). The collected fractions were dried, resuspended and identified in hexane (Fig. S2).

HPLC analysis of carotenoid fractions

A high percentage of carotenoids in the separated fraction was evidenced by HPLC analysis. The analysis was performed on a Hewlett Packard HPLC system under isocratic conditions; column: Zorbax Eclipse XDB-C18; mobile phase: acetonitrile/methanol/ethyl acetate, 60:20:20; flow rate: 0.5 ml min^{-1}. The monitoring wavelengths were 445 nm for β-carotene and lycopene and 447 nm for lutein. The HPLC chromatograms are shown in the supplement (Figs. S4 and S5).

UV treatment

Continuous irradiation of the samples was performed in a cylindrical photochemical reactor "Rayonnet", with 14 symmetrically placed lamps with emission maxima in two different ranges: 254 nm (UV-C) and 300 nm (UV-B). The samples were irradiated in quartz cuvettes (1 cm×1 cm×4.5 cm) placed on a circular rotating holder. The total energy flux reaching the samples was about 25 and 21 W m^{-2} for 254 and 300 nm, respectively.

Vis spectroscopy

Vis spectra of the samples before and after UV radiation were recorded on Varian Cary-100 spectrophotometer. All spectra were recorded from 400 to 800 nm.

DPPH test

The interaction of carotenoids with the 1,1-diphenyl-2-picrylhydrazyl (DPPH) radical was estimated according to the modified method of Choi et al.[17,18] A methanolic solution of DPPH radical (1 ml, 0.3×10^{-3} mol l^{-1}) was added after irradiation to 2.5 ml of an aqueous mixture lecithin:pigment, 50:1 (v/v). The initial concentrations were 8.5×10^{-6} mol l^{-1} and 5×10^{-5} mol l^{-1} for lecithin and carotenoids, respectively. The irradiated reaction mixture was incubated at room temperature for 20 min in the dark. Vis spectra were recorded from 400 to 800 nm. The absorbance was read at 517 nm, being the wavelength of maximal absorption of the DPPH radical. Aliquots of the new mixtures (lecithin and the pigments) were irradiated with UV-C and UV-B light for various time intervals and the DPPH test was repeated. The following formula was used to calculate the scavenging capacity of DPPH in the presence of carotenoids:[17]

$$\text{Scavenging capacity (\%)} = 100 - (A_{\text{sample}} - A_{\text{blank}}) \times 100 / A_{\text{control}}$$

where A_{sample} is the absorbance at 517 nm of an irradiated lecithin/pigments mixture, 50:1, treated afterwards with a solution of DPPH radicals, A_{blank} is the absorbance at 517 nm of the unirradiated lecithin/pigments mixture and A_{control} is the absorbance at 517 nm of a methanolic solution of the DPPH radical.

RESULTS

The structures of the investigated carotenoids (lycopene, β-carotene, and lutein) are shown in Fig.1.

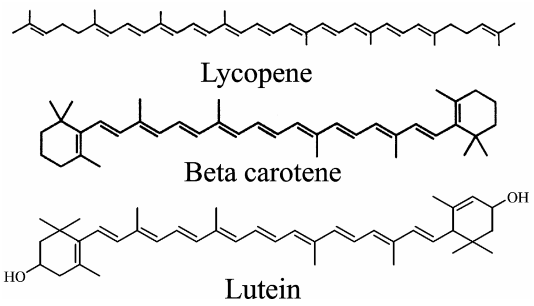

Fig. 1. Structures of the investigated carotenoids.

The DPPH scavenging capacity in presence of the investigated carotenoids as a function of time of irradiation with UV-B light is shown in Fig. 2.

The DPPH scavenging capacity in presence of the investigated carotenoids as a function of time of irradiation with UV-C light is shown in Fig. 3.

The calculated slopes from the corresponding DPPH scavenging capacity plots are given in Table I. The calculated average declinations (*i.e.*, relative errors), based on 4 other repeated experiments, for each point on the plots (Figs. 2 and 3), are 10.65 (UV-C) and 6.70 % (UV-B) for β-carotene; 10.25 (UV-C) and 4.3 % (UV-B) for lycopene; 10.2 (UV-C) and 4.9 % (UV-B) for lutein.

DISCUSSION

The influence of UV radiation on the antioxidant activities of carotenoids was spectrophotometrically analyzed by the DPPH test. DPPH is a stable free radical that produces a violet color in methanolic solution. The DPPH radical (containing a lone electron) is characterized by a strong absorption at 517 nm. As the electron is paired off in the presence of another free radical scavenger, the absorption decreases and the resulting discolorations are stoichiometric with respect to the number of electrons taken up.[18,19] Hence, the concentration of stable free DPPH radical is reduced in the presence of an antioxidant molecule. This fact was employed to evaluate its antioxidant activity.

Specifically, DPPH test was performed in this study in the presence of a mixture of lipoidal components (lecithin) in the reaction system, exposed to a long continuous UV-radiation, resulting in the formation of lipid and lipoperoxy radicals.[20] DPPH test is not specific for any particular radical species present in the

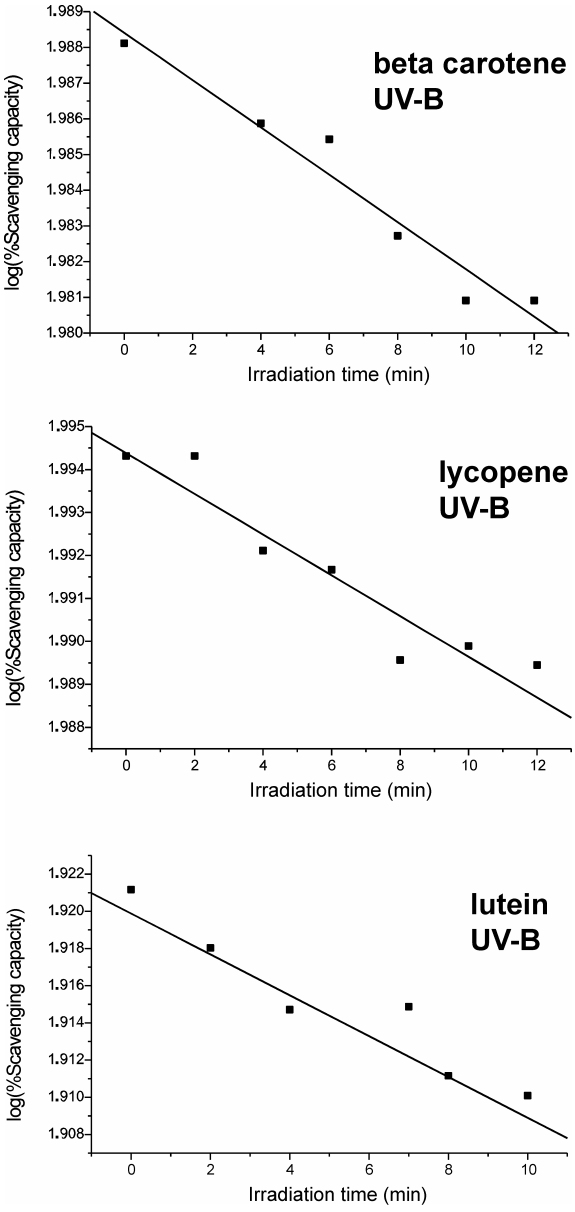

Fig. 2. Decrease of the scavenging capacity of DPPH toward β-carotene, lycopene and lutein with increasing time of UV-B irradiation (300 nm), in the presence of lecithin.

reaction mixture, *i.e.*, a DPPH radical may potentially react with carotenoid radicals (CAR), as well as with lipid radicals, or with any other radicals species potentially present in solution (at the same time, CAR radicals, obviously present in the system, certainly react with lipid radicals, thereby performing anti-oxidant lipid protection, but this cannot be followed by the DPPH test). Nevertheless, the relative linearity of the plots of scavenging capacity *vs.* irradiation time for all three

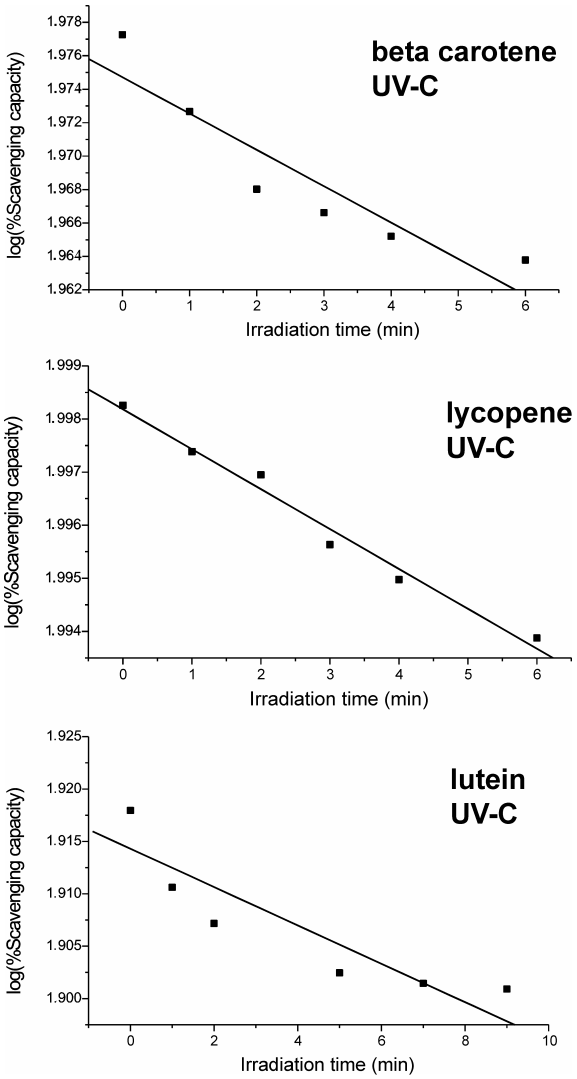

Fig. 3. Decrease of scavenging capacity of DPPH toward β-carotene, lycopene and lutein, with increasing time of UV-C irradiation (254 nm), in the presence of lecithin.

studied carotenoids with both UV-B and UV-C radiation, which was also found in the presence of the same carotenoids using the other, more specific TBA–MDA test,[21] offers arguments in favor of DPPH–CAR combination. Therefore, the results presented in Table I give a comparative view of the three "pigment slopes" calculated from kinetic measurements and represent decreasing rates of the radical scavenging capacities of DPPH toward the three carotenoids (k) during prolonged UV-irradiation in both ranges (UV-C and UV-B). Clearly, there is noticeable drop in the k values following a change from UV-C (254 nm) to UV-B (300 nm) photons. This fact confirms that the decreasing rates of the scavenging capacities of carotenoids toward the DPPH radical during prolonged UV-irradi-

ation depend on the energy input of the UV-photons (the $k_{UV\text{-}C}/k_{UV\text{-}B}$ ratio was 3.3 for β-carotene, 2.1 for lycopene and 1.7 for lutein). This type of dependence of the antioxidant activity of carotenoids on the energy input of the UV photons was also observed in a previous work, in which the antioxidant activities of carotenoids were studied by the TBA–MDA test.[21]

TABLE I. The values of rate constants (k / 10^{-3} min^{-1}) of the decreasing anti-oxidant activities of the investigated carotenoids (β-carotene, lycopene and lutein) monitored by the DPPH test in a solution containing the carotenoids (1.0×10^{-6} mol l^{-1}) and soybean lecithin (8.5×10^{-6} mol l^{-1}) mixture, during UV-irradiation with emission maxima in two different ranges: 254 (UV-C) and 300 nm (UV-B). Concentration of DPPH radicals was 3×10^{-4} mol l^{-1}

λ / nm	254	300
β-Carotene	2.17	0.66
Lycopene	1.05	0.49
Lutein	1.83	1.10

It is necessary to underline that the DPPH test is an indirect and partial measure of the antioxidant activities of carotenoids. As it is already known, the antioxidant activities of carotenoids in a free radicals rich medium (chain-breaking antioxidant activities) may be expressed through at least three possible pathways.[11–13] These actions are performed *via* the participation of carotenoid radical cations ($CAR^{+\bullet}$), radical anions ($CAR^{-\bullet}$), or neutral radicals ($CAR^{\bullet}$). These radicals in complex systems, as studied in this work, are short-lived and therefore undetectable by the techniques used in this research. Thus, possibly, only a part of the antioxidant activities of carotenoids (through recombination with lipid and lipoxy radicals, thus preventing lipid oxidation) was able to be followed through recombination with DPPH radicals. The fact that the scavenging capacity of DPPH decreased linearly in the presence of all carotenoids when irradiated with UV-B and UV-C radiation (Figs. 2 and 3) is not a direct implication, *per se*, that DPPH and CAR radicals underwent mutual recombination. However, since the same type of kinetics (linear, 1st order) was found for all carotenoids in the same medium (Figs. 2 and 3) not only by this method, but by the much more selective TBA–MDA test,[21] where decreases of the carotenoids antioxidant activities were clearly connected with some (though slight) suppression of the lipid peroxidation chain mechanism, implies most probably DPPH–CAR combination, rather than the possible scavenging by DPPH of other radicals present in the system. This does not absolutely negate the latter possibility but suggests its marginal character compared to the main presumption. Hence, the effects of UV radiation on at least a part of the antioxidant activities of carotenoids can be followed by this method.

It is also evident that decrease of the scavenging capacity of DPPH toward the three carotenoids under UV-irradiation depends on the chemical structure of the carotenoid. Lycopene has the lowest values of k in respect to the other investtigated carotenoids. Thus lycopene (being non-cyclized and containing no oxy-

gen atoms) was the most resistant toward the effects of UV-irradiation. Contrary to this, lutein (containing two oxygen atoms and two cyclic rings, Fig. 1) was the most sensitive to UV-B irradiation, while keeping the "middle position" between β-carotene and lycopene, concerning its resistance toward UV-C irradiation (Table I). It has already been reported that the antioxidant activities of xanthophylls were more sensitive in comparison to carotenes to changes in the energy of the incident UV photons in hexane solution.[22] This reinforces the conclusion, since another conjugated dienes test was employed in that study.

CONCLUSIONS

To conclude, (*i*) although the DPPH test is not very selective, the results enable the speculation that DPPH radical preferably recombine with carotenoid radicals present in the system; (*ii*) the measured UV radiation mediated decrease in the antioxidant activities of the carotenoids through recombination with DPPH radicals highly depends on the energy of the UV photons employed and on the chemical structures of the carotenoid; (*iii*) antioxidant activity of lycopene appeared to be most resistant to UV radiation.

Acknowledgements. D. Cvetković is a recipient of a fellowship granted by Ministry of Science of the Republic of Serbia.

SUPPLEMENT

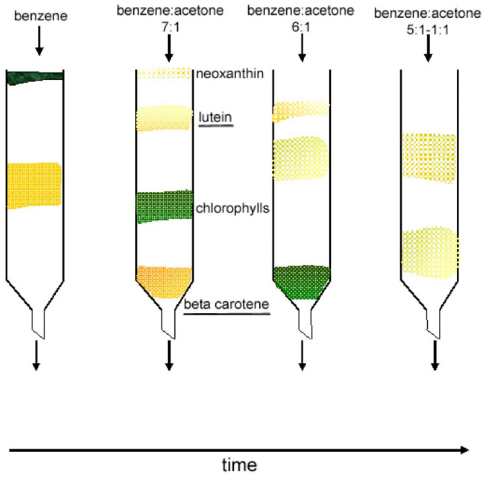

Fig. S1. Column chromatography of spinach leaves extract.

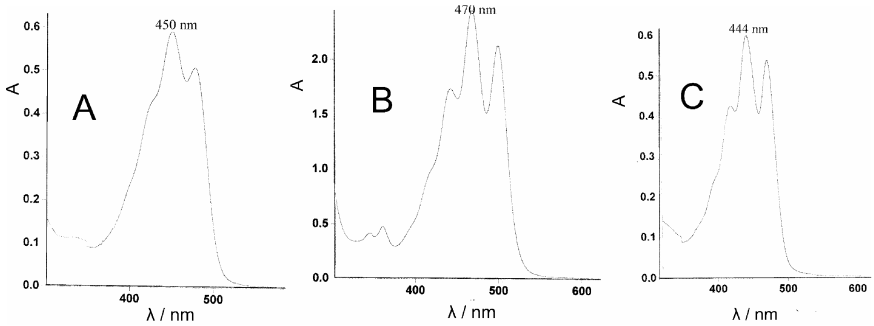

Fig. S2. Vis spectra of isolated carotenoid fractions in hexane: β-carotene (A), lycopene (B) and lutein (C).

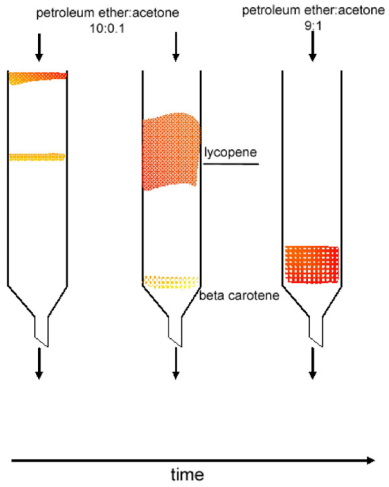

Fig. S3. Column chromatography of tomato fruit extract.

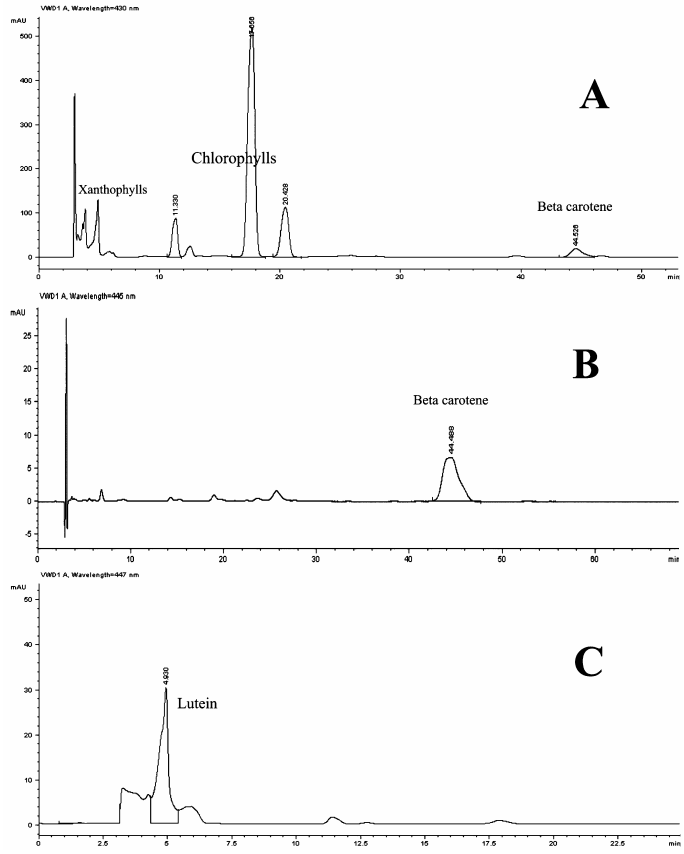

Fig. S4. HPLC chromatograms of spinach leaves extract (A), β-carotene fraction (B) and lutein fraction (C).

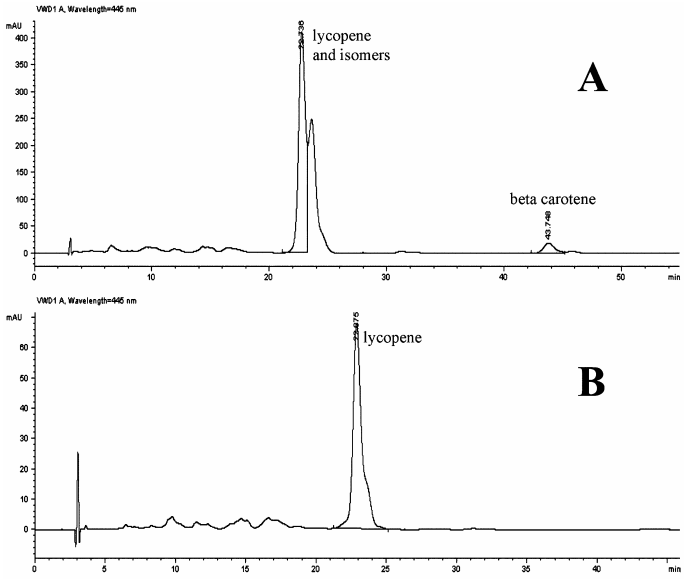

Fig. S5. HPLC chromatograms of tomato fruit extract (A) and lycopene fraction (B).

И З В О Д

ЕФЕКАТ УЛТРАЉУБИЧАСТОГ ЗРАЧЕЊА НА АНТИОКСИДАТИВНУ АКТИВНОСТ КАРОТЕНОИДА У ПРИСУСТВУ ЛЕЦИТИНА ПРАЋЕН ПРЕКО DPPH ТЕСТА

ДРАГАН ЦВЕТКОВИЋ и ДЕЈАН МАРКОВИЋ

Технолошки факултет, Универзитет у Нишу, Булевар ослобођења 124, Лесковац

Ефекти ултраљубичастог зрачења на антиоксидативну активност три изабрана каротеноида (β-каротена, ликопена и лутеина) у присуству липоидалне смеше лецитина, праћени су преко DPPH теста. DPPH тест се заснива на мерењу опадања абсорбанције DPPH радикала на 517 nm, проузрокованог антиоксидативним деловањем присутних каротеноида. Антиоксидативна активност испитиваних каротеноида примарно зависи од интензитета ултраљубичастог зрачења, односно од енергије упадних UV фотона.

(Примљено 19. марта, ревидирано 29. маја 2008)

REFERENCES

1. M. Ichihashi, M. Ueda, A. Budiyannto, T. Bito, M. Oka, M. Fukunaga, K. Tsuru, T. Horikawa, *Toxicology* **189** (2003) 21
2. A. H. Teramura, L. H. Ziska, in *Photosynthesis and the Environment*, N. R. Baker, Ed., Kluwer Academic Publishers, Dordrecht, 1996, p. 436
3. A. R. Young, *Eur. J. Dermatol.* **6** (1996) 225
4. A. Ouhtit, H. N. Ananthaswamy, *J. Biomed. Biotechnol.* **1** (2001) 5
5. J. Aikens, T. A. Dix, *Arch. Biochem. Biophys.* **305** (1993) 516
6. M. G. J. Heijman, H. Nauta, Y. K. Levine, *Radiat. Phys. Chem.* **26** (1985) 73
7. D. Z. Marković, L. K. Patterson, *Photochem. Photobiol*. **49** (1989) 531
8. D. Z. Marković, T. Durand, L. K. Patterson, *Photochem. Photobiol*. **51** (1990) 389
9. D. Z. Marković, *J. Serb. Chem. Soc.* **66** (2001) 309
10. K. E. Heim, A. R. Tagliaferro, D. J. Bobilya, *J. Nutr*. *Biochem.* **13** (2002) 572
11. G. W. Burton, K. U. Ingold, *Science* **224** (1984) 569
12. N. Palozza, I. Krinsky, *Methods Enzymol.* **213** (1992) 403
13. M. G. Simić, *Methods Enzymol.* **213** (1992) 444
14. W. A. Svec, in *Chlorophylls*, H. Scheer, Ed., CRC Press, Boca Raton, 1991, p. 89
15. W. A. Svec, in *The Porphyrins*, D. Dolphin, Ed., Academic Press, New York, 1978, p. 342
16. H. Brockman, N. Risch, in *Chlorophylls*, H. Scheer, Ed., CRC Press, Boca Raton, 1991, p. 103
17. C. W. Choi, S. C. Kim, S. S. Hwang, B. K. Choi, H. J. Ahn, M. Y. Lee, S. H. Park, S. K. Kim, *Plant Sci.* **163** (2002) 1161
18. C. Sanchez-Moreno, *Food Sci. Technol. Int.* **8** (2002) 121
19. Y. Matsushita, R. Suzuki, E. Nara, A. Yokoyama, K. Miyashita, *Fisheries Sci*. **66** (2000) 980
20. A. Sujak, J. Gabrielska, W. Grudzinski, *Arch. Biochem. Biophys.* **371** (1999) 301
21. D. Cvetković, D. Marković, *Radiat. Phys. Chem.* **77** (2008) 34
22. D. Cvetković, D. Marković, *J. Serb. Chem. Soc.* **72** (2007) 235.

www.shd.org.rs

Journal of the Serbian Chemical Society

JSCS@tmf.bg.ac.yu • www.shd.org.rs/JSCS

J. Serb. Chem. Soc. 73 (11) 1063–1071 (2008)
JSCS–3787

UDC 542.9+547.571+547.551:542.913:66.092+
+548.7:615.281–188
Original scientific paper

Designing, synthesis and spectral characterization of Schiff base transition metal complexes: DNA cleavage and antimicrobial activity studies

N. RAMAN*, S. SYED ALI FATHIMA and J. DHAVEETHU RAJA

Research Department of Chemistry, VHNSN College, Virudhunagar-626 001, India

(Received 24 October 2007, revised 24 April 2008)

Abstract: A new series of transition metal complexes of Cu(II), Ni(II), Co(II) and Zn(II) have been designed and synthesized using a Schiff base (L) derived from 4-aminoantipyrine, benzaldehyde and *o*-phenylenediamine. The structural features were derived from their elemental analyses, magnetic susceptibility and molar conductivity, as well as from mass, IR, UV–Vis, ^{1}H-NMR and ESR spectral studies. The FAB mass spectral data and elemental analyses showed that the complexes had a composition of the ML type. The UV–Vis and ESR spectral data of the complexes suggested a square-planar geometry around the central metal ion. The magnetic susceptibility values of the complexes indicated that they were monomeric in nature. Antimicrobial screening tests were also performed against four bacteria, *viz*. *Salmonella typhi*, *Staphylococcus aureus*, *Escherichia coli*, and *Bacillus subtilis* and three fungi, *viz*. *Aspergillus niger*, *Aspergillus flavus* and *Rhizoctonia bataicola.* These data gave good results in the presence of metal ion in the ligand system. The nuclease activity of the above metal complexes shows that only the copper complex cleaves CT DNA in the presence of an oxidant.

Keywords: 4-aminoantipyrine; benzaldehyde; *o*-phenylenediamine; CT DNA; Schiff base; antimicrobial activity.

INTRODUCTION

Schiff bases of 4-aminoantipyrine and their complexes have a variety of applications in biological, clinical, analytical and pharmacological areas.[1,2] Studies of new kinds of chemotherapeutic Schiff bases are now attracting the attention of biochemists.[3,4] Earlier works reported that some drugs showed increased activity when administered as metal complexes rather than as organic compounds. According to cell biology, deoxyribonucleic acid (DNA) is the primary target molecule for most anticancer and antiviral therapies. Investigations of the interaction of DNA with small molecules are basic work in the design of new types of pharmaceu-

* Corresponding author. E-mail: drn_raman@yahoo.co.in
doi: 10.2298/JSC0811063R

tical molecules. Since the chemical nuclease activity of transition metal complexes was discovered in the 1980s,[5–7] studying the interaction model and the mechanism of transition metal complexes with DNA and exploring the application of metal complexes in antineoplastic medication, molecular biology and bioengineering have been hotspots in recent years. Certain kinds of metal complexes when interacted with DNA could induce the breakage of DNA strands by appropriate methods. Thus, with cancer genes, after DNA strands are cleaved, the DNA double strands break. The replication ability of cancer gene is then destroyed. Ueda *et al*.[8] showed that the copper complex could cleave DNA in the presence of ascorbate or hydroquinone. It was suggested that the reductive capability of the reductants had a critical influence on DNA cleavage. The coordinating property of the 4-aminoantipyrine ligand was modified to give flexible ligand systems, formed by condensation with a variety of reagents, such as aldehydes, ketones, thiosemicarbazides, carbazides, *etc*.[9–19] A literature search revealed that no work has been undertaken on the condensation of 4-aminoantipyrine, benzaldehyde and *o*-phenylenediamine. Hence, in this paper, the synthesis, characterization, antimicrobial and DNA studies of transition metal complexes containing Schiff base derived from 4-aminoantipyrine, benzaldehyde and *o*-phenylenediamine are described.

EXPERIMENTAL

Syntheses of Schiff base (L)

An ethanolic solution (20 mL) of 1-phenyl-2,3-dimethyl-4-aminopyrazol-5-one (4-aminoantipyrine) (2.03 g, 0.010 mol) was added to an ethanolic solution of benzaldehyde (1.06 g, 0.010 mol). On stirring, a yellow-coloured solid (**I**) separated, which was filtered and recrystallised from ethanol. Compound **I** (2.9 g, 0.010 mol) was added to an ethanolic solution (20 mL) of *o*-phenylenediamine (0.54 g, 0.0050 mol). The mixture was refluxed for *ca.* 30 h after addition of anhydrous potassium carbonate. The potassium carbonate was filtered off from the reaction mixture and the solvent was evaporated. A dark yellow solid product (L) was separated, which was filtered and recrystallised from ethanol (Fig. 1).

Syntheses of complexes

A solution of metal(II) chloride in ethanol (2.0 mmol) was refluxed with an ethanolic solution of the Schiff base (2.0 mmol) for *ca.* 5 h. Then the solution was reduced to one-third of its volume on a water bath. The precipitated solid complex was filtered and washed thoroughly with ethanol and dried under vacuum.

Antimicrobial activity

The in vitro biological screening effects of the investigated compounds were tested against the bacteria: *Salmonella typhi*, *Staphylococcus aureus*, *Escherichia coli*, and *Bacillus subtilis* by the well-diffusion method, using agar nutrient as the medium. The antifungal activities of the compounds were evaluated by the well-diffusion method against the fungi, *viz*. *Aspergillus niger*, *Aspergillus flavus* and *Rhizoctonia bataicola* cultured on potato dextrose agar as medium. Stock solutions (10 mM) were prepared by dissolving the compounds in DMSO and the solutions were serially diluted in order to find the *MIC* values. In a typical procedure,[20] a well

was made on the agar medium inoculated with micro-organisms. The well was filled with the test solution using a micropipette and the plate was incubated, 24 h for bacteria and 72 h for fungi, at 35 °C. During this period, the test solution diffused and the growth of the inoculated micro-organisms was affected. The concentration at which an inhibition zone developed, was noted.

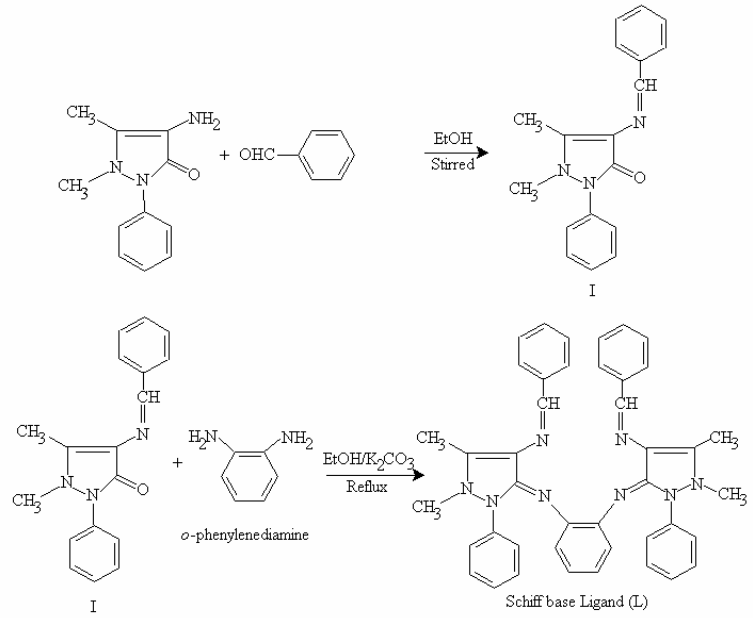

Fig. 1. Formation of Schiff base ligand (L).

Gel electrophoresis

The gel electrophoresis experiments were performed by incubation at 35 °C for 2 h as follows. The samples containing 30 μM calf thymus DNA (CT DNA), 50 μM of each complex and 50 μM H_2O_2 in 50 mM tris-HCl buffer (pH 7.2) were electrophoresed for 2 h at 50 V on a 1 % agarose gel using tris-acetic acid–EDTA buffer, pH 8.3. After electrophoresis, the gel was stained using 1.0 μg cm^{-3} ethidium bromide (EB) and photographed under UV light.

Apparatus and reagents

All reagents, 4-aminoantipyrine, benzaldehyde, *o*-phenylenediamine and various metal(II) chlorides were Merck products and used as supplied. Anhydrous grade ethanol, DMF and DMSO were purified according to standard procedures. Microanalytical data of the compounds were recorded at the Sophisticated Analytical Instrument Facility, Central Drug Research Institute (SAIF, CDRI), Lucknow. The FAB mass spectra of the ligand and its complexes were recorded at SAIF, Indian Institute of Technology, Mumbai. The IR spectra of the samples were recorded on a Perkin-Elmer 783 spectrophotometer in the 4000–400 cm^{-1} range using KBr pellets. The UV–Vis spectra were recorded on a Shimadzu UV-1601 spectrophotometer using DMF as the solvent. The X-band ESR spectra of the complex were recorded at 300 and 77 K at IIT, Mumbai, using tetracyanoethylene (TCNE) as the g-marker. Magnetic susceptibility measurements of the complexes were carried out on a Guoy balance using copper sulphate as the calibrant. The molar conductance of the complexes was measured using a Systronic conductivity bridge. Solutions of CT DNA in 50 mM NaCl/50 mM tris-HCl

(pH 7.2) gave the ratio of the UV absorbance at 260 and 280 nm, A_{260}/A_{280}, of *ca.* 1.8–1.9, indicating that the DNA was sufficiently free of protein contamination. The DNA concentration was determined by the UV absorbance at 260 nm after 1:100 dilution. The molar absorption coefficient was taken as 660 m^2 mol^{-1}. Stock solutions were kept at 4 °C and used after not more than 4 days. Doubly distilled H_2O was used to prepare the buffer. The antimicrobial activities of the ligand and its complexes were carried out by the well-diffusion method.

RESULTS AND DISCUSSION

The analytical data for the ligand and complexes together with some physical properties are summarized in Table I. The analytical data of the complexes correspond well with the general formula ML, where M = Cu(II), Ni(II), Co(II) and Zn(II); L = $C_{42}H_{38}N_8$. The magnetic susceptibilities of the complexes at room temperature were consistent with square planar geometry around the central metal ion. The higher conductivity values of the chelates support the electrolytic nature of the metal complexes.

TABLE I. Physical characterization, analytical, molar conductivity, Λ_m, and magnetic susceptibility data of the ligand and the complexes

Cmpd.	Molecular formula	Colour	M.p. °C	Found (Cacld.), %				Λ_m / Ω^{-1} cm^2 mol^{-1}	μ_{eff} / μ_B
				M	C	H	N		
L	$C_{42}H_{38}N_8$	Yellow	198	–	77.0 (77.0)	5.8 (5.9)	17.1 (17.2)	–	–
$[CuL]Cl_2$	$CuC_{42}H_{38}N_8Cl_2$	Black	260	8.8 (8.9)	70.2 (70.3)	5.3 (5.4)	15.6 (15.6)	94	1.73
$[NiL]Cl_2$	$NiC_{42}H_{38}N_8Cl_2$	Light green	272	8.2 (8.3)	70.7 (70.7)	5.4 (5.4)	15.7 (15.7)	98	–
$[CoL]Cl_2$	$CoC_{42}H_{38}N_8Cl_2$	Brown	242	8.2 (8.2)	70.7 (70.7)	5.4 (5.3)	15.7 (15.6)	93	3.52
$[ZnL]Cl_2$	$ZnC_{42}H_{38}N_8Cl_2$	Colour-less	265	9.2 (9.3)	70.0 (70.0)	5.3 (5.4)	15.6 (15.6)	82	–

The FAB mass spectra of the Schiff base and its complexes were compared for their stoichiometric compositions. The molecular ion peak for the ligand was observed at 654 *m*/*z*, which is also supported by the "nitrogen rule", since the compound possesses eight nitrogen atoms. For the copper complex, the molecular ion peak appeared at 791 *m*/*z*, which confirms the stoichiometry of metal complexes as being of the ML type. It is also supported by the mass spectra of other complexes. This composition is further supported by the microanalytical data (Table I).

The IR spectra provide valuable information regarding the nature of the functional group attached to the metal atom.[21] The spectrum of the free Schiff base ligand shows two –C=N bands in the region 1650–1565 cm^{-1}, which is shifted to lower frequencies in the spectra of all the complexes (1620–1530 cm^{-1}), indicating the involvement of the –C=N nitrogen in the coordination to the metal ion.[22] Coordination of the Schiff base to the metal through the nitrogen atom is expected to reduce the electron density in the azomethine link and lowers the

$\nu_{C=N}$. All the complexes show bands in 1090–1100 cm^{-1} and 700–750 cm^{-1} regions and can be assigned to phenyl ring vibrations.[23] Assignment of the proposed coordination sites is further supported by the appearance of medium bands at 450–500 cm^{-1}, which could be attributed to ν_{M-N}.[24,25]

The electronic absorption spectra of the Schiff base, Cu(II), Co(II), and Ni(II) complexes were recorded at 300 K. The absorption region, assigned and the proposed geometry of the complexes are given in Table II. Based on these data, a square-planar geometry was assigned to the complexes. These values are comparable with those of the other reported complexes.[26–29]

TABLE II. Electronic absorption spectral data of the compounds

Cmpd.	Solvent	Absorption, cm^{-1}	Band assignment	Geometry
L	DMSO	26525	ILCT	–
$[CuL]Cl_2$	DMSO	27397, 23752	ILCT, $^2B_1g \rightarrow {}^2A_1g$	Square-planar
$[CoL]Cl_2$	DMSO	27173, 19417	ILCT, $^1A_1g \rightarrow {}^1B_1g$	Square-planar
$[NiL]Cl_2$	DMSO	27027,25380, 19607	ILCT, $^1A_1g \rightarrow {}^1A_2g$, $^1A_1g \rightarrow {}^1B_1g$	Square-planar

The ESR spectra of the copper complex, recorded in DMSO solution at 300 and 77 K are shown in Figs. 2a and 2b. The frozen solution spectrum shows a well resolved four line spectrum and no features characteristic for a dinuclear complex. This is also supported by the magnetic moment of copper complex (1.73 μ_B) which confirms the mononuclear nature of the complex. The spin Hamiltonian parameters for the copper complex were calculated from the spectra. The g-tensor values of this copper(II) complex can be used to derive the ground state. In square-planar complexes, the unpaired electron lies in the $d_{x^2-y^2}$ orbital, giving $^2B_{1g}$ as the ground state with $g_{\|} > g_{\perp} > 2$, while the unpaired electron lies in the d_{z^2} orbital, giving $^2A_{1g}$ as the ground state with $g_{\perp} > g_{\|} > 2$. From the observed values, it is clear that $g_{\|}(2.17) > g_{\perp}(2.03) > 2$, which suggests that the complex is square planar. This is further supported by the fact that the unpaired electron lies predominantly in the $d_{x^2-y^2}$ orbital,[30–33], as was evident from the value of the exchange interaction term G, estimated from the expression:

$$G = \frac{g_{\|} - 2.0023}{g_{\perp} - 2.0023}$$

If $G > 4.0$, the local tetragonal axes are aligned parallel or only slightly misaligned. If $G < 4.0$, significant exchange coupling is present and the misalignment is appreciable. The observed value for the exchange interaction parameter for the copper complex ($G = 6.5$) suggests that the local tetragonal axes are aligned parallel or slightly misaligned and that the unpaired electron is present in the $d_{x^2-y^2}$ orbital. This result also indicates that the exchange coupling effects are not operative in the present complex.[34]

Based on the above spectral data, the structure of the complex given in Fig. 3 is proposed.

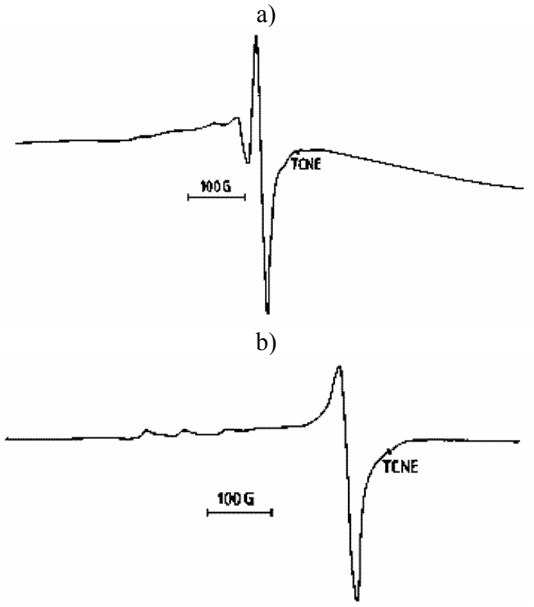

Fig. 2. ESR spectra of the copper complex at 300 (a) and 77 K (b).

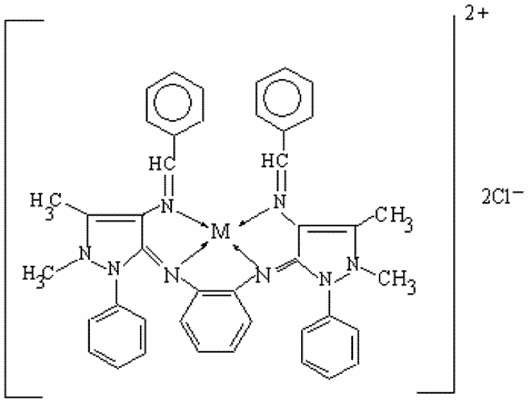

Fig. 3. The proposed structure of the Schiff base complexes.

For in vitro antimicrobial activity, the investigated compounds were tested against the bacteria *Salmonella typhi*, *Staphylococcus aureus*, *Escherichia coli*, and *Bacillus subtilis* and the fungi *Aspergillus niger*, *Aspergillus flavus* and *Rhizoctonia bataicola*. The minimum inhibitory concentration (*MIC*) values of the investigated compounds are summarized in Table III. From the table, the observed *MIC* values indicate that most of the complexes have higher antimicrobial activity than the free ligand. Such increased activity of the metal chelates can be explained on the basis of the chelation theory. On chelation, the polarity of the metal ion is reduced to a greater extent due to the overlap of the ligand orbital and partial sharing of the positive charge of the metal ion with donor groups. Further, it increases the delocalization of the π-electrons over the whole chelate ring

and enhances the penetration of the complexes into lipid membranes and the blocking of the metal binding sites in the enzymes of micro-organisms. These complexes also disturb the respiration process of the cell and thus block the synthesis of proteins, which further restricts the growth of the organism.[18]

TABLE III. Antibacterial activity of the Schiff base ligand and its metal complexes

Cmpd.	*MIC* / 10^{-2} M						
	S. typhi	*S. aureus*	*E. coli*	*B. subtilis*	*A. niger*	*A. flavus*	*R. bataicola*
L	5.8	5.9	5.7	6.1	7.1	7.2	7.3
$[CuL]Cl_2$	4.6	4.4	4.6	4.8	5.8	5.9	6.1
$[CoL]Cl_2$	4.7	5.1	4.9	4.9	5.7	5.9	5.6
$[NiL]Cl_2$	4.8	4.9	4.6	4.7	5.4	5.7	5.8
$[ZnL]Cl_2$	4.9	4.8	4.7	4.8	6.0	5.9	6.1

The cleavage efficiency of the complexes compared to that of the control is due to their efficient DNA-binding ability. The metal complexes were able to convert supercoiled DNA into open circular DNA. The general oxidative mechanism is proposed to account for DNA cleavage by hydroxyl radicals *via* abstraction of hydrogen atoms from sugar units and predict the release of specific residues arising from transformed sugars, depending on the position from which the hydrogen atom is removed.[35] The cleavage was inhibited by free radical scavengers, implying that hydroxyl radical or peroxy derivatives mediate the cleavage reaction. The reaction was modulated by metallocomplexes bound hydroxyl radical or a peroxo species generated from the co-reactant H_2O_2.

In the present study, a CT-DNA gel electrophoresis experiment was conducted at 35 °C using the synthesized complexes in the presence of H_2O_2 as an oxidant. As can be seen from the results in Fig. 4, at very low concentration, only the copper complex exhibited nuclease activity in the presence of H_2O_2. The control experiment using DNA alone (lane 1) did not show any significant cleavage of CT-DNA, even with a longer exposure time. From the observed results, it can be concluded that the copper complex (lane 2), cleaves DNA as compared to the control DNA while the other complexes (lanes 3–5) do not cleave DNA in the presence of H_2O_2. Furthermore, the presence of a smear in the gel diagram indicates the presence of radical cleavage.[36]

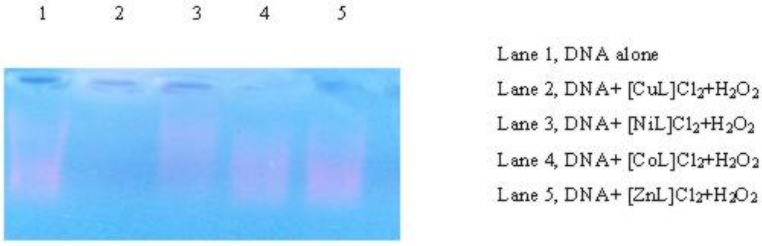

Fig. 4. Changes in the agarose gel electrophoretic pattern of CT-DNA induced by H_2O_2 and the metal complexes.

CONCLUSIONS

In this paper, the coordination chemistry of a Schiff base ligand, obtained from the reaction of 4-aminoantipyrine, benzaldehyde and *o*-phenylenediamine is described. Cu(II), Co(II), Ni(II) and Zn(II) complexes were synthesized using the above Schiff base ligand and characterized by spectral and analytical data. Based on these data, a square-planar geometry was assigned to the complexes. The metal complexes have higher antimicrobial activity than the ligand. The interaction of these complexes with CT-DNA was investigated by gel electrophoresis, from the results of which it was observed that the copper complex cleaved DNA in the presence of H_2O_2 as compared to the control DNA and the other complexes.

Acknowledgements. The authors express their sincere thanks to the Managing Board, Principal and Head of the Department of Chemistry, VHNSN College, Virudhunagar for their constant encouragement and providing the research facilities. J. D. thanks the Tamil Nadu Government for financial assistance.

И З В О Д

ДИЗАЈН, СИНТЕЗА И СПЕКТРАЛНА КАРАКТЕРИЗАЦИЈА ШИФОВИХ БАЗА ПРЕЛАЗНИХ МЕТАЛНИХ КОМПЛЕКСА: РАСКИДАЊЕ DNA И АНТИМИКРОБНО ПРОУЧАВАЊЕ

N. RAMAN, S. SYED ALI FATHIMA и J. DHAVEETHU RAJA

Research Department of Chemistry, VHNSN College, Virudhunagar-626 001, India

Дизајнирана је серија комплекса прелазних метала Cu(II), Ni(II), Co(II) и Zn(II) и добијена помоћу Шифове базе (L) изведене из 4-аминопирина, бензалдехида и *o*-фенилендиамина. До структурних облика се дошло на основу њихових елементалних анализа, магнетне сусцептибилности, моларне проводљивости, масених, IR, UV–Vis, ^{1}H-NMR и ESR спектралних проучавања. FAB масени спектри и елементална анализа показали су да је састав комплекса ML типа. UV–Vis и ESR спектри комплекса сугеришу квадратно-планарну геометрију око централног металног јона. Вредности магнетне сусцептибилности комплекса указују на то да су они мономерне природе. Антимикробни тест је спроведен на четири бактерије, и то *Salmonella typhi*, *Staphylococcus aureus*, *Escherichia coli*, и *Bacillus subtilis* и три гљивице, и то *Aspergillus niger*, *Aspergillus flavus* и *Rhizoctonia bataicola*. Тест је дао добре резултате у присуству металног јона у лигандном окружењу. Нуклеазна активност поменутих комплекса показује да само комплекс бакра раскида CT DNA у присуству оксиданта.

(Примљено 24. октобра 2007, ревидирано 24. априла 2008)

REFERENCES

1. T. Hitoshi, N. Tamao, A. Hideyuki, F. Manabu, M. Takayuki, *Polyhedron* **16** (1997) 3787
2. T. Punniyamurthy, S. J. S. Kalra, J. Iqbal, *Tetrahedron Lett*. **36** (1995) 8497
3. Y. K. Choi, K. H. Chjo, S. M. Park, N. Doddapaneni, *J. Electrochem. Soc*. 142 (1995) 4107
4. B. Katia, L. Simon, R. Anne, C. Gerard, D. Francoise, M. Bernard, *Inorg. Chem*. **35** (1996) 387
5. D. S. Sigman, D. R. Graham, V. D. D'Aurora, A. M. Stern, *J. Biol. Chem*. **254** (1979) 12269
6. V. M. Downey B. R. Que, A. G. So, *Biochem. Biophys. Res. Commun*. **93** (1980) 264

7. E. L. Marshall, D. R. Graham, K. A. Reith, *Biochemistry* **20** (1981) 224
8. J. I. Ueda, M. Takai, Y. Shimazu, *Arch. Biochem. Biophys*. **357** (1998) 231
9. P. K. Radhakrishnan, *Polyhedron* **5** (1986) 995
10. R. C. Maurya, D. D. Mishra, M. Pandey, P. Shukla, R. Rathour, *Synth. React. Inorg. Met. Org. Chem*. **23** (1992) 167
11. R. K. Agarwal, P. Garg, H. Agarwal, D. Chandra, *Synth. React. Inorg. Met. Org. Chem*. **27** (1997) 251
12. L. Singh, N. Tyagi, N. P. Dhaka, S. K. Sindhu, *Asian J. Chem*. **11** (1999) 503
13. N. K. Jha, D. M. Joshi, *Synth. React. Inorg. Met. Org. Chem*. **16** (1986) 947
14. P. Thomas, G. Parmeshwaran, *J. Indian Chem. Soc*. **69** (1992) 117
15. A. P. Mishra, V. Srinivastava, S. K. Srinivastava, *Synth. React. Inorg. Met. Org. Chem*. **25** (1995) 21
16. R. Shankar, R. P. Kumar, S. K. Ramalingam, *Polyhedron* **5** (1986) 991
17. A. Kriza, A. Reiss, S. Florea, T. Caproiu, *J. Indian Chem. Soc*. **77** (2000) 207
18. N. Dharmaraj, P. Viswanathamurthi, K. Natarajan, *Transition Met. Chem*. **26** (2001) 105
19. N. Raman, A. Kulandaisamy, K. Jeyasubramanian, *Polish J. Chem*. **76** (2002) 1085
20. M. J. Pelczar, E. C. S. Chan, N. R. Krieg, *Microbiology*, 5th Ed., McGraw Hill Inc., New York, 1998
21. L. Heri, J. Taganine, B. M. Gupta, *Indian J. Chem*. **40A** (2000) 999
22. S. K. Sengupta, O. P. Pandey, J. K. Pandey, G. K. Pandey, *Indian J. Chem.* **40A** (2001) 887
23. K. Nakamoto, *Infrared and Raman Spectra of Inorganic and Coordination Compounds*, 3rd Ed., Wiley, New York, 1997
24. M. B. H. Howlader, M. S. Islam, *Indian J. Chem.* **46A** (2007) 440
25. M. Thankamony, K. Mohanan, *Indian J. Chem*. **46A** (2007) 247
26. M. F. Iskander, L. Ei-Syed, K. Z. Ismail, *Transition Met. Chem.* **4** (1979) 225
27. M. Thankamony, K. Mohanan, *Indian J. Chem*. **46A** (2007) 249
28. M. Thomas, M. K. M. Nair, R. K. Radhakrishan, *Synth. React. Inorg. Met. Org. Chem.* **25** (1995) 471
29. R. M. Kadam, M. D. Sastry, M. K. Bhide, S. A. Chavan, J. V. Yakhmi, O. Khan, *Chem. Phys. Lett*. **281** (1997) 292
30. M. Base, K. Ohta, Y. Babu, M. D. Sastry, *Chem. Phys. Lett*. **324** (2000) 330
31. R. K. Ray, G. B. Kauffman, *Inorg. Chim. Acta* **173** (1990) 207
32. K. Jeyasubramanian, S. A. Samath, S. Thambidurai, R. Murugesan, S. K. Ramalingam, *Transition Met. Chem*. **20** (1996) 76
33. A. M. F. Benial, V. Ramakrishnan, R. Murugesan, *Spectrochim. Acta* **56A** (2000) 2775
34. L. J. Boucher, E. C. Tyanan, T. F. Yen, *Electron Spin Resonance of Metal Chelates*, Plenum Press, New York, 1969
35. G. Prativel, M. Pitie, J. Bernadou, B. Meunier, *Angew. Chem. Int. Ed. Eng*. **30** (1991) 702
36. A. M. Thomas, A. D. Naik, M. Nethaji, A. R. Chakravarty, *Indian J. Chem*. **43A** (2004) 691.

www.shd.org.rs

Journal of the Serbian Chemical Society

JSCS@tmf.bg.ac.yu • www.shd.org.rs/JSCS

J. Serb. Chem. Soc. 73 (11) 1073–1082 (2008) UDC 661.8+547.362–32+549.766.321:615.281
JSCS–3788 *Original scientific paper*

Transition metal complexes with oxygen donor ligands: a synthesis, spectral, thermal and antimicrobial study

VAIBHAV N. PATANGE[1]*, RAJENDRA K. PARDESHI[1] and BALASAHEB R. ARBAD[2]

[1]*Department of Chemistry, Shri Chhatrapati Shivaji College, Omerga, Dist-Osmanabad – 413606, Maharashtra and* [2]*Department of Chemistry, Dr. Babasaheb Ambedkar Marathwada University, Aurangabad – 431004, Maharashtra, India*

(Received 14 November 2007, revised 6 June 2008)

Abstract: Transition metal complexes of chalcones derived from the condensation of 3-acetyl-6-methyl-2*H*-pyran-2,4(3*H*)-dione (dehydroacetic acid) and *p*-methoxybenzaldehyde (HL^1) or *p*-nitrobenzaldehyde (HL^2) were synthesized and characterized by elemental analysis, conductometry, thermal analysis, magnetic measurements, IR, ^{1}H-NMR, UV–Vis spectroscopy and a microbial study. From the analytical and thermal data, the stoichiometry of the complexes was found to be 1:2 (metal:ligand). The molar conductance data revealed that all the metal chelates were non-electrolytes. The thermal stability of the complexes was studied by thermogravimetry and the decomposition schemes of the complexes are given. The ligands and their metal complexes were screened for antibacterial activity against *Staphylococcus aureus* and *Escherichia coli*, and fungicidal activity against *Aspergillus flavus*, *Curvularia lunata* and *Penicillium notatum*.

Keywords: dehydroacetic acid; chalcones; thermal study; ligand field parameters; antimicrobial study.

INTRODUCTION

A number of β-dicarbonyl compounds in which the carbonyl function(s) is bonded to C=C linkage(s) have gained considerable importance,[1] mainly because such compounds are associated with many biological activities due to the presence of the α,β-unsaturated system, as evidenced from their antimalarial,[2] antituberculosis,[3] antiplasmodial,[4] antitrichomonal,[5] anti-oxidant[6] and analgesic[7] activities, as well as their use as anti-inflammatory and cancer chemopreventive agents.[8]

Therefore, the synthesis and characterization of such unsaturated carbonyl system and their metal complexes are of tremendous importance. Continuing earlier research[9–11] on biologically active complexes of dehydroacetic acid chalcones containing β-dicarbonyl moieties and a carbonyl group directly linked to a C=C group, the present paper reports a synthetic, spectral, thermal and biological study.

* Corresponding author. E-mail: abr_chem@yahoo.co.in
doi: 10.2298/JSC0811073P

EXPERIMENTAL

Dehydroacetic acid was purchased from Merck and was used as supplied. *p*-Methoxybenzaldehyde and *p*-nitrobenzaldehyde, used for the preparation of the ligands, were from Aldrich. Metal chlorides used for the preparation of the complexes were from BDH. A.R. grade solvents were used for the spectral measurements. The carbon, hydrogen and sulphur content in each sample were determined using a Perkin Elmer 2400 CHNS analyzer. The IR spectra (nujol) were recorded on a Perkin Elmer C-75430 IR spectrometer in the range 4000–450 cm^{-1}. The ^{1}H-NMR spectra were recorded in $CDCl_3$ at room temperature using TMS as the internal standard on a Varian Mercury YH 300 MHz instrument. The metal contents were determined by AAS on a Perkin Elmer PE-Analyst 300. The TG–DTA measurements were performed on a Perkin ElmerTA/SDT-2960 instrument in a dry nitrogen atmosphere and at a heating rate of 10 °C min^{-1}. The electronic spectra were recorded in DMF solution on a Shimadzu UV-1601 spectrophotometer. The magnetic susceptibility measurements of the complexes were performed using a Gouy balance at room temperature with $Hg[Co(SCN)_4]$ as calibrant. The molar conductivity was measured on an Elico CM180 conductivity meter with a dip-type cell using a 1.0×10^{-3} M solution of complexes in DMF.

Synthesis of ligand

A solution of 0.010 mol of dehydroacetic acid, 10 drops of piperidine and 0.010 mol of aldehyde (*p*-methoxybenzaldehyde or *p*-nitrobenzaldehyde) in 25 ml chloroform was refluxed for 8–10 h. 10 ml of the chloroform–water azeotrope mixture was separated by distillation. Crystals of the product separated on slow evaporation of the remaining chloroform, which were recrystalised from ethyl acetate.

Synthesis of metal complexes

To a chloroform solution (30 ml) of the ligand (10 mmol), a methanolic solution (20 ml) of metal chloride (5.0 mmol) was added under constant stirring. The pH of the reaction mixture was maintained around 7–8 by adding a 10 % methanolic solution of ammonia. It was then refluxed for 2 h. The resulting metal complex was filtered hot and washed with chloroform, methanol and petroleum-ether and dried over calcium chloride in a desiccator.

Antimicrobial screening

The ligands and their metal complexes were screened for *in vitro* antibacterial activity against gram positive bacteria, *i.e*., S*taphylococcus aureus* and gram negative bacteria, *i.e*., *Escherichia coli* by the paper disc plate method.[12] The compounds were tested at a concentration of 0.50 mg ml^{-1} in DMF and compared with a known antibiotic, *viz.* ciproflaxin at the same concentration.

To evaluate the fungicidal activity of the ligands and the corresponding metal complexes, their effect on the growth of *Aspergillus flavus*, *Curvularia lunata* and *Penicillium notatum* was studied. The ligand and their corresponding metal chelates in DMF were screened *in vitro* by the disc diffusion method.[13] The ligands and complexes were dissolved separately in DMF to obtain concentration of 125 and 250 μg/disc. The linear growth of the fungus was recorded by measuring the diameter of colony after 96 h. The diameters of the zone of inhibition produced by the complexes were compared with griseofulvin antifungal drug.

RESULTS AND DISCUSSION

Elemental analyses show 1:2 (metal:ligand) stoichiometry for all the complexes (Fig. 1). The analytical data of the ligand and the complexes are given in

Table I. They correspond well with the general formula $[M(L^{1 \text{ or } 2})_2(H_2O)_2]$, where M = Mn(II), Co(II), Ni(II) and Cu(II), and $[M(L^{1 \text{ or } 2})_2(Cl)(H_2O)]$, where M = Fe(III), and $L^1 = C_{16}H_{14}O_5$ and $L^2 = C_{15}H_{11}NO_6$. The presence of coordinated water was confirmed by TGA–DTA analysis. The low conductance of the chelate solution supports the non-electrolytic nature of the metal complexes. Since a single crystal of the complexes could not be isolated from any common solvent, the possible structure was predicted based on analytical, spectroscopic, magnetic and thermal data.

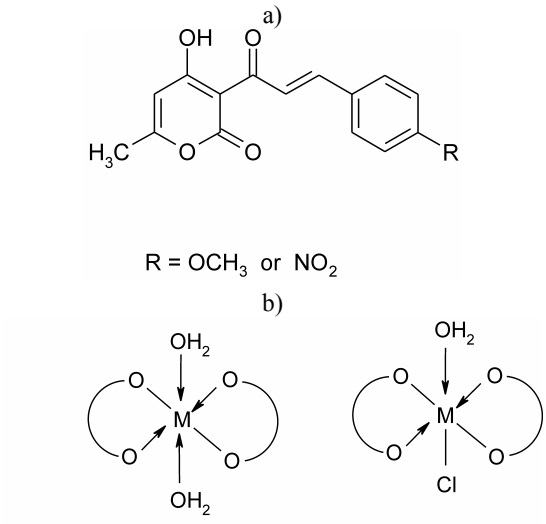

Fig. 1. The proposed structures of ligands (a) and complexes (b).

TABLE I. Physical characterization, analytical and molar conductance data of the compounds

Compound	M_r g mol^{-1}	M.p. °C	Yield %	Color	Found (Calcd.), %				Λ_m MΩ^{-1} cm^2 mol^{-1}
					M	C	H	N	
Ligand HL^1 $C_{16}H_{14}O_5$	286.3	208	52	Yellow	–	67.54 (67.13)	4.89 (4.93)	–	–
$[C_{32}H_{30}O_{12}Mn]$	661.5	272	59	Brown	8.11 (8.30)	57.92 (58.10)	4.32 (4.57)	–	12.7
$[C_{32}H_{28}O_{11}ClFe]$	679.91	268	68	Dark brown	8.20 (8.21)	56.12 (56.52)	4.00 (4.15)	–	13.3
$[C_{32}H_{30}O_{12}Co]$	665.5	>300	61	Light brown	8.71 (8.85)	57.31 (57.75)	4.44 (4.54)	–	15.1
$[C_{32}H_{30}O_{12}Ni]$	665.3	258	57	Pale green	8.80 (8.82)	57.07 (57.77)	4.65 (4.55)	–	13.7
$[C_{32}H_{30}O_{12}Cu]$	670.1	296	58	Green	9.32 (9.48)	58.01 (57.35)	4.44 (4.51)	–	17.5
Ligand HL^2 $C_{15}H_{11}NO_6$	301.3	246	54	Yellow	–	59.52 (59.80)	3.51 (3.68)	4.57 (4.65)	–

TABLE I. Continued

Compound	M_r g mol^{-1}	M.p. °C	Yield %	Color	Found (Calcd.), %				Λ_m MΩ^{-1} cm^2 mol^{-1}
					M	C	H	N	
$[C_{30}H_{24}N_2O_{14}Mn]$	691.5	>300	52	Brown	7.79 (7.94)	51.79 (52.10)	3.36 (3.49)	3.97 (4.05)	10.1
$[C_{30}H_{22}N_2O_{13}ClFe]$	709.7	>300	63	Red	7.91 (7.87)	51.22 (50.77)	3.22 (3.12)	3.87 (3.95)	13.1
$[C_{30}H_{24}N_2O_{14}Co]$	695.5	>300	61	Light brown	8.32 (8.47)	52.32 (51.81)	3.39 (3.48)	3.89 (4.03)	11.2
$[C_{30}H_{24}N_2O_{14}Ni]$	695.2	>300	57	Pale green	8.36 (8.44)	51.20 (51.82)	3.55 (3.48)	3.91 (4.03)	10.1
$[C_{30}H_{24}N_2O_{14}Cu]$	700.1	>300	63	Green	9.23 (9.07)	51.08 (51.46)	3.59 (3.45)	4.11 (4.00)	12.2

^{1}H-NMR spectroscopy

Ligand HL^1. ^{1}H-NMR (300 MHz, $CDCl_3$, δ / ppm): 2.27 (3H, *s*, C_6–CH_3), 3.85 (3H, *s*, –OCH_3), 5.93 (1H, *s*, C_5–H), 6.9–8.43 (6H, *m*, phenyl ring and –CH=CH–), 16.65 (1H, *s*, –OH).

Ligand HL^2. ^{1}H-NMR (300 MHz, $CDCl_3$, δ / ppm): 2.35 (3H, *s*, C_6–CH_3), 6.03 (1H, *s*, C_5–H), 6.9–8.3 (6H, *m*, phenyl ring and –CH=CH–), 16.77 (1H, *s*, –OH).

IR Spectroscopy

The IR spectra of the ligands show bands at 3164–3120, 1739–1720, 1705––1675 and 1257–1222 cm^{-1}, assignable to ν(OH) (phenolic hydrogen bonded), ν(C=O) (lactone carbonyl), ν(C=O) (acetyl carbonyl) and ν(C–O) (phenolic) stretching mode, respectively (Table II).[14,15] In the IR spectra of all the metal chelates, no band was observed in the region 3164–3120 cm^{-1}. Instead, in its place, a broad band characteristic of ν(OH) of coordination water was observed in the region 3500–3200 cm^{-1}.The presence of coordinated water was further confirmed by the appearance of a non-ligand band in the region 830–840 cm^{-1}, assignable to the rocking mode of water.[16] This was also established and supported by TG and DTA analysis. The absence of ν(OH) (phenolic) at 3164–3120 cm^{-1} suggests subsequent deprotonation of the phenolic group and coordination of the phenolic oxygen to the metal ion. This was supported by an upward shift in ν(C–O) (phenolic)[17] by 20–40 cm^{-1}. The ν(C=O) (acetyl carbonyl) was shifted to lower energy with respect to the free ligand, suggesting the participation of the acetyl carbonyl in the coordination.[14,15,17] The IR spectra of all the compounds showed a prominent band at ≈ 1377 and ≈ 970 cm^{-1}, typical of ν(C–O–C) and *trans*–CH=CH– absorption. The presence of new bands in the region 600–450 cm^{-1} can be assigned to ν(M–O) vibrations.[16]

Hence, the ligands coordinated with the metal ions as monodeprotonated bidentate and the coordination occurs *via* the acetyl and phenolic oxygen of dehydroacetic acid moiety, as shown in Fig. 1.

TABLE II. Magnetic and electronic spectral data of the complexes and their ligand field parameters

Complex	ν(OH) cm^{-1}	ν(C=O) (lactone carbonyl) cm^{-1}	ν(C=O) (acetyl carbonyl) cm^{-1}	ν(C–O) (phenolic) cm^{-1}	$\nu(NO_2)$ cm^{-1}	ν(M-O) cm^{-1}	μ_{eff} / μ_B	10 Dq cm^{-1}	B / cm^{-1}	β	ν_2/ν_1	LFSE kcal mol^{-1}
HL^1 $C_{16}H_{14}O_5$	3164(*b*)	1709(*m*)	1705(*m*)	1257(*m*)	–	–	–	–	–	–	–	–
HL^2 $C_{15}H_{11}NO_6$	3126(*b*)	1722(*s*)	1679(*m*)	1224(*m*)	1575(*m*)	–	–	–	–	–	–	–
$[Mn(L^1)_2(H_2O)_2]$	3375(*b*)	1740(*m*)	1634(*m*)	1253(*m*)	–	566(*m*)	5.77	–	–	–	–	–
$[Mn(L^2)_2(H_2O)_2]$	3373(*b*)	1719(*s*)	1645(*s*)	1254(*m*)	1574(*s*)	585(*m*) 533(*m*)	5.81	–	–	–	–	–
$[Fe(L^1)_2(Cl)(H_2O)]$	3379(*b*)	1723(*s*)	1620(*s*)	1279(*m*)	–	597(*m*) 537(*m*)	5.92	–	–	–	–	–
$[Fe(L^2)_2(Cl)(H_2O)]$	3375(*b*)	1719(*m*)	1647(*m*)	1250(*m*)	1573(*m*)	586(*m*) 533(*w*)	5.79	–	–	–	–	–
$[Co(L^1)_2(H_2O)_2]$	3348(*b*)	1698(*s*)	1625(*s*)	1297(*m*)	–	563(*m*) 549(*m*)	4.66	8779	821.1	0.84	1.91	25.08
$[Co(L^2)_2(H_2O)_2]$	3365(*b*)	1721(*s*)	1640(*m*)	1255(*m*)	1571(*s*)	555(*m*) 532(*w*)	4.70	9298	874.8	0.90	1.93	26.41
$[Ni(L^1)_2(H_2O)_2]$	3348(*b*)	1698(*m*)	1624(*m*)	1297(*m*)	–	562(*m*) 549(*m*)	3.03	9372	781.5	0.75	1.66	26.77
$[Ni(L^2)_2(H_2O)_2]$	3365(*b*)	1718(*m*)	1628(*m*)	1243(*m*)	1566(*m*)	580(*m*)	3.02	9910	701.0	0.67	1.55	28.31
$[Cu(L^1)_2(H_2O)_2]$	3363(*b*)	1729(*m*)	1620(*m*)	1299(*m*)	–	534(*m*)	2.09	15122	–	–	–	43.22
$[Cu(L^2)_2(H_2O)_2]$	3370(*b*)	1716(*m*)	1625(*m*)	1252(*m*)	1572(*m*)	598(*m*) 489(*w*)	1.95	15138	–	–	–	43.25

Magnetic and electronic absorption spectroscopy

The magnetic and electronic spectral data are given in Table II. The data is of relevance for the proposed structure of the complexes (Fig. 1). The electronic spectra of the Cu(II) complexes in DMF revealed one broad band at 15128 and 25126 cm^{-1} for ligand HL^1 and at 15138 and 25000 cm^{-1} for ligand HL^2, assignable to a $^2E_g \rightarrow {}^2T_{2g}$ transition and charge transfer, respectively. The observed magnetic moment value for the Cu(II) complexes was in the range 1.95–2.09 μ_B. The electronic spectral data[18] coupled with the magnetic moment value suggest a distorted octahedral geometry for the Cu(II) complexes.[19] The electronic spectra of Ni(II) complexes display three bands at 9372, 15625 and 24213 cm^{-1} for HL^1 and at 9910, 15360 and 24885 cm^{-1} for HL^2, assignable to $^3A_{2g} \rightarrow {}^3T_{2g}$ (F) (ν_1), $^3A_{2g} \rightarrow {}^3T_{1g}$ (F) (ν_2) and $^3A_{2g} \rightarrow {}^3T_{1g}$ (P) (ν_3) transitions, respectively. This is in accordance with earlier reported values for octahedral Ni(II) complexes.[21,22] The reductions of the Racah parameter (B) and the nephelauxetic effect (β) from the value of the free ion suggest an appreciable amount of covalent character in the metal ligand bonds.[20,21] The calculated values of 10 Dq, B, ν_2/ν_1 and β (Table II) lie in the range reported for octahedral geometry. The normal magnetic moment 2.99–3.19 μ_B confirms the proposed geometry. The Co(II) complexes show three transitions at 9569, 18348 and 22675 cm^{-1} for HL^1 and at 9900, 19182 and 23640 cm^{-1} for HL^2, assignable to $^4T_{1g}$ (F) $\rightarrow {}^4T_{2g}$ (F) (ν_1), $^4T_{1g}$ (F) $\rightarrow {}^4A_{2g}$ (F) (ν_2) and $^4T_{1g}$ (F) $\rightarrow {}^4T_{1g}$ (P) (ν_3) transitions, respectively.[19,20] The calculated values of 10 Dq, B, ν_2/ν_1 and β together with the magnetic moment value of the Co(II) complexes (Table II) suggest octahedral geometry. The obtained values of LFSE determine the stability of the complexes and follows the order in terms of metal ion Cu(II) > Ni(II) > Co(II) for ligand HL^1 and HL^2.

The Fe(III) complexes of ligands HL^1 and HL^2 show three bands at, respectively, 14556, 21692, 24450 cm^{-1} and 14484, 22322, 24196 cm^{-1}, assignable to $^6A_1 \rightarrow {}^4T_1$ (G), $^6A_1 \rightarrow {}^4T_2$ (G) and $^6A_1 \rightarrow {}^4E$ (G) transitions, respectively. The spectra suggest distorted octahedral geometry.[19,21,23] The electronic spectrum of Mn(II) complex of HL^1 displays weak bands at 17794, 19569 and 31056 cm^{-1}, whereas Mn(II) complex of HL^2 displayed weak bands at 18382 and 24671 cm^{-1}. These bands are both Laporte and spin-forbidden. However, due to instantaneous distortion of the octahedral structures around the metal cation, weak bands sometimes do appear.[19,21]

Thermal analysis

The Mn(II), Fe(III), Co(II), Ni(II) and Cu(II) complexes of ligand HL^1 were chosen for a thermal study. The TG curve of the complexes of ligand HL^1 shows three decomposition steps. On the TG curve of the Mn(II) complex, the first step shows a steep slope between 150–200 °C with a mass loss of 5.0 % (calculated 5.4 %), indicating the removal of two molecules of coordinated water. An endo-

thermic peak in the range 150–200 °C (Δt_{min} = 175 °C) on the DTA curve corresponds to the dehydration step. The anhydrous compound in second step decomposes within a short temperature range from 220–330 °C, with a 37.0 % mass loss (calculated 36.3 %). An exotherm between 240 and 400 °C with a Δt_{max} = = 270 °C on the DTA curve corresponds to this mass loss. This step may be attributed to the removal of the non-coordinated part of the ligand, *i.e.*, $[C_{16}H_{16}O_2]$. The third mass loss step in the range 400–790 °C corresponds to the decomposition of the coordinated part of the ligand, with a mass loss 47.0 % (calculated 47.6 %). A broad endotherm is observed for this step. The mass of the final residue corresponds to stable MnO, 11.0 % (calculated, 10.7 %).

In the thermal study of the Fe(III) complex, an inclined slope from 175–195 °C on the TG curve, with a mass loss of 7.0 % (calculated 7.9 %), indicates the removal of one molecule of water and one chloride ion. An endothermic peak in the range 180–240 °C was observed on the DTA curve (Δt_{min} = 192 °C). The complex continues to decompose in a second step between 210 and 300 °C, with 37.0 % mass loss (calculated 35.2 %). A corresponding exothermic peak between 250–280 °C (Δt_{max} = 265 °C) on the DTA is attributed to the removal of the non-coordinating part of the ligand. The third step corresponds to the decomposition of remaining part of the ligand with a mass loss 47.0 % (calculated 46.3 %). The mass of the final residue was 9.0 % (calculated 10.6 %), corresponding to FeO.

The thermal decomposition profile of the Co(II) complex showed no weight loss up to 140 °C. A mass loss of 5.0 % (calculated 5.4 %) was observed in the range 140–175 °C. The endothermic peak between 140–165 °C (Δt_{min} = 152 °C) correspond to the loss of two molecules of water. The second step of decomposition was between 265 and 400 °C with a 37.0 % mass loss (calculated 36.1 %). The broad exothermic peak between 270–375 °C (Δt_{max} = 346 °C) on the DTA curve is attributed to the removal of the non-coordinating part of the ligand. The mass loss continued with the slow decomposition of remaining part of the ligand 45.5 % (calculated 47.2 %). The mass of the final residue corresponded to CoO, 12.5 % (calculated 11.3 %).

The thermal decomposition profile of the Ni(II) complex showed a mass loss of 5.0 %(calculated 5.4 %) in the range 150–175 °C, indicating the removal of two coordinated water molecules. An endothermic peak on the DTA curve between 160–185 °C (Δt_{min} = 162 °C) also corresponds to dehydration. The second step of the decomposition was between 190 and 325 °C with a 37.0 % mass loss (calculated 36.1 %). A broad exothermic peak between 200–350 °C (Δt_{max} = 260 °C) on the DTA curve is attributed to the removal of the non-coordinating part of the ligand. The mass loss continued with the slow decomposition of the remaining part of the ligand up to 900 °C with a 46.0 % (calculated 47.3 %) mass loss. A broad endothermic peak between 450–850 °C was observed on the DTA curve. The mass of the final residue of 12.0 % (calculated 11.2 %) corresponds to NiO.

On the TG curve of the Cu(II) complex, the mass loss commences at 120 °C with an inclined slope from 155–185 °C with a mass loss of 6.0 % (calculated 5.4 %), indicating the removal of two molecules of coordinated water. An endothermic peak in the range 150–200 °C (Δt_{min} = 158 °C) on the DTA curve also corresponds to the dehydration. The second step of the decomposition continues on the TG curve from 275 up to 375 °C, with a mass loss of 37.0 % (calculated 35.7 %) and the exothermic peak (Δt_{max} = 299 °C) on the DTA curve may be attributed to the removal of the non-coordinated part of the ligand. The third step in the range 420–880 °C with a mass loss of 46.0 % (calculated 47.0 %) corresponds to the decomposition of the coordinated part of the ligand. A broad endotherm was also observed for this step. The mass of the final residue corresponded to stable CuO, 11.0 % (calculated 11.9 %).

Antimicrobial activity

The results of the antimicrobial study, Table III, showed that the ligand HL^1 had no antibacterial activity whereas the ligand HL^2 exhibited weak activity. This may be due to the presence of the electron withdrawing group ($-NO_2$) on the phenyl ring. The Cu(II) and Co(II) complexes of ligand HL^2 showed moderate antibacterial activity against both of the bacteria.

TABLE III. Antibacterial and antifungal activities of ligands and their metal complexes

Compound	Antibacterial activity		Antifungal activity					
	Inhibition zone of bacterial growth, mm		*A. flavus*		*C. lunata*		*P. notatum*	
	S. aureus 0.50 mg ml^{-1}	*E. coli* 0.50 mg ml^{-1}	I[a]	II[b]	I	II	I	II
HL^1 $C_{16}H_{14}O_5$	1.1	1.2	7	15	7	14	7	14
HL^2 $C_{15}H_{11}NO_6$	3.6	4.1	8	16	8	15	8	15
$[Mn(L^1)_2(H_2O)_2]$	1.6	1.8	9	17	8	17	8	17
$[Mn(L^2)_2(H_2O)_2]$	4.2	4.5	11	24	11	22	10	22
$[Fe(L^1)_2(Cl)(H_2O)]$	2.1	2.1	8	16	7	19	7	15
$[Fe(L^2)_2(Cl)(H_2O)]$	4.5	4.9	9	20	9	19	9	20
$[Co(L^1)_2(H_2O)_2]$	5.1	5.6	10	20	10	20	10	20
$[Co(L^2)_2(H_2O)_2]$	8.9	9.3	14	33	13	32	13	33
$[Ni(L^1)_2(H_2O)_2]$	4.2	4.6	9	19	9	19	9	19
$[Ni(L^2)_2(H_2O)_2]$	6.3	6.8	13	30	12	29	12	30
$[Cu(L^1)_2(H_2O)_2]$	6.1	6.5	11	22	11	21	11	19
$[Cu(L^2)_2(H_2O)_2]$	9.2	10.7	15	37	14	34	14	36
Ciproflaxin	12.0	13.5	–	–	–	–	–	–
Griseofulvin	–	–	31	34	29	33	30	34

[a]125 μg/disc; [b]250 μg/disc

From the results in Table III, it can be concluded that the ligands and their metal complexes show significant antifungal activity at a concentration of 250 μg

disc^{-1} against all the tested fungi. In addition, the activity decreased as the concentration decreased. The Cu(II)HL^2 complex exhibited a higher antifungal activity than the standard at a concentration of 250 μg disc^{-1}, while the Ni(II) and Co(II) complexes of HL^2 showed nearly same antifungal activity as the standard. The order of inhibition with respect to metal ions of HL^1 and HL^2 is Cu > Co > > Ni > Mn > Fe. It was found that these complexes show strong antifungal activity at lower concentration when compared to earlier reported literature.[17,24]

It was observed that the metal complexes show enhanced antimicrobial activity as compared to the ligands. The increased activity of the chelates can be explained on the basis of the overtone concept and the Tweedy chelation theory.[25] According to the overtone concept of cell permeability, the lipid membrane that surrounds the cell favours the passage of only lipid-soluble materials, for which reason liposolubility is an important factor controlling antimicrobial activity. On chelation, the polarity of metal ion is reduced to a greater extent due to overlap of the ligand orbital and partial sharing of its positive charge with the donor groups and also due to delocalization of the π-electrons over whole chelate ring, which enhances the penetration of the complexes into the lipid membranes and the blocking of the metal binding sites of the enzymes of the micro-organisms.

CONCLUSIONS

In the light of the above discussion, a distorted octahedral geometry for Cu(II), Mn(II) and Fe(III) complexes and an octahedral geometry for the Co(II) and Ni(II) complexes are proposed. The ligands behave as bidentate, coordinating through the phenolic oxygen and the acetyl carbonyl group of the dehydroacetic acid moiety. The complexes are biologically active and exhibit enhanced antifungal activities compared to their parent ligands. The Cu(II), Ni(II) and Co(II) complexes of ligand HL^2 show good antifungal activity, hence further study of these complexes in agriculture could lead to interesting results.

Acknowledgements. V. N. P. is grateful to the UGC (WRO) Pune, for the award of a Teacher fellowship under FIP in Xth plan. The authors are also thankful to Dr. T. K. Chondekar, Dept of Chemistry, Dr. B. A. M. University, Aurangabad, for valuable suggestions.

ИЗВОД

ПРЕЛАЗНИ МЕТАЛНИ КОМПЛЕКСИ СА КИСЕОНИЧНИМ ДОНОРНИМ ЛИГАНДИМА: СИНТЕЗА И ТЕРМИЧКА, СПЕКТРАЛНА И АНТИМИКРОБНА ПРОУЧАВАЊА

VAIBHAV N. PATANGE[1], RAJENDRA K. PARDESHI[1] и BALASAHEB R. ARBAD[2]

[1]Department of Chemistry, Shri Chhatrapati Shivaji College, Omerga, Dist-Osmanabad – 413606, Maharashtra и [2]Department of Chemistry, Dr. Babasaheb Ambedkar Marathwada University, Aurangabad – 431004, Maharashtra, India

Добијени су прелазни метални комплекси халкона изведених кондезацијом 3-ацетил-6-метил-2*H*-пиран-2,4(3*H*)-диона (дехидросирћетне киселине) и *p*-метоксибензалдехида (HL^1) или *p*-нитробензалдехида (HL^2) и окарактерисани елементалном анализом, кондуктометријом,

термичком анализом, магнетним, IR, ^{1}H-NMR, UV–Vis и проучавањем микробне активности. Из аналитичких и термичких података нађена је стехиометрија 1:2 (метал:лиганд). Подаци за моларну проводљивост потврдили су да су ови метални хелати неелектролити. Термичка стабилност комплекса проучавана је термогравиметријом и дате су схеме распада комплекса. Лиганди и њихови комплекси метала су тестирани на антибактеријску активност према *Staphylococcus aureus* и *Escherichia coli* и антигљивичну активност према *Aspergillus flavus*, *Curvularia lunata* и *Penicillium notatum*.

(Примљено 14. новембра 2007, ревидирано 6. јуна 2008)

REFERENCES

1. K. Krishanankutty, V. D. John, *Synth. React. Inorg. Metal Org. Chem.* **28** (2003) 343
2. S. S. Lim, H. S. Kim, D. U. Lee, *Bull. Korean Chem. Soc.* **28** (2007) 2495
3. M. S. Ponnurengam, S. Malliappan, K. G. Sethu, M. Doble, *Chem. Pharm. Bull.* **55** (2007) 44
4. M. L. Go, M. Liu, P. Wilairat, P. J. Rosenthal, K. L. Saliba, K. Kirk, *Antimicrob. Agents Chemother.* **48** (2004) 3241
5. A. O. Oyedapo, V. O. Makanju, C. O. Adewunmi, E. O. Iwalewa, K. Adenowo, *Afr. J. Trad. CAM* **1** (2004) 55
6. C. L. Miranda, J, F. Stevens, V. Ivanov, M. McCall, B. Frei, M. L. Deinzer, D R. Buhler, *J. Agricult. Food Chem.* **48** (2000) 3876
7. G. S. B. Viana, M. A. M. Bandeira, F. J. A. Matos, *Phytomedicine* **10** (2003) 189
8. S. J. Won, C. T. Liu, L. T. Tsao, J. R. Weng, H. H. Ko, J. P. Wang, C. N. Lin, *Eur. J. Med. Chem.* **40** (2005) 103
9. V. N. Patange, B. R. Arbad, V. G. Mane, S. D. Salunke, *Transition Met. Chem.* **32** (2007) 944
10. V. N. Patange, B. R. Arbad, *Indian J. Chem. Soc.* **84** (2007) 1096
11. V. G. Mane, V. N. Patange, B. R. Arbad, *Indian J. Chem. Soc.* **84** (2007) 1086
12. H. H. Thornberry, *Phytopathology* **40** (1950) 419
13. A. W. Bauer, W. M. M. Kirby, J. C. Shesies, M. Turck, *Am. J. Clin. Pathol.* **44** (1966) 93
14. N. Ramarao, V. P. Rao, V. J. Tyaga Raju, M. C. Ganorkar, *Indian. J. Chem. A* **24** (1985) 877
15. O. Carugo, C. B. Castellani, M. Rizzi, *Polyhedron* **9** (1990) 2061
16. K. Nakamoto, *Infrared Spectra of Inorganic and Coordination Compounds*, Wiley, New York, 1970, pp. 159, 167, 214
17. P. V. Rao, A. V. Narasaiah, *Indian. J. Chem. A* **42** (2003) 1896
18. G. L. Eichhorn, J. C. Bailar, *J. Am. Chem. Soc.* **75** (1953) 2905
19. B. N. Figgis, *Introduction to Ligand Fields*, Interscience, London, 1966
20. K. B. Gudasi, S. A. Patil, R. S. Vadavi, R. V. Shenoy, M. S. Patil, *J. Serb. Chem. Soc.* **71** (2006) 529
21. A. B. P. Lever, *Inorganic Electronic Spectroscopy,* Elsevier, Amsterdam, 1968
22. K. C. Satpatty, A. K. Panda, R. Mishra, I. Pande, *Transition Met. Chem.* **16** (1991) 410
23. R. N. Prasad, M. Mathur, *J. Serb. Chem. Soc.* **67** (2002) 825
24. P. S. Mane, S. G. Shirodkar, B. R. Arbad, T. K. Chondekar, *Indian. J. Chem. A* **40** (2001) 648
25. N. Raman, A. Kulandaisamy, C. Tungaraja, P. Manishankar, S. Viswanthan, C. Vedhi, *Transition Met. Chem.* **29** (2004) 129.

www.shd.org.rs

Journal of the Serbian Chemical Society

JSCS@tmf.bg.ac.yu • www.shd.org.rs/JSCS

J. Serb. Chem. Soc. 73 (11) 1083–1112 (2008)
JSCS–3789

UDC 544.4/.6.004.2+66.022.362:546.82+
621.3.032.2:544.773.42
Authors' review

AUTHORS' REVIEW

Electrocatalytic properties and stability of titanium anodes activated by the inorganic sol–gel procedure

VLADIMIR V. PANIĆ[1]*# and BRANISLAV Ž. NIKOLIĆ[2]#

[1]*ICTM – Centre for Electrochemistry, Njegoševa 12, 11000 Belgrade and* [2]*Faculty of Technology and Metallurgy, Karnegijeva 4, 11000 Belgrade, Serbia*

(Received 3 March, revised 2 September 2008)

Abstract: The properties of activated titanium anodes, RuO_2–TiO_2/Ti and RuO_2–TiO_2–IrO_2/Ti, prepared from oxide sols by the sol–gel procedure, are reviewed. RuO_2 and TiO_2 sols were synthesized by forced hydrolysis of the corresponding chlorides in acid medium. The morphology of the prepared sols was investigated by transmission electron microscopy. The chemical composition of the RuO_2 sol was determined by X-ray diffraction and thermogravimetric analysis. The loss of electrocatalytic activity of a RuO_2–TiO_2/Ti anode during an accelerated stability test was investigated by examination of the changes in the electrochemical characteristics in the potential region of the chlorine and oxygen evolution reaction, as well as on the open circuit potential. These electrochemical characteristics were investigated by cyclic voltammetry, electrochemical impedance spectroscopy and polarization measurements. The changes in electrochemical characteristics of the anode prepared by the sol–gel procedure were compared to the changes registered for an anode prepared by the traditional thermal decomposition of metal chlorides. The comparison indicated that the main cause for the activity loss of the sol–gel prepared anode was the electrochemical dissolution of RuO_2, while in the case of thermally prepared anode the loss was mainly caused by the formation of an insulating TiO_2 layer in the coating/Ti substrate interphase. The results of an accelerated stability test on RuO_2–TiO_2/Ti and RuO_2–TiO_2–IrO_2/Ti anodes showed that the ternary coating is considerably more stable than the binary one, which is the consequence of the greater stability of IrO_2 in comparison to RuO_2.

Keywords: activated titanium anodes; oxide sols; coating morphology; electrocatalytic properties; anode stability.

CONTENTS

* Corresponding author. E-mail: panic@ihtm.bg.ac.yu
# Serbian Chemical Society member.

doi: 10.2298/JSC0811083P

1. INTRODUCTION

Electrocatalytic materials based on noble metal oxides of metallic conductivity are widely used as electrodes in many fields of applied electrochemistry, such as chlorine production in the chlor-alkali and chlorate industry, processes involving oxygen generation in electroplating and metal electrowinning, as well as in cathodic protection, *etc*.[1] Most recently, these materials have been the subject of investigations in the field of supercapacitors[2–4] and fuel cells,[5,6] due to their excellent capacitive properties. Depending on the application of interest, these oxide materials are usually composed of a mixture of a noble metal oxide, such as RuO_2 or IrO_2, and an electrochemically inert, non-conductive or semi-conductive oxide (TiO_2, ZrO_2, Ta_2O_5 or Co_3O_4),[1,7–9] which stabilizes the coating and enhances the catalytic properties of the material. In the chlor-alkali industry, titanium supported RuO_2–TiO_2 coatings, known as Dimensionally Stable Anodes or Activated Titanium Anodes (ATA), are used.

In long-term electrolysis of chloride solutions a very important feature of an ATA is its service life. The anode service life and coating stability can be evaluated by an accelerated stability test (AST),[8,10] which involves the electrolysis of a dilute chloride solution at a constant high current density. The end of an anode service life, *i.e.* the loss of electrocatalytic activity, is recognized as a sudden increase in the potential. This increase in potential could be caused by 1) the growth of an insulating TiO_2 layer in the substrate/coating interface, originating from substrate corrosion, and 2) anodic dissolution of the catalytically active oxide species, RuO_2, which enriches the coating surface with TiO_2. Coating erosion can also be involved in the deactivation process.[10] The coating morphology appears to play an important role in the consideration of the cause of anode deactivation.

The anode activity for the oxygen evolution reaction, however, appears to be a key factor in the process of anode degradation.[10–13] It is known that ATA

containing iridium oxide is more stable in the electrolysis of NaCl solutions than binary RuO_2–TiO_2 coating.[12,14–16] This is due to the slower corrosion rate of IrO_2 with respect to RuO_2, since a considerable portion of the current is related to the oxygen evolution reaction.[17] For this reason, activated titanium anodes, commercially available as oxygen-evolving anodes and for cathodic protection purposes, contain iridium oxide in small amounts, in addition to ruthenium and titanium oxide.

Boodts and coworkers[8,9,18] showed that electrochemical impedance spectroscopy (EIS) provides useful information about the ATA deactivation pathway. In the case of Ti/RuO_2(x)+Co_3O_4(1–x) anodes, these authors reported the formation of a TiO_2 layer in the coating/substrate interphase as the main cause for the deactivation of anodes with low RuO_2 contents, due to high coating porosity. Anodes with a high RuO_2 content are of lower porosity, which is recognized as the cause for activity loss *via* intensive dissolution of the Ru species from the coating surface.[9]

The usual preparation method for RuO_2–TiO_2 coatings involves the process of thermal decomposition of a metal chloride mixture from organic solvents.[1,10] However, in recent years, coating preparation by the sol–gel procedure has occupied the attention of scientific workers. This is due to the possibility of preparing particles of more regular shape, size and distribution in the oxide coating.

The aim of this paper is to summarize the results of an investigation of the conditions of preparation of oxide sols and coatings on the morphology and electrochemical properties of RuO_2–TiO_2/Ti and RuO_2–TiO_2–IrO_2/Ti anodes prepared by the sol–gel procedure, especially from the standpoint of anode stability in electrolysis. The oxide sols were obtained by forced hydrolysis of an acid solution of metal chlorides at the boiling temperature. Some unique features of ATA prepared from sols obtained by the hydrolysis of alkoxides was also investtigated,[19–21] but this is not the subject of this review.

2. PHYSICO–CHEMICAL PROPERTIES OF OXIDE SOLS

The electrochemical properties of an ATA follow the basic characteristics of the oxide coating, which are influenced not only by the conditions during coating deposition (application technique and its repetition, thermal regime, coating thickness, *etc*.), but also by the physico–chemical properties of the oxide precursors. In the sol–gel procedure for coating preparation, the oxides are prepared prior to coating formation, which is the main difference with respect to thermal decomposition, when the oxides are formed *in situ* on a Ti substrate. Hence, the properties of oxide sols are reflected in the coating characteristics and, consequently, in the electrochemical properties of the ATA. The basic properties of the synthesized oxide sols and their mixture prepared for coating deposition are given in this Section, with a more detailed analysis of the ruthenium oxide sol, since this oxide is the electrocatalytically active component of the coating.

2.1. Ruthenium oxide sol

In order to check the degree of conversion in the preparation of the ruthenium oxide sol, the composition of the dry residue of the prepared sol was analyzed by energy depressive X-ray fluorescence spectroscopy (EDXRFS) and X-ray diffraction (XRD).[22] The EDXRFS spectrum is shown in Fig. 1. In addition to the high-intensity peak of ruthenium, a chlorine peak of low intensity was Registered. The appearance of the chlorine peak in the EDXRFS spectrum indicates that not all of the starting quantity of chloride precursor was converted into oxide. The XRD patterns of the dry residue of the RuO_xH_y sol, calcined at 130 °C, are shown in Fig. 2. The pattern designated as "A" was obtained for the dry residue, while "B" represents the XRD pattern of the dry residue redissolved in ethanol and dried at ambient temperature. The peaks in pattern "A" can be ascribed to crystalline ruthenium chloride, which indicates, as does the EDXRFS spectrum (Fig. 1), the incomplete conversion of the precursor. Pattern "B" in Fig. 2 indicates an amorphous structure, showing not only that ruthenium chloride does not crystallize from an ethanolic solution, but also that there is no other crystalline phase in the dry residue of the sol.

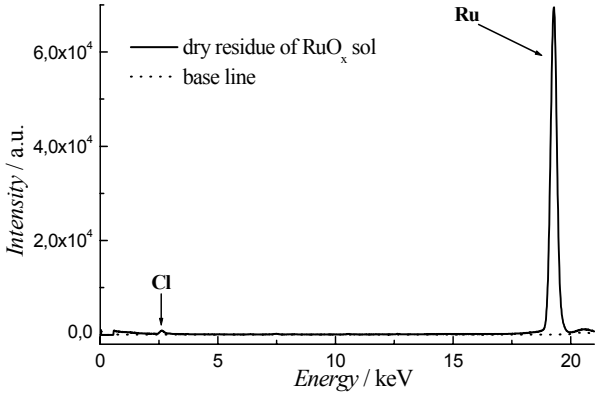

Fig. 1. EDXRFS spectrum of the solid phase of RuO_xH_y sol (Reprinted with permission of Elsevier).[22]

The forced hydrolysis process for the preparation of the sol is the time-dependent conversion of the precursor, in which some induction time for nuclei formation is necessary. For the duration of the process (ageing time), the primary nuclei grow to form the particles of the solid phase of the sol. It was shown[23,24] that the sol oxide particles grow with ageing time, which consequently influenced the electrochemical behavior of the sol–gel obtained oxide material. It was only a matter of time before all the precursor would be converted to the oxide. Bearing in mind the Ru to Cl peak intensity ratio from Fig. 1, a conversion above 95 % was achieved during the ageing time of the investigated sol, while Fig. 2 demonstrates that the formed oxide phase was amorphous.

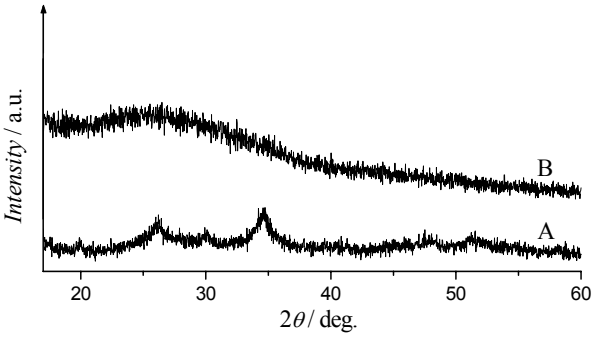

Fig. 2. XRD patterns of the solid phase of RuO_xH_y sol (A) and of RuO_xH_y sol solid phase redisolved in ethanol (B) (Reprinted with permission of Elsevier).[22]

The main feature of ruthenium oxide that defines its electrochemical properties is an optimal balance between protonic and electronic conductivity. The former increases with the water content in the hydrous oxide (RuO_xH_y), while the latter is a function of the oxide crystallinity.[22,25] Since the solid phase of the prepared sol was amorphous (Fig. 2), it should be subjected to thermal treatment in order to increase its electronic conductivity. However, the water content decreases with temperature and, consequently, so does the ability of the oxide to exchange protons with the solution. The processes that may occur during thermal treatment of the solid phase of the RuO_xH_y sol are indicated by the thermogravimetric (TG) and differential thermogravimetric (DTG) curve, which are shown in Fig. 3. The sample lost 30 % of its initial mass when the temperature was increased to around 120 °C. On the DTG curve, two minima (a and b) can be seen, indicating two processes of the release of weakly bonded water during the reversible sol–gel transition. The release of water from the hydrous oxide commences around 150 °C, and near 10 mass % was lost during a slow process accomplished around 350 °C (plateau c). In this step, one water molecule from $RuO_2{\cdot}2H_2O$ is released.[4,26] The remaining water molecule (from the monohydrate) is released at 430 °C (point d, Fig. 3), which contributes an additional 8 % mass loss. The interval d–e appears to be related to the conversion of residual chloride to oxide, since the presence chloride was registered by EDXRFS measurements (Fig. 1).

It follows from the TG measurements that the dispersed oxide retains an anhydrous nature over a wide temperature range, while the crystalline oxide structure was fully developed at the end of the processes related to the release of crystalline water, as is illustrated by the XRD pattern given in Fig. 4. These characteristics fully recommend the oxide prepared by the sol–gel process as a good protonic and electronic conductor.

Transmission electron microscopy (TEM) investigations[27] showed that the amorphous solid phase of the prepared sols consisted of spherical particles which are gathered in agglomerates. TEM images of such agglomerates are shown in Fig. 5 for sols of different ageing times. The sol with the shorter ageing time (Fig. 5a) consisted of spherical particles with a diameter of about 10 nm, while agglo-

merates with a more crystal-like structure, consisting of larger, irregularly shaped particles, were obtained at a longer ageing time (Fig. 5b).

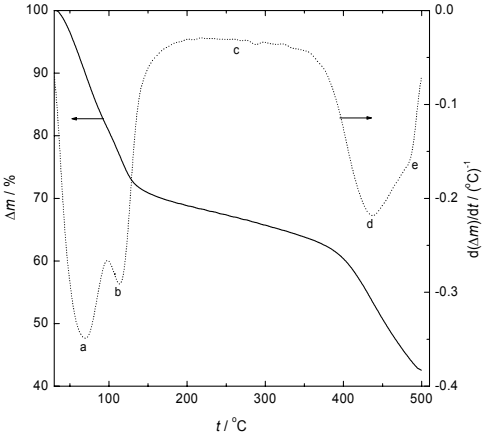

Fig. 3. TG and DTG curve registered for the solid phase of the RuO_xH_y sol.

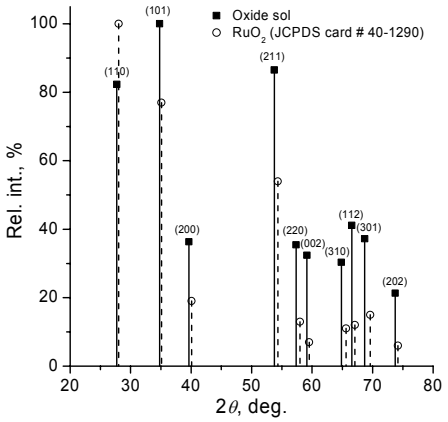

Fig. 4. XRD pattern of the solid phase of the RuO_xH_y sol annealed at 450 °C.

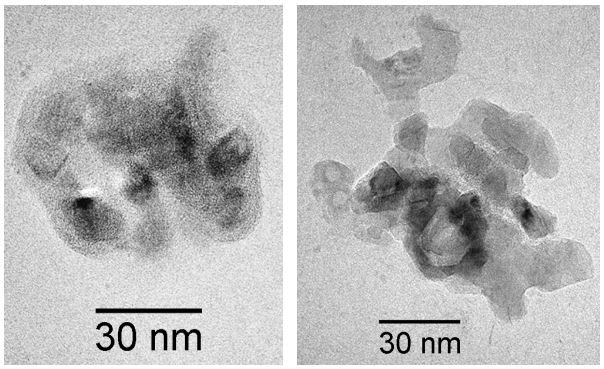

(a) (b)

Fig. 5. TEM Images of the solid phase of RuO_xH_y sol aged for 46 (a) and 94 h (b) (Reprinted with permission of Elsevier).[27]

2.2. Titanium oxide sol and sol mixture

Similar to the case of the ruthenium oxide sol, the solid phase of the prepared TiO_2 sol had an amorphous structure,[28] as it is illustrated by the XRD pattern shown in Fig. 6a, while the anatase crystal structure developed with increasing annealing temperature. In addition, the diffraction peaks become sharper with increasing temperature, which indicates an increase in the particle size.

However, in solid phase of RuO_2–TiO_2 sol mixture annealed at 450 °C, the particles of both oxides have a rutile structure, which is a usual characteristic of a thermally treated solid mixture of these oxides, regardless of the preparation procedure.[29–31]

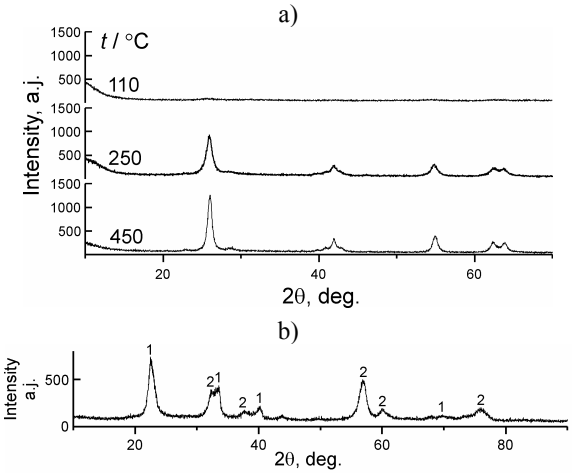

Fig. 6. XRD patterns of the solid phase of TiO_2 sol annealed at different temperatures (a) and RuO_2–TiO_2 sol mixture (b).

TEM images of differently aged TiO_2 sols are given in Fig. 7. Narrow-sized, small spherical crystallites with a diameter not larger than 5 nm form star-like agglomerates in the sol aged for the shorter time (Fig. 7a). However, with increasing ageing time, single sphere-shaped particles of a diameter around 25 nm are formed (Fig. 7b). Other authors also reported the particle size of colloidal TiO_2 in the order of nanometers.[32]

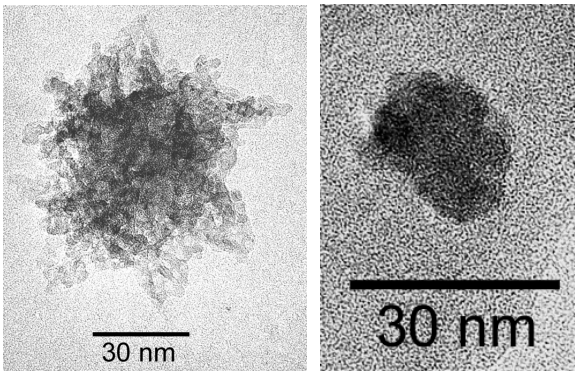

Fig. 7. TEM Images of the solid phase of TiO_2 sol aged for 15 (a) and 23 h (b) (Reprinted with permission of Elsevier).[27]

3. THE STRUCTURE AND MORPHOLOGY OF RuO_2–TiO_2 COATING

The scanning electron (SEM) microphotographs in Fig. 8 illustrate the typical appearance of the RuO_2–TiO_2 coatings prepared on titanium by the sol–gel procedure (Fig. 8a) and by *in situ* thermal decomposition of metal chlorides (Fig. 8b).[28] At the applied magnification, the sol–gel coating appears more cracked. The surface of the coatings looks like "cracked-mud" and consisted of "islands" (surface area ≈ 60 μm^2) separated by cracks, which are wider on sol–gel coating surface. The appearance of cracks also suggests that the islands in the sol–gel coating are made of distinct layers, while "thermal" coating appears smoother.

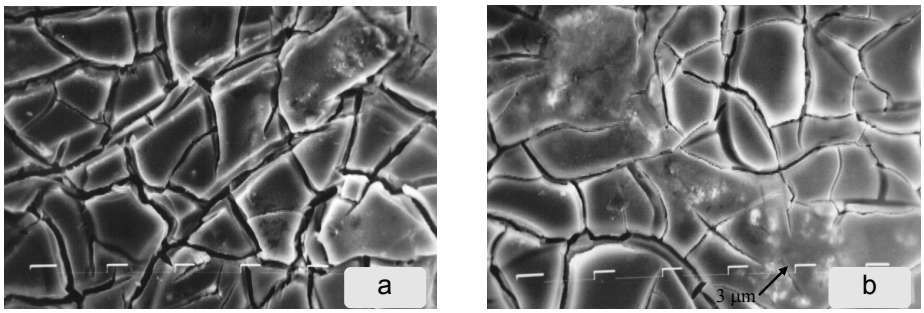

Fig. 8. Typical SEM microphotographs of RuO_2–TiO_2 coatings obtained by: a) the sol–gel procedure and b) thermal decomposition (Reprinted with permission of Elsevier).[28]

The essential difference in morphology between the sol–gel processed and thermally prepared RuO_2–TiO_2 coating is registered on the nano-scale.[27,28] The typical surface appearance on the nano-scale of the coatings prepared by the sol–gel procedure and thermal decomposition is given by the scanning tunneling microscopy (STM) 3D surface nanophotographs (scan size: 50 nm×50 nm) given in Fig. 9.

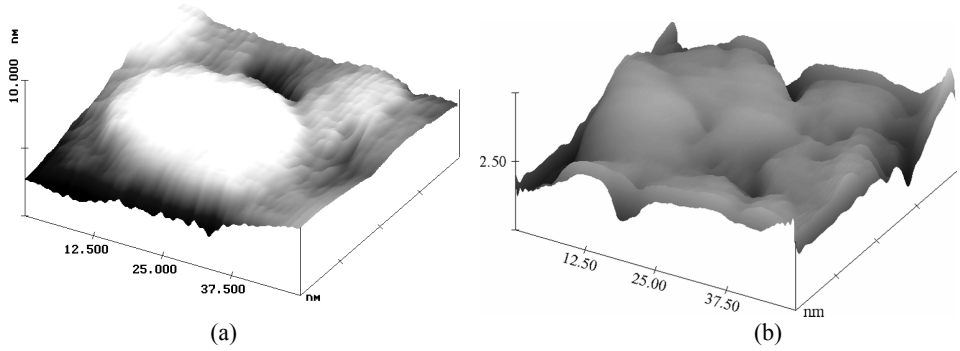

(a) (b)

Fig. 9. Typical STM microphotographs of the RuO_2–TiO_2 coatings obtained by: a) the sol–gel procedure and b) thermal decomposition (Reprinted with permission of Elsevier).[27,28]

It can be seen that the nano-roughness is more pronounced for the surface of sol–gel prepared coating (Fig. 9a). The average difference between real and geometric surface area, according to the STM data, was found to be two-fold greater for the sol–gel coating. The sharp nano-spots, which are ubiquitous on the surface of sol–gel coating, cannot be seen on the thermal one. It could be assumed that these surface characteristics are the result of the more defined oxide particles formed in the case of the sol–gel coating. The size of the spots is very similar to the RuO_2 particle size registered by TEM (Fig. 5a). Another important difference is the appearance of bright areas on the sol–gel coating, having a size of about 30 nm (Fig. 9a). Taking into account the size of the TiO_2 particles observed in the TEM image of the TiO_2 sol (Fig. 7b), being close to 25 nm, the conclusion appears to be that the bright areas in Fig. 9a are the large grains of TiO_2. It seems that small

the RuO_2 particles are on the top of and around each TiO_2 grain in the sol–gel prepared coating.[27]

4. CAPACITIVE ABILITY OF ACTIVATED TITANIUM ANODES AS THE FUNCTION OF THE PROPERTIES OF OXIDE SOLS

The pronounced capacitive ability of noble metal oxides is the consequence of pseudocapacitive behavior due to solid-state surface redox transitions of the metal ions, which is closely related to the oxide protonic conductivity.[1,2,33] Generally, proton-assisted redox transitions are written as follows:[33]

$$RuO_x(OH)_y + \delta H^+ + \delta e^- \rightarrow RuO_{x-\delta}(OH)_{y+\delta}, \quad 0 \leq \delta \leq x \qquad (1)$$

The transition reactions can be diffusion-controlled to different degrees by the proton injection/ejection process, depending on the coating porosity. On the other hand, the capacitance depends on the surface area. These features are directly influenced by the coating morphology, preparation procedure and oxide particle size,[19,20,23,27,34] which results in the capacitance being dependent on the rate of the charging/discharging process.

4.1. Preparation procedure, coating composition and capacitive response

The cyclic voltammograms (CV) of a sol–gel and a thermally prepared ATA recorded in acid solution are shown in Fig. 10. The registered CV shape is usual for RuO_2-based electrodes,[2,23,33] with a broad peak in the potential region from 0.20 to 0.50 V, which is related to the redox transition presented by Eq. (1). The voltammetric current densities recorded for the sol–gel prepared anode are larger than those recorded for thermally prepared one. This indicates the larger electrochemically active surface area[7] of the sol–gel prepared anode, due to the larger real surface area and greater RuO_2 content in the surface layer of the sol–gel prepared coating.[31] Using the approach of Da Silva *et al*.[35] for the values of the morphology factor, 0.50 and 0.52 are obtained for sol–gel and thermally prepared coating, respectively. These similar values indicate the similar contribution of inner coating surfaces to the overall coating capacitance, due to similar porosity of the coatings.[36]

The addition of a small amount of iridium oxide (10 mol %), either as *in situ* converted chloride or as previously prepared sol, into the sol–gel prepared RuO_2–TiO_2 coating results in an increase in the capacitive ability.[37] The voltammograms of ternary and binary coating registered in acid solution are shown in Fig. 11. The increase in the voltammetric currents were more pronounced at potentials positive to 0.40 V due to the imposed contribution of redox transitions of iridium species. If IrO_2 was applied from the sol, the effects were more pronounced.

4.2. The voltammetric charge and properties of the oxide sols

The dependence of coating capacitive ability on the ageing time, t_{ag}, (*i.e.* oxide particle size, Section 2) of the oxide sols was analyzed through the values of voltammetric charges.[23]

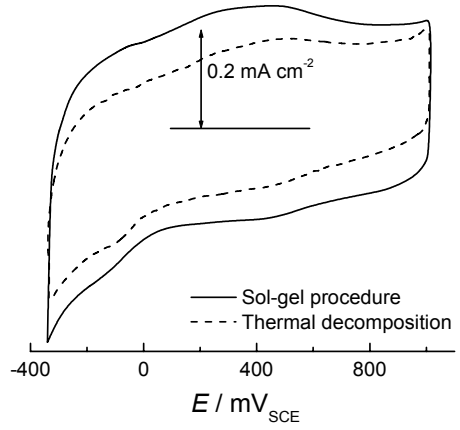

Fig. 10. Cyclic voltammograms of the RuO_2–$–TiO_2$/Ti electrodes prepared by the sol–gel and thermal procedure. Scan rate: 20 mV s^{-1}. Electrolyte: 1.0 mol dm^{-3} $HClO_4$.

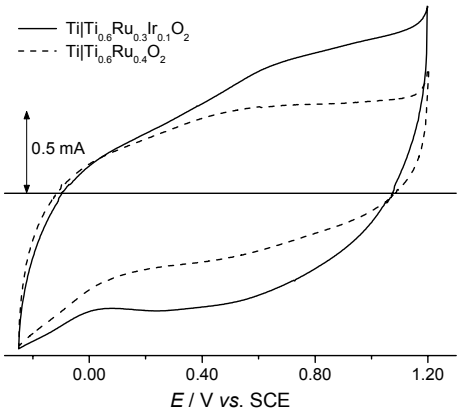

Fig. 11. Cyclic voltammograms of the RuO_2–$–TiO_2$–IrO_2/Ti and RuO_2–TiO_2/Ti electrodes prepared by the sol–gel procedure. Scan rate: 20 mV s^{-1}. Electrolyte: 1.0 mol dm^{-3} H_2SO_4.

The total charge, q^*_{tot}, related to the whole electrochemical surface area of the coating, could be separated into two components: the first, q^*_{out}, related to the "outer" parts of the coating, which are directly exposed to the electrolyte, and the second, q^*_{in}, related to the "inner" parts of the coating, which are hidden in loose grain boundaries, pores and cracks. The total charge, as well as its components, can be evaluated from the dependencies:

$$q^*(v) = q^*_{out} + kv^{-1/2} \quad (2)$$

$$q^*(v)^{-1} = (q^*_{tot})^{-1} + k'v^{1/2} \quad (3)$$

and

$$q^*_{tot} = q^*_{in} + q^*_{out} \quad (4)$$

where q^* is the charge obtained by integration of anodic part of the voltammetric curve at a given sweep rate v; k and k' are constants.

The values of the voltammetric charges obtained using Eqs. (2)–(4) as functions of the aging time of the RuO_2 and TiO_2 sol are shown in Fig. 12. For ageing times of the RuO_2 sol shorter than about 40 h, all three kinds of charge increase with increasing ageing time (Fig. 12a). After 40 h of ageing, the charges decrease with ageing time. Since these changes are seen for all three kinds of charge, it could be concluded that the particles from the RuO_2 sols of different ageing result in similar morphological changes in the outer surface of the coating as well as in its inner parts. The largest charge related to an anode obtained with a RuO_2 sol aged for about 40 h suggests that the solid phase of this sol had the largest ratio of small RuO_2 particles.[38] Smaller charge values related to anodes obtained with RuO_2 sols aged for times shorter than 40 h indicate that the particles of these sols were larger than those from the sol aged for about 40 h. Taking into account the fact that complete sol particle formation in the forced hydrolysis procedure requires some critical time,[39] it is to be expected that the formation of the RuO_2 sol particles is not completed in ageing times shorter than 40 h. In addition, it is assumed that the large RuO_2 particles in the coatings obtained with sols aged for times shorter than 40 h originate from the thermal decomposition of the residual $RuCl_3$ which had not been converted to RuO_2 by forced hydrolysis. The ratio of larger RuO_2 particles dispersed in the solid phase increased for ageing longer than 40 h, which causes a decrease of the charge related to the anodes obtained with these dispersions.

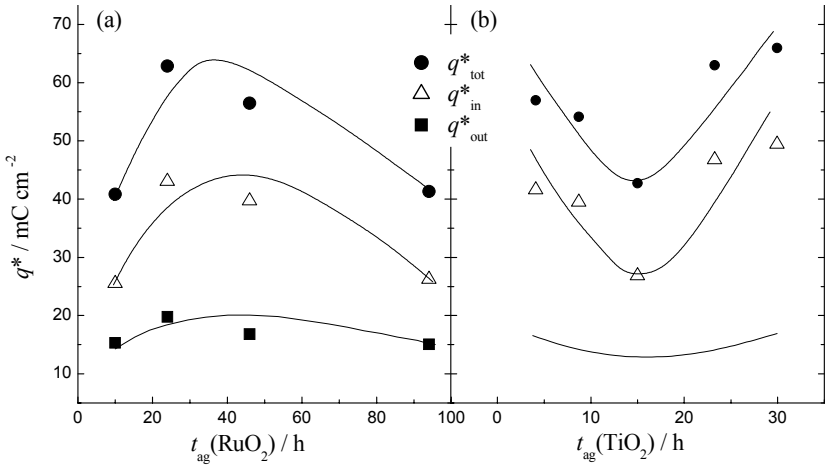

Fig. 12. The charge densities related to the total, inner and outer electrochemical surface area of the anode coating as functions of the ageing time of RuO_2 (a) and TiO_2 (b) sols used for the preparation of the coatings (Reprinted with permission of Elsevier).[23]

The influence of the ageing time of TiO_2 sol on the charges of the prepared anodes is shown in Fig. 12b. The values of all three types of charges decreased with increasing aging time of TiO_2 sol up to 15 h and then increased, although

the changes in q^*_{out} were less pronounced. Since the ratio of large sol particles increases with increasing ageing time, it could be concluded that the growth of TiO_2 particles during the ageing of TiO_2 sols causes the enlargement of the ESA of the coating obtained from these sols. For ageing times shorter than 15 h, similar to the case of the aging of the RuO_2 sol, particle formation was not completed and the ratio of large TiO_2 particles resulting from the thermal decomposition of residual $TiCl_3$ was high. Accordingly, the anode obtained with TiO_2 sol aged 15 h had the smallest ESA, which means that the solid phase of this sol contained the highest ratio of small TiO_2 particles.

The observed changes in ESA with ageing time of the TiO_2 sol are clearly reflected from the changes in the difference between the real and apparent surface area (*SAD*) obtained from STM measurements.[27] The changes in macro-, micro- and nano-roughness with $t_{ag}(TiO_2)$ are shown in Fig. 13. While the macroscopic roughness (880 nm × 880 nm) does not depend on $t_{ag}(TiO_2)$, the shapes of the micro- (250 nm × 250 nm) and nano-roughness (50 nm × 50 nm) dependencies are quite similar to the dependencies presented in Fig. 12b.

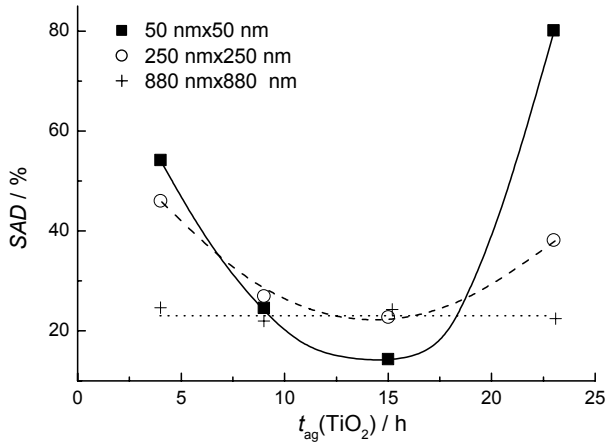

Fig. 13. Difference between real and apparent surface area (*SAD*, surface area difference) of RuO_2–TiO_2 coating prepared by the sol–gel procedure from differently aged TiO_2 sols. The ageing time of the RuO_2 sol was fixed at 46 h.

5. THE ACTIVITY FOR Cl_2 AND O_2 EVOLUTION REACTION

Tafel plots of the ATA prepared by the sol–gel procedure and thermal decomposition in the chlorine evolution reaction, as an indication of their electrocatalytic properties, are given in Fig. 14. The slope values close to 40 mV for both the sol–gel prepared and the thermally formed coatings correspond to the known mechanism of the chlorine evolution reaction on RuO_2-type coatings.[1,10,23] Higher current densities were registered for the sol–gel prepared anode. Normalized data (given by symbols ◇ and ○ for sol–gel and thermally prepared anode, respecttively) was obtained by dividing the measured currents densities by the corresponding q^*_{tot} values. Since the geometric factor (surface area) is eliminated in this way, the normalized data give the real catalytic activity of RuO_2.[33,40] The

normalized catalytic activity is practically the same for the sol–gel and the thermally formed anode. This leads to the conclusion that the difference in real surface areas of the sol–gel and thermally prepared anode, influenced by coating morphology, is the key parameter that causes the difference in their electrochemical behavior.[41]

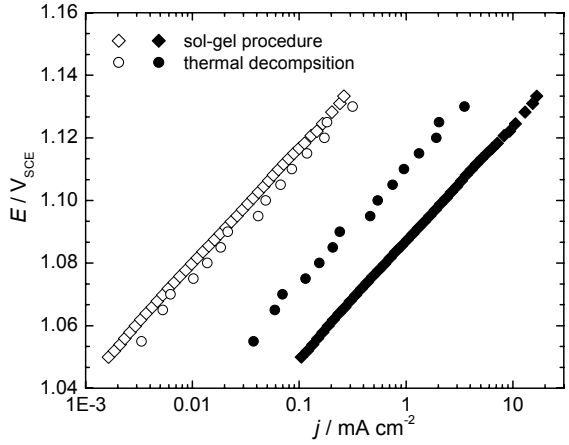

Fig. 14. The apparent (●,◆) and normalized (○,◇) Tafel plots of the sol–gel and thermally prepared anode. Electrolyte: 5 mol dm^{-3} NaCl, pH 2 (Reprinted with permission of Taylor & Francis).[41]

The normalized activities of the sol–gel prepared anode, however, show a dependence on the ageing time of oxide sol.[23] The dependences of the normalized values of the current densities on ageing time of the RuO_2 and TiO_2 sol are shown in Fig. 15. The changes of electrocatalytic activity with oxide particle size are similar to those obtained for ESA with oxide particle size (Fig. 12). The highest activities were achieved for anodes obtained with the RuO_2 sol aged for about 40 h and the TiO_2 sol aged for 30 h. The anode obtained with TiO_2 sol aged for 23 h had the smallest activity. The dependence of the anode electrocatalytic activity on the aging time was more pronounced in the case of the TiO_2 sol than in the case of the RuO_2 sol. The observed activity effects are probably due to the appearance of different states of the active sites, caused by different TiO_2 particle sizes and the revealing effect of TiO_2. A similar effect of the appearance of "new" active sites was also observed in the case of RuO_2 coatings obtained with rare earth oxides.[42,43] In the case of the RuO_2–TiO_2 binary oxide, the appearance of "new" active sites could be the consequence of different physical interaction between these two oxides, which depends on the TiO_2 particle size.

The ternary coating, obtained by the addition of a small amount of IrO_2, showed no significant difference in activity for chlorine and oxygen evolution with respect to the binary coating.[37] The Tafel plots given in Fig. 16 show that the polarization curves have the usual values of the Tafel slopes and negligibly higher activity of binary coating for chlorine evolution.

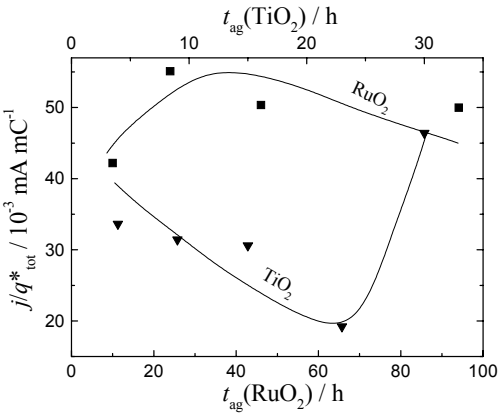

Fig. 15. Normalized activity of the sol–gel coatings at a potential of 1.10 V as a function of the ageing time of the RuO_2 and TiO_2 sols used for coating preparation (Reprinted with permission of Elsevier).[23]

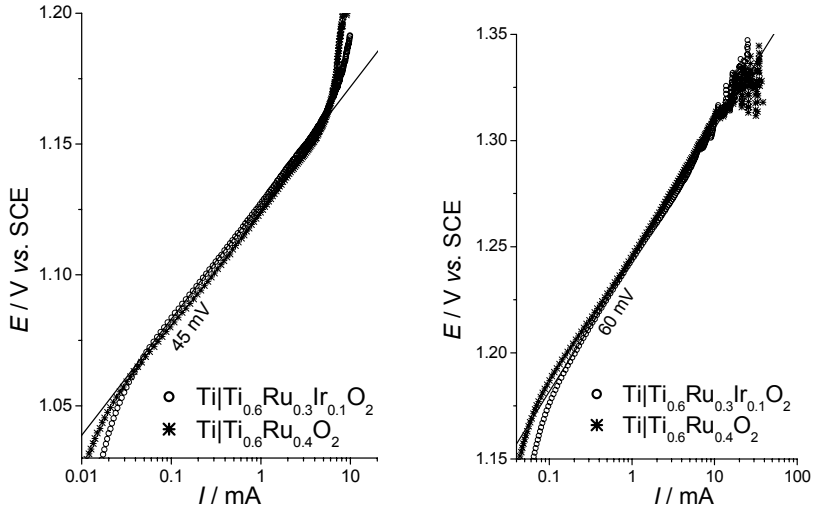

(a) (b)

Fig. 16. Tafel plots for the chlorine (a) and oxygen (b) evolution reaction registered for binary and ternary coating prepared by the sol–gel procedure.

6. THE STABILITY IN Cl_2 AND O_2 ELECTROLYSIS

The main industrial application of ATA is in long-term electrolysis of acid or neutral solutions, both chloride-containing and not. The anode wears during the electrolysis and finally ends its operation.[10–13] The dissolution of electrochemically active coating component (*e.g.* RuO_2 and IrO_2) and coating enrichment in insulating and inactive TiO_2 are recognized as the causes of the wearing process.[11] In addition to dissolution, the TiO_2 content can increase due to anodic oxidation of the Ti substrate, forming an insulating coating/substrate interlayer.[10] In this Section, the stability of binary and ternary coatings will be analyzed and com-

pared to the stability of traditional binary thermal coatings. The possible mechanism of anode wearing and the loss of electrocatalytic activity will be given.

The time dependence of the relative electrode potential, as the result of an accelerated corrosion test, for anodes prepared by the sol–gel and thermal procedure is shown in Fig. 17. The sol–gel prepared anodes with a binary coating showed considerably longer lifetimes than the thermal ones. The causes for the greater stability could be either the larger surface area of the sol–gel prepared anode or different mechanisms of the loss of catalytic activity or both. The morphology of the coating can influence any characteristic step in the mechanism. According to the STM data (Fig. 9), it is believed that the oxide particle size and distribution is more regular in the case of the sol–gel procedure then in the case of the thermal one, which produces a larger surface area and, consequently, the real current density of Ru dissolution on a sol–gel anode is smaller. In the same manner, the structure of the catalytic coating of a sol–gel prepared anode could be more homogeneous and the penetration of the electrolyte towards the titanium substrate thus hindered, which, besides the smaller current density, makes the chance for nonconductive intermediate TiO_2 layer formation smaller as compared to a thermally prepared anode.[28]

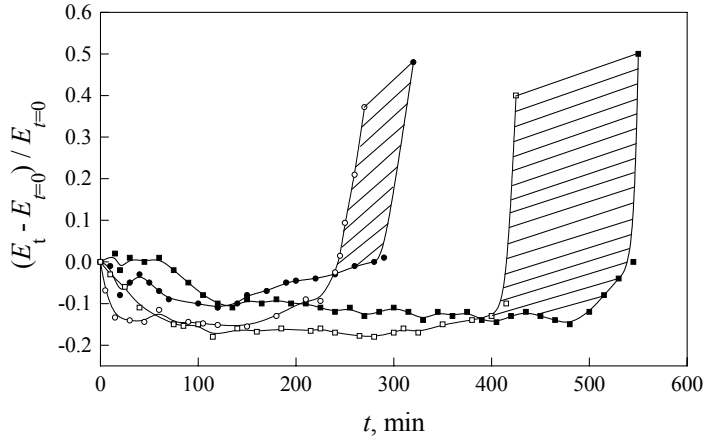

Fig. 17. The results of accelerated stability test: (–○–) thermally and (–□–) sol–gel prepared anodes with the shortest lifetime; (–●–) thermally and (–■–) sol-gel prepared anodes with the longest lifetime (the lifetimes for other samples of both types of anodes lay in the shaded areas). Electrolyte: 0.50 M NaCl, pH 2. Temperature: 35 °C, j = 2.0 A cm^{-2}. Total amount of oxide: 2.0 mg cm^{-2}. (Reprinted with permission of Elsevier).[28]

The stability of binary sol–gel coating can be controlled by changing the properties of the oxide sols. The influence of the ageing time of RuO_2 and TiO_2 sols on the stability of obtained anodes is presented in Fig. 18. The anode stability was the greatest when the RuO_2 sol was aged for about 40 h, *i.e.* when the ratio of small RuO_2 particles in RuO_2 sol was the highest. The change in stability

can be discussed in accordance to the changes of coating ESA with ageing of RuO_2 sol (Fig. 12). The rate of loss of activity *via* Ru dissolution decreases as the ESA increases or as the RuO_2 particle size decreases. In addition, the real current density of Ru dissolution is distributed more regularly if the RuO_2 particles are smaller, because they are more regularly packed throughout the bulk of the coating. Summarizing the above considerations, the anode with highest ratio of small RuO_2 particles, obtained with the RuO_2 sol aged for about 40 h, was the most stable due to it having the largest ESA.

The anode was more stable if the ageing time of the TiO_2 sol increased or if the TiO_2 particle size increased, due to similar consideration as in the case of the variation of the ageing time of the RuO_2 sol.

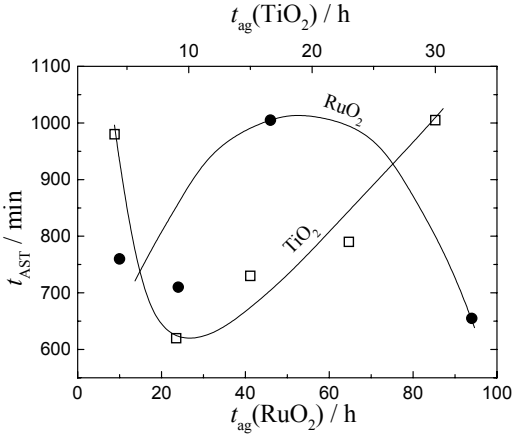

Fig. 18. The dependencies of RuO_2–TiO_2/Ti anode durability obtained by an accelerated stability test (AST) (electrolyte: 0.50 M NaCl, pH 2, j = 2.0 A cm^{-2}, 33 °C) on the ageing time of RuO_2 and TiO_2 sols used for the anode preparation. (Reprinted with permission of Elsevier).[23]

6.1. The mechanism of anode deactivation

In order to gain further insight into the wear mechanism, anodes with thin sol–gel or thermally prepared coatings were investigated in more detail when approaching the end of their service life.[36] The time dependences of the anode potential and the appropriate differential curves for the anodes with thin coatings prepared by sol–gel and thermal procedure are shown in Fig. 19. The current density was lower than in the tests shown in Figs. 17 and 18, in order to obtain well resolved wear steps at the end of the service life of the anodes. Two distinct regions in the plots in Fig. 19 can be seen. In the period below 29 h, the anode operation is stable. The potential has a stable value not exceeding the initial value by more than 20 %. The potential increased slightly during the first few hours of the AST, which could be the consequence of the presence of evolved gas bubbles at the anode surface. Tumultuous anode disordering is observed after 29 h as a continuous increase in the potential. The service lives of both the sol–gel and thermally prepared anode were practically the same, which was not the case with thick coatings, when the sol–gel procedure provided coatings with a longer service life (Fig. 17). The increase in potential and the rate of increase in potential were quite

similar for both the sol–gel and thermally prepared anode up to 30.7 h of AST, but a difference in the change of potential values was seen after this time. The rate of increase in potential of the thermally prepared anode was constant, being around 0.1 V min^{-1}, while the rate of the change in potential values of the sol–gel prepared anode considerably increased. These observations at the end of anode service life indicate a different deactivation mechanism for the anodes prepared by the sol–gel and thermal procedure.

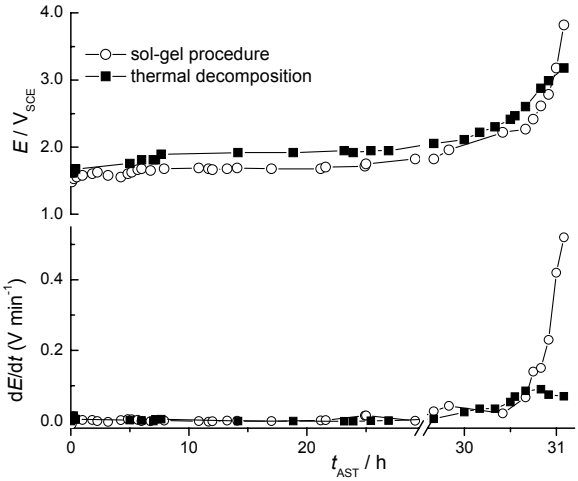

Fig. 19. The change of anode potential as a function of time during AST for RuO_2–TiO_2/Ti anodes prepared by the sol–gel procedure and thermal decomposition. Electrolyte: 0.50 mol dm^{-3} NaCl, pH 2, 25 °C. Current density: 700 mA cm^{-2}. (Reprinted with permission of Elsevier).[36]

6.2. The changes in electrochemically active surface area during deactivation

The changes in electrochemically active surface area of the coatings during AST are presented by the data given in Fig. 20, which shows the changes in apparent capacitances, calculated for a 1 V potential window from the cyclic voltammograms registered during AST and normalized to the apparent electrode surface area. After a period of 29.7 h of AST, the capacitance of both the sol–gel and thermally prepared anode increased in comparison to the capacitance Registered before AST. This could be explained by an increase in the real surface area of the coating. As the Ru species from the coating surface undergo dissolution during AST, the coating roughness increased, while the orifices of pores and cracks became wider. This makes the inner parts of the coating more accessible to the electrolyte. Assuming that the thermally prepared coating consisted of larger particles than the coating prepared by the sol–gel procedure,[44] the increase in coating roughness is more pronounced and the electrolyte penetrates more easily to the bulk of thermally prepared coating. This should lead to a more pronounced increase in capacitance of the thermally prepared coating for t_{AST} = 29.7 h. For AST times between 29.7 and 30.5 h, the capacitance decreased. During this short period, the intensive dissolution of Ru species leads to a considerable decrease in the number of active sites in the coating, *i.e.* electrochemically active surface area of the coating.

The essential difference in the C–t_{AST} dependencies for the sol–gel and thermally prepared anode appeared for t_{AST} larger than 30.5 h. While the capacitance of the sol–gel prepared anode continuously decreased going towards the end of its service life, the thermally prepared anode maintained the capacitance value registered for $t_{AST} \approx 30.5$ h. In this period, more reliable capacitance data for the thermally prepared anode are obtained by impedance measurements (see Section 6.4).

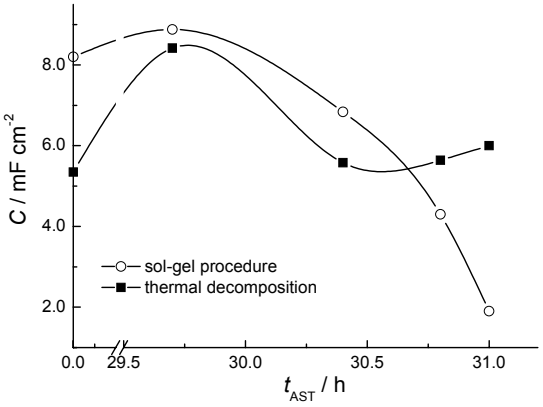

Fig. 20. The capacitances per apparent surface area of the anodes prepared by the sol–gel (○) and thermal procedure (■) calculated from cyclic the voltammograms recorded in 1.0 mol dm^{-3} $HClO_4$ during AST (Reprinted with permission of Elsevier).[36]

6.3. The loss of electrocatalytic activity

Polarization measurements in both NaCl and $HClO_4$ solution showed that the time of subjection of an anode to AST influenced the current, the Tafel slope and the potential range of the Tafel dependences. The apparent current density of chlorine evolution at a potential of 1.15 V, as well as the Tafel slope obtained from E–log j dependencies corrected for pseudo-ohmic resistance, and the values used for this correction are shown as function of t_{AST} in Fig. 21. Generally, the current decreased with t_{AST}, while the Tafel slope and pseudo-ohmic resistance increased for both the sol–gel and thermally prepared anode, as a result of anode deactivation. Similar dependencies were obtained for oxygen evolution from an $HClO_4$ solution.

As can be seen, the current–AST time dependences (Fig. 21a) are similar to the anodic C–t_{AST} dependencies (Fig. 20). There was an initial increase in the current density with t_{AST}, followed by a decrease as the anodes approach the end of their service life. The initial increase was more pronounced for the sol–gel prepared anode than for the thermally prepared one, which is opposite to the change in capacitance. In addition, an almost three times higher current density was registered before AST for the anode prepared by thermal decomposition. This behavior could be due to the larger number of active sites that participate in the O_2/Cl_2 evolution reaction,[45] owing to the wider cracks and pores of the thermally prepared anode.

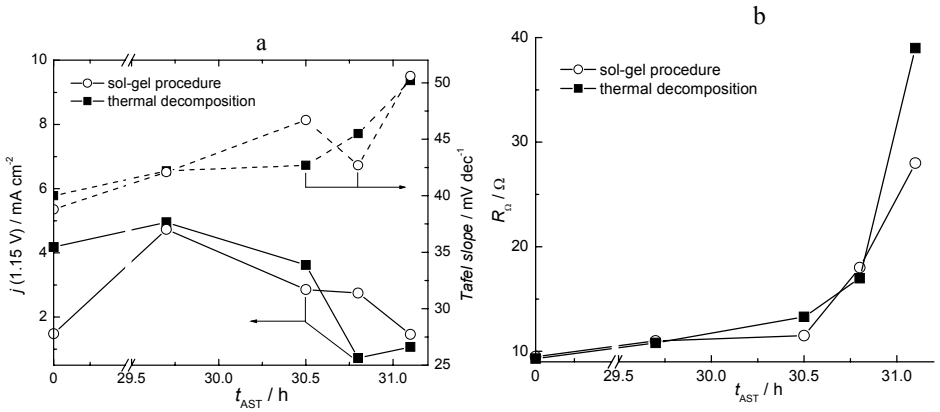

Fig. 21. The changes in current density at potential 1.15 V_{SCE} and Tafel slope registered by polarization measurements in 0.50 mol dm^{-3} NaCl, pH 2, (a) and pseudo-ohmic resistance used for correction of Tafel dependencies (b), during the accelerated stability test. (Reprinted with permission of Elsevier).[36]

According to the theory of porous electrodes,[45] the overvoltage exponentially decreases going from the surface toward the bulk of the porous layer. The decreasing function depends on the layer morphology. Considering layers of the same thickness but of different porosity and/or tortuosity, active sites at different distances from the surface are at different overvoltage values. The higher current densities registered for the thermally prepared anode before AST means that a larger number of inner active sites contribute to the reaction than in the case of the sol–gel prepared anode. Since the thermally prepared anode had wider pores and cracks, there is a better access of the electrolyte to the inner active sites of the thermally prepared anode and an easier release of gas bubbles from the pores and cracks. With the sol–gel prepared anode, only the active sites situated at the surface of the coating participate in reaction because of the narrow pores and cracks.

The increase in current density registered for both the sol–gel and thermally prepared anode for t_{AST} = 29.7 h (Fig. 21a) is due to an increase in the coating roughness. This initial period should be thus considered as an "opening of the inner coating structure". Once the inner coating structure is "opened", progressive dissolution of the active Ru species occurs, resulting in a decrease in the total number of active sites. For t_{AST} between 30.5 and 30.8 h, the current density for the thermally prepared anode decreased considerably, while the sol–gel prepared anode maintained the activity registered for t_{AST} = 30.5 h. This indicates a larger inner electrochemically active surface area of the sol–gel prepared coating, due to the more homogeneously dispersed oxide catalyst within the coating bulk.

As can be seen in Fig. 21b, the deactivation process during AST was also followed by a continuous increase in the pseudo-ohmic resistance within the coating. Similar values of the pseudo-ohmic resistance were obtained for both the

sol–gel and thermally prepared anode during AST, except at the end of the service life. For AST times longer than 30.7 h, a more pronounced increase in the pseudo-ohmic resistance was registered for the thermally than for the sol–gel prepared anode.

6.4. Impedance characteristics during the deactivation

The complex plane plots of the EIS data registered in 1 mol dm^{-3} $HClO_4$ during AST for the sol–gel and thermally prepared anode are shown in Fig. 22 and Fig. 23, respectively. The results of a fitting procedure are presented by the lines.

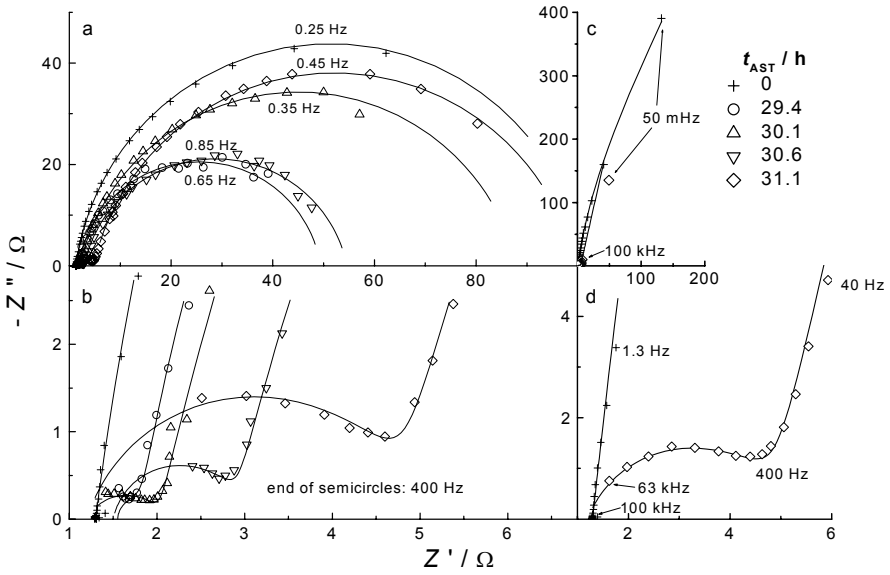

Fig. 22. Complex plane plots of the EIS data registered for the sol–gel prepared anode in 1.0 mol dm^{-3} $HClO_4$ at a potential of 1.25 V_{SCE} (a and b) during AST and at 0.50 V_{SCE} (c and d) before (0 h) and after (31.1 h) of AST; a,c – whole frequency range and b,d – high frequency range. (Reprinted with permission of Elsevier).[36]

A semicircle at low frequencies was registered at a potential of 1.25 V, which is associated with charge transfer in the oxygen evolution reaction (Figs. 22a and 23a), while a capacitive-like response was seen at a potential of 0.50 V (Figs. 22c and 23c). As can be seen in Figs. 22b and 23b, the continuous deactivation of both the sol–gel and thermally prepared anode during AST is manifested by the appearance of a growing semicircle in the high-frequency domain of the complex plane plots. In addition, there are simultaneous changes in the diameter of the low-frequency semicircle (Figs. 22a and 23a). The appearance of a high--frequency semicircle and the difference in the EIS data from the low-frequency domain, caused by anode deactivation, was also registered at 0.50 V. The similar values of the diameters of the high-frequency semicircle registered at different

potentials (1.25 and 0.50 V) after the same AST time (31.1 h) mean that the corresponding resistance was not due to a charge transfer process. Although the changes in EIS behavior during AST are similar for both the sol–gel and thermally prepared anode, the difference in characteristics of the registered semicircles as well as in the capacitive behavior at 0.50 V is obvious.

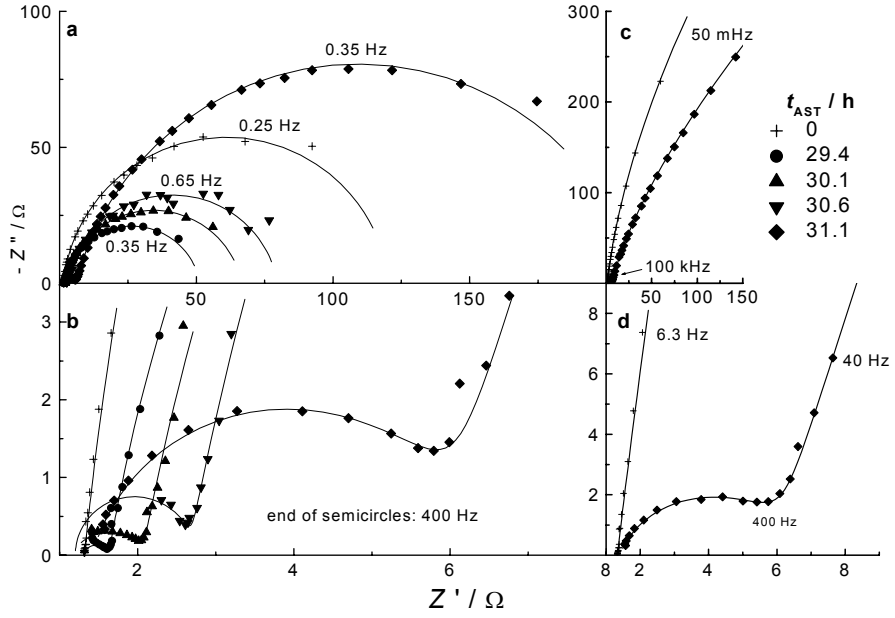

Fig. 23. Complex plane plots of EIS data registered for the thermally prepared anode in 1.0 mol dm^{-3} $HClO_4$ at a potential of 1.25 V_{SCE} (a and b) during AST and at 0.50 V_{SCE} (c and d) before (0 h) and after (31.1 h) AST; a,c – whole frequency range and b,d – high frequency range. (Reprinted with permission of Elsevier).[36]

The complex plane plots of EIS data registered in 0.50 mol dm^{-3} NaCl, pH 2, at a potential of 1.15 V, before and after AST for both the sol–gel and thermally prepared anode are shown in Fig. 24. A semicircle is seen before AST in the high-frequency domain, which relates to charge transfer in the chlorine evolution reaction. At lower frequencies, a straight line follows the semicircle. By fitting procedure using the Randles–Shevchik equivalent circuit with a constant phase element instead of a Warburg element, the values of the *n* parameter between 0.49 and 0.55 were obtained. This indicates diffusion limitations to the charge transfer process.

The diameter of the semicircle registered before AST for the thermally prepared anode was larger in comparison to that for the sol–gel prepared anode (Fig. 24). This indicates the greater activity of the sol–gel prepared anode for the chlorine evolution reaction, contrary to the higher apparent current density registered for the thermally prepared anode by polarization measurements (Fig. 21). This

observation supports the conclusion that the higher current densities of the thermally prepared anode were due to the wider pores and cracks of this anode.

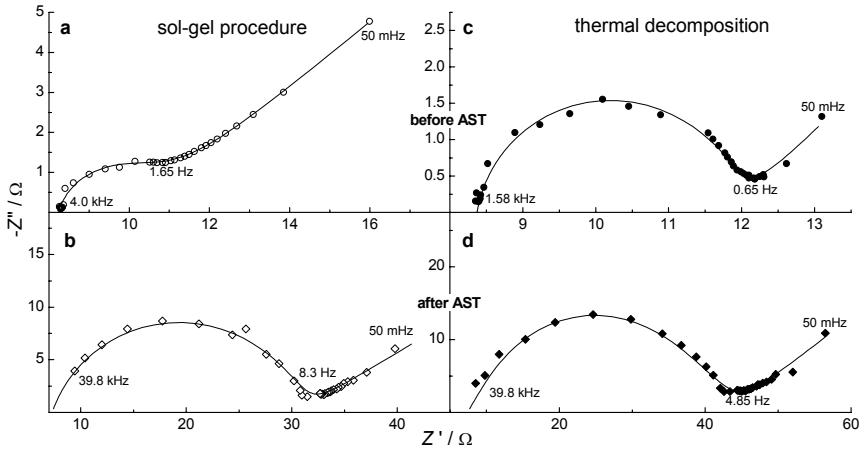

Fig. 24. Complex plane plots of EIS data registered for the sol–gel (a and b) and thermally (c and d) prepared anode in 0.50 mol dm^{-3} NaCl, pH 2, at the potential 1.15 V_{SCE} before (0 h) and after (31.1 h) AST. (Reprinted with permission of Elsevier).[36]

As a consequence of anode deactivation, semicircles of considerably larger diameters in comparison to those registered before AST are seen in Fig. 24. In addition, the semicircles are shifted towards higher frequencies. Semicircles of similar diameters were also registered at 0.50 V in NaCl solution after AST (not shown), which implies that the semicircle related to charge transfer and that appearing as a result of anode deactivation are overlapped. In NaCl solution, the resistance related to the high-frequency semicircle after AST is an order of magnitude greater than in $HClO_4$ solution (Figs. 22d and 23d), which suggests that this resistance refers to the electrolyte in the pores (pore resistance, R_p) of an insulating layer formed on the coating surface during anode deactivation. The ohmic resistance, R_Ω is also an order of magnitude larger in NaCl solution (*e.g.*, Figs. 22b and 24b). The sum of R_Ω and R_p, as obtained by a fitting procedure[46] of the EIS data registered in NaCl solution, for the sol–gel and thermally prepared anode after AST is 27 and 41 Ω, respectively. These values are very similar to the values of the pseudo-ohmic resistance used for the correction of the Tafel plots (Fig. 21b), which confirms that Rp corresponds to the ohmic resistance of the electrolyte.

The part of the complex plane plots in Fig. 24 related to the diffusion limitations differs for the anodes prepared by the sol–gel procedure and thermal decomposition, as well as for the anode before and after AST. This means that the transport of the reacting species involves diffusion through the electrolyte in the coating pores. The diffusion limitations were more pronounced for the sol–gel prepared anode than for the thermally prepared one, which indicates the wider

pores and cracks of the latter. Due to anode deactivation, the diffusion tails for both the sol–gel and thermally prepared anode commence at higher frequencies if compared to the tails before AST, which indicates that the reacting species reach active sites situated deeper in the coating.

6.4.1. Changes in the capacitive behavior

The best description of the impedance behavior of the active and deactivated coatings at 0.50 V (Figs. 22 and 23) was obtained using a transmission-line equivalent electrical circuit (EEC).[2] This kind of circuit indicates the capacitive responses of active sites situated on the outer and inner active surface, similarly to Eqs. (2) and (3). For the active (before AST) sol–gel and thermally prepared anode, as well as for the deactivated (after AST) sol–gel prepared coatings, a first--order transmission line was used, $R_\Omega(Q_{out}(R_p(Q_{in})))$ (the inscription according to ref. 46), where R_Ω is the ohmic resistance of the electrolyte, R_p is the pore resistance of the coating layer facing the electrolyte, while Q_{out} and Q_{in} are constant phase elements (CPE) related to the capacitance of the coating outer and inner active surfaces, respectively.

For the deactivated thermally prepared anode, a second-order transmission line EEC was applied to describe the anode impedance behavior at 0.50 V. This EEC indicates the separable EIS response of distinctive inner coating layers; hence the circuit inscription is $R_\Omega(Q_{out}(R_p(Q_{in}(R'(Q_{in}'))))))$. R' is the resistance closely related to the pore resistance of the inner layer to which Q_{in} relates, while Q_{in}' is the CPE related to the capacitance of an inner layer placed deeper in the bulk of the coating.

The values of the parameters of the EEC elements are given in Table I. The high R_p values obtained for both the sol–gel and thermally prepared active coatings indicate that the active surface of the inner coating is hardly accessible to the electrolyte. A lower R_p value was obtained for the thermally prepared anode, which supports the conclusion that this anode consisted of wider pores and cracks than the sol–gel prepared one, as concluded from the CV and polarization measurements. Considering Q_{out} as the capacitance of the surface layer (n values close to 1), values of 7.6 and 5.4 mF cm^{-2} (per apparent surface area) were calculated for the sol–gel and thermally prepared anode, respectively. These values agree with those registered by CV for t_{AST} = 0 h (Fig. 20), which confirms the difficult electrolyte penetration to the active surface of the inner coating due to narrow pores of high R_p values. The sweep rate applied in the CV was rather high for the active sites of the inner coating to be seen in the CV response. This is also seen from Y_0 values of Q_{in} for active coatings, with n values close to 0.5, which indicate that Q_{in} represents not only the capacitive behavior, but also the frequency-dependent diffusion processes in coating pores. Mobility of the ions of different radii is different, and can be considerably slower within the pores than

in electrolyte bulk.[47] This results in the formation of an instant electric micro--field within the pores, which slows down the faster ions and speeds up the slower ones. At higher frequencies, the ions cannot follow the fast alternation of potential, which is seen as a diffusion limitation represented by the values of the n parameter close to 0.5.[48] The value of $Y_{0,in}$ of the Q_{in} element indicates that almost one-third of the active sites of the coating are hardly accessible to the electrolyte (if $Y_{0,in}$ is compared to $Y_{0,in} + Y_{0,out}$).

TABLE I. Parameters of the equivalent electrical circuits used for the description of the impedance behavior of the investigated anodes at 0.50 V_{SCE} in 1.0 mol dm^{-3} $HClO_4$ (Reprinted with permission of Elsevier)[36]

Parameter		Anode prepared by:			
		Sol-gel procedure		Thermal decomposition	
		Before AST	After AST	Before AST	After AST
R_Ω / Ω		1.3	1.2	1.2	1.4
R_p / Ω		994	3.9	926	5.2
R' / Ω		–	–	–	360
Q_{out}	$Y_{0,out}$ / $k\Omega^{-1}$ s^n	6.0	0.12	4.2	0.095
	n	0.93	0.78	0.93	0.80
Q_{in}	$Y_{0,in}$ / $k\Omega^{-1}$ s^n	2.6	1.6	1.7	1.3
	N	0.66	0.86	0.44	0.83
Q_{in}'	$Y_{0,in}$' / $k\Omega^{-1}$ s^n	–	–	–	1.2
	n	–	–	–	0.40
ΣC / mF cm^{-2}		11.0	2.2	7.5	3.3

As the result of deactivation, R_p and Y_0 of Q_{out} considerably decreased for both the sol–gel and thermally prepared coating (Table I), which is the conesquence of the dissolution of Ru species from the outer coating surface. The coating porosity increased but the number of active sites decreased. A lower Y_0 value of Q_{out} was obtained after AST for the thermally prepared anode, which implies a faster dissolution of Ru species from outer coating surface than in the case of the sol–gel prepared anode. For the sol–gel prepared anode, the Y_0 of Q_{in} decreased, also for the same reason, but the decrease in the Y_0 value of Q_{in} for the thermally prepared anode was negligible. In addition, the n values of Q_{in} increased after AST for both the sol–gel and thermally prepared anode, which supports the fact that the electrolyte penetrates to the inner active sites of deactivated coatings easier than to those of the active coatings. It can be seen that the sum of the Y_0 values of Q_{in} and Q_{in}' for the deactivated thermally prepared coating (2.5 $k\Omega^{-1}$ s^n) is considerably higher than the Y_0 value of Q_{in} for the deactivated sol–gel prepared coating (1.6 $k\Omega^{-1}$ s^n), despite the lower Y_0 value of Q_{in} for the thermally prepared coating before AST (1.7 $k\Omega^{-1}$ s^n). This shows that Ru dissolution prevails at the inner active surface of the sol–gel prepared coating, which is not the case for the thermally prepared coating. As a consequence, a conside-

rably greater number of active sites remain on the inner active surface of the thermally prepared coating than on the inner active surface of the sol–gel prepared coating. This is also seen from the values of the overall coating capacitance, ΣC, given in Table I. The overall capacitance was calculated as the sum of the Y_0 values of Q_{out}, Q_{in} and Q_{in}', since these elements are in parallel. A larger ΣC value was obtained for the sol–gel prepared coating before AST than for the thermally prepared one, but the reverse was obtained after AST.

The resistance registered after AST for the thermally prepared anode, being the sum of R_p and R' (365 Ω), was considerably greater than the R_p of the sol–gel prepared anode (3.5 Ω), although the thermally prepared anode consisted of wider pores and cracks. This increased resistance could only be due to an insulating TiO_2 layer growing in the coating/substrate interphase.

6.4.2. Pore resistance and charge transfer resistance during deactivation

The impedance behavior of active coatings at 1.25 V (Figs. 22 and 23) is described through the simple EEC $R_\Omega(R_{ct}Q)$, where R_{ct} is the charge transfer resistance and Q is the CPE related to the coating resistance. As the active sites from the coating surface dissolve during AST, the EEC should be transformed into $R_\Omega(R_pQ_{out})(R_{ct,in}Q_{in})$. The physical meanings assigned to the EEC elements are based on the assumption that charge transfer at the deactivated anodes occurs mostly at the inner active sites, since the active sites disappeared from the outer surface during deactivation. Boodts and coworkers used a similar EEC to simulate the behavior of deactivated oxide coatings of different composition.[9,18]

The changes in R_p, R_{ct} (*i.e.*, $R_{ct,in}$) and the coating capacitance of both the sol–gel and thermally prepared anode during AST are given in Fig. 25. The coating capacitance was calculated with Q_{out} and Q_{in} in series. The changes in the coating capacitance are similar to the changes seen in Fig. 20. Since R_p does not depend on the anode potential, the R_p value for the active coating was taken from the EIS measurements at 0.50 V (Table I).

The R_{ct} value for the thermally prepared anode is higher than the value obtained for the sol–gel prepared anode, which indicates a higher activity of the latter. In the AST period below 29.7 h, R_{ct} and R_p considerably decreased. As the surface active sites dissolved, the pores and cracks became wider and a larger number of active sites from the inner active surface are exposed to the electrolyte. The charge transfer resistance is $R_{ct,in}$, owing to the effect recognized in Section 3.3 as the "opening of the inner coating structure". Once the inner active sites are opened for electrolyte penetration, they begin to dissolve, which results in the increase in R_{ct} and R_p for the AST period between 29.7 and 30.1 h. In the AST period between 30.1 and 31.1 h, the opening of the subsequent inner active surface, placed deeper into the bulk of the coating, is seen for sol–gel prepared anode as an additional decrease and subsequent increase in R_{ct}, while R_p continu-

ously increases. This effect was not seen for the thermally prepared anode. The significantly greater R_{ct} value after AST (31.1 h) was caused by the increasing content of TiO_2 in the coating/substrate interphase of this anode during AST.

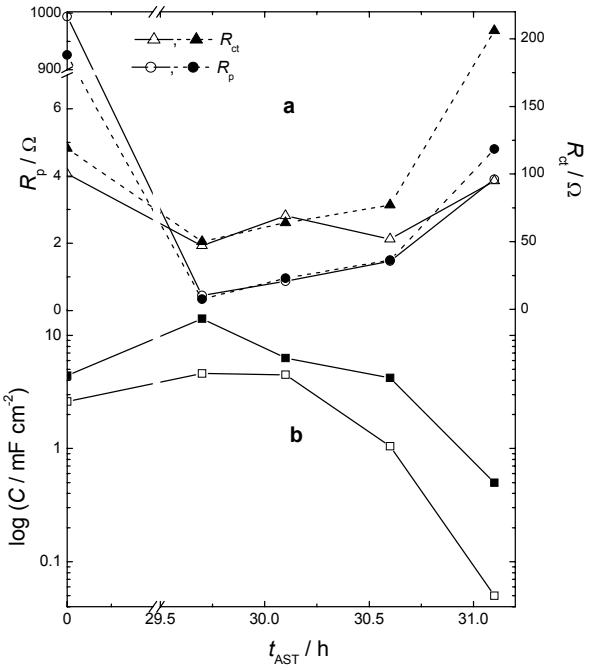

Fig. 25. The change in the pore resistance, R_p, charge-transfer resistance, R_{ct}, (a) and coating capacitance, C, (b) during AST for RuO_2–TiO_2/Ti anodes prepared by the sol–gel procedure and thermal decomposition. Empty symbols: sol–gel procedure, solid symbols: thermal decomposition. (Reprinted with permission of Elsevier).[36]

The obtained results show that the first stage in the deactivation mechanism for both the sol–gel and thermally prepared anode was Ru dissolution from the surface layer of the coating. In the case of the thermally prepared anode, the parallel progressive oxidation of the Ti substrate occurred in the subsequent stage, which additionally enlarged the insulating TiO_2 layer in the coating/substrate interphase. For the sol–gel prepared anode, this parallel process was less pronounced. This difference could explain the fact that the sol–gel prepared anode lasted longer in NaCl electrolysis, as was registered earlier, especially when thick coatings are considered.[23,28]

6.5. The stability of the ternary RuO_2–TiO_2–IrO_2 coating

The stability to ATA can be improved by the addition of IrO_2, which is believed to be more stable against dissolution during simultaneous vigorous oxygen evolution.[17] For this reason, commercial activated titanium anodes, available for cathodic protection purposes contain iridium oxide in small amounts, in addition to ruthenium and titanium oxide. Particularly, a good activity of ATA in seawater is important for their application in cathodic protection. The results of accelerated stability test performed in seawater on a ternary and a binary coating are shown

in Fig. 26, as the time dependence of the anode potential at a constant current density. Since IrO_2 is more stable during the simultaneous evolution of oxygen and chlorine, the durability of the ternary coating was longer than that of the binary coating. A tentative explanation for considerably larger stability of the ternary coating could be as follows. The reactions of RuO_2 dissolution and oxygen evolution proceed in parallel.[11] The mechanism for RuO_2 dissolution could be:

$$RuO_2 + H_2O \rightarrow RuO_2{-}OH + H^+ + e^- \quad (5)$$

$$RuO_2{-}OH \rightleftharpoons RuO_3 + H^+ + e^- \quad (6)$$

$$RuO_3 + H_2O \rightleftharpoons RuO_3{-}OH + H^+ + e^- \quad (7)$$

$$RuO_3{-}OH \rightleftharpoons RuO_4 + H^+ + e^- \quad (8)$$

while for the oxygen evolution reaction, the proposed mechanism[11] suggests that Steps (7) and (8) should be replaced by:

$$2RuO_3 \rightleftharpoons 2RuO_2 + O_2 \quad (9)$$

The Steps (5) and (6) are the same for the two mechanisms, with the formation of $RuO_2{-}OH$, Step (5), as the rate-determining step. The species in the subsequent Steps (7)–(9) decompose giving either oxygen or RuO_4, which is soluble in acid solutions. However, when IrO_2 is present in the coating, oxygen evolution occurs mainly at the IrO_2 active sites. This hinders the decomposition reactions on the RuO_2 active sites and considerably extends the service life of the coating.

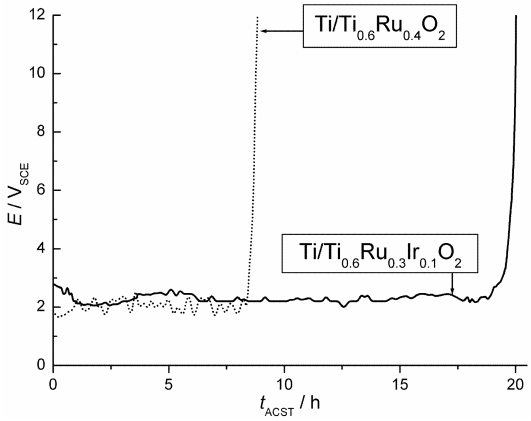

Fig. 26. Time dependences of the potential of the sol–gel anodes with ternary and binary coating during the accelerated stability test in seawater at a current density of 0.60 A cm^{-2}.[37]

CONCLUSIONS

The results obtained in investigations of activated titanium anodes prepared by the inorganic sol–gel procedure are reviewed. Microscopic investigations of oxide sols and coatings showed that the ageing time of the sols defines the coating morphology and, consequently, the electrochemical behavior of a coating. Better electrochemical characteristics, including anode stability in electrolysis, was registered for a combination of small RuO_2 and large TiO_2 particles.

Anode deactivation is manifested by an increased coating resistance and by a deceased electrochemically active surface area. The increase in the coating resistance is more pronounced for traditional thermally prepared coatings, while sol–gel prepared coatings show a more pronounced decrease in the electrochemically active surface area. The initial increase in coating resistance is caused by the dissolution of Ru species from the coating surface facing the electrolyte, which restricts the coating activity to the active sites of the inner coating. For the thermally prepared anode, there is additional increase in coating resistance due to the enlargement of an insulating TiO_2-rich layer in the coating/substrate interphase. This enlargement is considerably less pronounced during the deactivation of sol–gel prepared anodes. Thus, the main cause for deactivation of a thermally prepared anode is a TiO_2 layer in the interphase, while the dissolution of a Ru species prevails in the deactivation process of sol–gel prepared coatings, which makes the coating surface layers enriched in TiO_2.

Investigations of a ternary, sol–gel prepared RuO_2–TiO_2–IrO_2 coating on titanium showed that it has similar basic electrochemical properties as a binary RuO_2–TiO_2 coating. However, the results of an accelerated stability test on the binary and ternary coating showed that the ternary coating was considerably more stable during exploitation in seawater than the binary one. This is the consequence of the greater stability of IrO_2 under vigorous oxygen and chlorine evolution in comparison to RuO_2. This fact makes the ternary coating a better candidate as the anode in real applications for cathodic protection.

Acknowledgements. Financial support from the Ministry of Science and Technological Development of the Republic of Serbia under Grant No. 14062 is acknowledged. Thanks are due to the colleagues which significantly participated in the research work: Slobodan K. Milonjić ("Vinča" Institute of Nuclear Sciences, University of Belgrade, Serbia), Aleksandar B. Dekanski (ICTM–IEC, University of Belgrade, Serbia), Vesna B. Mišković-Stanković (Faculty of Technology and Metallurgy, University of Belgrade, Serbia) and Radoslav T. Atanasoski (Present address: 3M Company, St. Paul, MN, USA).

И З В О Д

ТИТАНСКЕ АНОДЕ АКТИВИРАНЕ ОКСИДНОМ ПРЕВЛАКОМ ДОБИЈЕНОМ СОЛ–ГЕЛ ПОСТУПКОМ

ВЛАДИМИР В. ПАНИЋ[1] и БРАНИСЛАВ Ж. НИКОЛИЋ[2]

[1]ИХТМ – Центар за електрохемију, Његошева 12, Београд и [2]Технолошко–металуршки факултет, Карнегијева 4, Београд

У раду је дат је преглед својстава активираних титанских анода, RuO_2–TiO_2/Ti и RuO_2–TiO_2–IrO_2/Ti, добијених сол–гел поступком од неорганских оксидних солова. RuO_2 и TiO_2 солови добијени су форсираном хидролизом одговарајућих хлорида метала у киселој средини. Морфологија добијених солова испитивана је трансмисионом електронском микроскопијом. Хемијски сатав RuO_2 сола испитиван је дифракцијом х-зрака и термогравиметријском анализом. Механизам губитка електрокаталитичке активности RuO_2–TiO_2/Ti анода испитиван је праћењем промена електрохемијских својстава аноде у реакцијама издвајања хло-

ра и кисеоника, као и на потенцијалу отвореног кола, током деградације аноде. Ове електрохемијске карактеристике аноде испитиване су методама цикличне волтаметрије, спектроскопије електрохемијске импеданције и поларизационим мерењима. Промене у електрохемијским својствима аноде добијене сол–гел поступком поређене су са променама које су регистроване за RuO_2–TiO_2/Ti аноду добијену традиционалним поступком термичке разградње хлорида метала. На основу ових испитивања произилази да је основни узрок губитка електрокаталитичке активности аноде добијене сол–гел поступком електрохемијско растварање RuO_2, док је узрок деградације аноде добијене термичком разградњом раст непроводног TiO_2 слоја у међуфази превлака/титанска подлога. Резултати убрзаног теста стабилности RuO_2–TiO_2/Ti и RuO_2–TiO_2–IrO_2/Ti аноде показују да је тројна превлака знатно стабилнија од двојне, због веће стабилности оксида иридијума у поређењу са оксидом рутенијума.

(Примљено 3. марта, ревидирано 2. септембра 2008)

REFERENCES

1. S. Trasatti, in *Interfacial Electrochemistry – Theory, Experiment and Applications*, A. Wieckowski, (Ed.), Marcel Dekker Inc., New York, 1999, p. 769.
2. B. Conway, *Electrochemical Supercapacitors – Scientific Fundamentals and Technological Applications*, Plenum Publishers, New York, 1999, p. .
3. T. Jow, J. Zheng, *J. Electrochem. Soc.* **145** (1998) 49
4. M. Ramani, B. Haran, R. White, B. Popov, *J. Electrochem. Soc.* **148** (2001) A374
5. [5]D. Rolison, P. Hagans, K. Swider, J. Long, *Langmuir* **15** (1999) 774
6. [6]K.-W. Park, B.-K. Kwon, J.-H. Choi, In-Su Park, Y.-M. Kim, Y.-E. Sung, *J. Power Sources* **109** (2002) 439
7. S. Trasatti, *Electrochim. Acta* **36** (1991) 225
8. V. A. Alves, L. A. Silva, J. F. C. Boodts, *J. Appl. Electrochem.* **28** (1998) 899
9. L. M**.** Da Silva, L. A. De Faria, J. F. C. Boodts, *J. Electroanal. Chem.* **532** (2002) 141
10. V. M. Jovanović, A. Dekanski, P. Despotov, B. Ž. Nikolić, R. T. Atanasoski, *J. Electroanal. Chem.* **339** (1992) 147
11. Lj. M. Gajić-Krstajić, T. Lj. Trišović, N. V. Krstajić, *Corr. Sci.* **46** (2004) 65
12. G. N. Martelli, R. Ornelas, G. Faita, *Electrochim. Acta* **39** (1994) 1551
13. F. Beck, *Electrochim. Acta* **34** (1992) 811
14. J.-M. Hu, J.-Q. Zhang, C.-N. Cao, *Inter. J. Hydrogen Ener*. **29** (2004) 791
15. V. V. Gorodetskii, V. A. Neburchilov, V. I. Alyab'eva, *Russ. J. Electrochem*. **41** (2005) 1111
16. T.-X. Cai, H. Chen, H. Ju, L.-N. Lu, *Corr. Potection* **27** (2006) 522
17. M. G. Pavlović, A. B. Dekanski, *J. Solid State Electrochem*. **1** (1997) 208
18. T. A. F. Lassali, J. F. C. Boodts, L. O. S. Bulhões, *J. Appl. Electrochem.* 30 (2000) 625
19. V. V. Panić, A. B. Dekanski, S. K. Milonjić, V. B. Mišković-Stanković, B. Ž. Nikolić, *Russ. J. Electrochem.* **42** (2006) 1173
20. V. V. Panić, A. B. Dekanski, S. K. Milonjić, V. B. Mišković-Stanković, B. Ž. Nikolić, *J. Serb. Chem. Soc.* **71** (2006) 1173
21. V. V. Panić, T. R. Vidaković, A. B. Dekanski, V. B. Mišković-Stanković, B. Ž. Nikolić, *J. Electroanal. Chem*. **609** (2007) 120
22. V. Panić, T. Vidaković, S. Gojković, A. Dekanski, S. Milonjić, B. Nikolić, *Electrochim. Acta* **48** (2003) 3805
23. V. Panić, A. Dekanski, S. Milonjić, R. Atanasoski, B. Nikolić, *Electrochim. Acta* **46** (2000) 415

24. V. Panić, A. Dekanski, S. Milonjić, R. Atanasoski, B. Nikolić, *Mater. Sci. Forum* **352** (2000) 117
25. J. P. Zheng, T. R. Jow, *J. Electrochem. Soc.* **142** (1995) L6
26. J. Zhang, D. Jiang, B. Chen, J. Zhu, L. Jiang, H. Fang, *J. Electrochem. Soc.* **148** (2001) A1362
27. V**.** Panić, A. Dekanski, G. Wang, M. Fedoroff, S. Milonjić, B. Nikolić, *J. Colloid Interface Sci*. **263** (2003) 68
28. V. Panić, A. Dekanski, S. Milonjić, R. Atanasoski, B. Nikolić, *Colloids Surfaces A* **157** (1999) 269
29. A. De Battisti, G. Lodi, M. Cappadonia, G. Battaglin, R. Kötz, *J. Electrochem. Soc.* **136** (1989) 2596
30. M. Guglielmi, P. Colombo, V. Rigoto, G. Battaglin, A. Boscolo-Boscoletto, A. De Battisti, *J. Electrochem. Soc.* **139** (1992) 1655
31. K. Komeyama, S. Shohji, S. Onoue, K. Hishimura, K. Zahikozawa, Y. Takasu, *J. Electrochem. Soc.* **140** (1993) 1034
32. F. I. Mattos-Costa, P. de Lima-Neto, S. A. S. Machado, L. A. Avaca, *Electrochim. Acta* **44** (1998) 1515
33. S. Ardizzone, S. Trasatti, *Adv. Colloid Interface Sci.* **64** (1996) 173
34. V. V. Panić, A. B. Dekanski, V. B. Mišković-Stanković, S. K. Milonjić, B. Ž. Nikolić, *J. Serb. Chem. Soc.* **68** (2003) 979
35. L. M. Da Silva, L. A. De Faria, J. F. C. Boodts, *Electrochim. Acta* **47** (2001) 395
36. V. Panić, A. Dekanski, V. B. Mišković-Stanković, S. Milonjić, B. Nikolić, *J. Electroanal. Chem*. **579** (2005) 67
37. V. V. Panić, B. Ž. Nikolić, *J. Serb. Chem. Soc*. **72** (2007) 1393
38. L. A. De Faria, J. F. C. Boots, S. Trasatti, *Electrochim. Acta* **42** (1997) 3525
39. E. Matijević, M. Budnik, L. Meites, *J. Colloid Interface Sci.* **61** (1977) 352
40. F. I. Mattos-Costa, P. de Lima-Neto, S. A. S. Machado, L. A. Avaca, *Electrochim. Acta* **44** (1998) 1515
41. V. Panić, A. Dekanski, V. Mišković-Stanković, B. Nikolić, S. Milonjić, *Mater. Manufacturing Proc.* **20** (2005) 89
42. Y. Murakami, T. Kondo, Y. Shimoda, H. Kaji, K. Yahikozawa, Y. Takasu, *J. Alloys Comp.* **239** (1996) 111
43. Y. Takasu, T. Arikawa, K. Yanase, X.-G. Zhang, Y. Murakami, *J. Alloys Comp.* **261** (1997) 172
44. V. Panić, A. Dekanski, S. Milonjić, R. Atanasoski, B. Nikolić, *J. Serb. Chem. Soc*. **65** (2000) 649
45. Yu. Chizmadzev, Yu. Chirkov, in *Comprehensive Threatise of Electrochemistry Vol. 6,* E. Yeager, J. Bockris, B. Conway, S. Sarangapani, (Eds.), Plenum press, New York, 1983, Ch. 5.
46. B. Boucamp, *Equivalent Circuit (EQUIVCRT.PAS) Users Manual*, University Twente, Enschede, the Netherlands, 1989
47. V. B. Mišković-Stanković, J. B. Zotović, Z. Kačarević-Popović, M. D. Maksimović, *Electrochim. Acta* **44** (1999) 4269
48. W. H. Mulder, J. H. Sluyters, T. Pajkossy, L. Nyikos, *J. Electroanal. Chem*. **285** (1990) 103.

www.shd.org.rs

Journal of the Serbian Chemical Society

JSCS@tmf.bg.ac.yu • www.shd.org.rs/JSCS

J. Serb. Chem. Soc. 73 (11) 1113–1122 (2008) UDC 546.193+547.461.2:543.555:541.132.3
JSCS–3790 *Original scientific paper*

Conductometric and pH metric investigations of the oxalic acid and $NaAsO_2$ reaction

MIRJANA V. OBRADOVIĆ[1], SLAVICA M. SUNARIĆ[2]*, SNEŽANA S. MITIĆ[1] and DRAGAN S. VESELINOVIĆ[3#]

[1]*Department of Chemistry, Faculty of Natural Sciences and Mathematics, University of Niš, Višegradska 33, P.O. Box 224,* [2]*Faculty of Medicine, Department of Pharmacy, University of Niš, Bulevar dr Zorana Djindjića 81 and* [3]*Faculty of Physical Chemistry, University of Belgrade, P.O. Box 550, Serbia*

(Received 10 January, revised 15 May 2008)

Abstract: The reaction between $NaAsO_2$ and oxalic acid was studied by pH-metric and conductometric measurements, applying the methods of continual variation and pH-metric and conductometric titration. It was found that oxalic acid forms a complex anion of the type $[AsOC_2O_4]^-$. The relative stability constant of the complex at ionic strengths, I, of 0.10 (log K_r = 4.70), 0.20 (log K_r = = 4.51), 0.50 (log K_r = 4.24) and 0 (log K_r^0 = 5.05) and thermodynamic parameters were calculated using the data obtained by pH-metric measurements at 25.0±0.1 °C (ΔH = 10.5 kJ mol^{-1}, ΔG = –29.0 kJ mol^{-1}, ΔS = 133 J mol^{-1} K^{-1}).

Keywords: arsenic(III); oxalic acid; complex; conductometry; pH-metry.

INTRODUCTION

Literature data are available for Mo(VI) and W(VI) complexes, *i.e.*, complexes of a metal in the form of an oxyanion, with different monobasic acids (HAc), such as formic, acetic, propionic and ascorbic.[1–3] The ligand to metal ratio in these complexes, $[WO_3Ac_2]^{2-}$ and $[MoO_3Ac_2]^{2-}$, is 2:1. With oxalic acid, Na_2WO_4 and Na_2MoO_4 form $[WO_3C_2O_4]^{2-}$ and $[MoO_3C_2O_4]^{2-}$ complexes, respectively.[4] Tetracycline (H_3T_C) forms the complexes $[WO_3(HT_C)]^{2-}$, $[WO_3(H_2T_C)_2]^{-}$ and $[MoO_3(H_2T_C)_2]^{2-}$ in the reaction with Na_2WO_4 and Na_2MoO_4.[5] Also, Na_2HAsO_4 forms a complex with oxalic acid which has the formula $[HAsO_3C_2O_4]^{2-}$ and a relative stability constant of log K = 5.50 at an ionic strength I = 0 and 25 °C.[6] With monobasic acids (HAc), *i.e.*, formic, acetic and propionic acid, $NaAsO_2$ forms $[AsOAc_2]^-$ complexes.[7] With the carbonate ion, it forms the $[As(OH)_2CO_3]^-$ complex, starting from the $As(OH)_3$ form of the As(III) acid.[8]

* Corresponding author. E-mail: ssunaric@medfak.ni.ac.yu
# Serbian Chemical Society member.
doi: 10.2298/JSC0811113O

All the above-cited results were obtained by pH and conductometric measurements and methods, as in this work.

However, no literature data exist on the complex formed between $NaAsO_2$ and oxalic acid.

According to literature data,[9,10] different forms of As(III) acids exist in aqueous solutions, *i.e.*, H_3AsO_3, $HAsO_2$, $As(OH)_3$, AsO(OH) and $H_3[As(OH)_6]$. The acids of As(III) have not been isolated as pure acids, liquid or solid. The dissociation constant of arsenite acid in the form of $HAs(OH)_4$ or $HAsO_2$, at 25 °C and the ionic strength $I = 0$, is $pK_1 = 9.22$, 9.08 or 9.3, depending on the author.[10] The theoretical calculated dissociation constant of $HAsO_2$ is $pK_1 = 10.01$ at 25 °C.[11] According to new data, pK_1 for H_3AsO_3 is 9.22 or 9.25 at 25 °C.[12] In alkaline solution, the *m*-arsenite ion, AsO_2^-, is present.[9]

The dissociation constants of $H_2C_2O_4$ are $K_1 = 5.6\times10^{-2}$ and $K_2 = 5.4\times10^{-5}$ at 25 °C and ionic strength $I = 0$.[13]

The aim of the present work was to investigate behavior of the $NaAsO_2$–oxalic acid system, in which As is trivalent. The inorganic forms of arsine are more toxic than its complex organic compounds, especially the trivalent form-arsenite. Arsenic compounds are present in the environment and in biological systems. For most humans, the greatest single exposure source is through food and water. Oxalic acid and oxalates are present in many plants and vegetables. Therefore, studies of reaction of arsenic compounds with oxalic acid can help in the understanding of the biogeochemistry, toxicity and metabolism of arsenic compounds.

EXPERIMENTAL

Apparatus

A Jenko pH-meter 6071, calibrated with Sigma buffers of pH 7.00 and pH 4.00, was used for the pH measurements. The conductivity was measured using a Hanna Instruments conductometer. The solutions were thermostated using a Sutjeska thermostat with temperature regulation ±0.1 °C.

Reagents and solutions

The oxalic acid ($H_2C_2O_4\cdot2H_2O$, Lafoma) solutions (0.20 mol dm^{-3}) were standardized by potentiometric titration with NaOH. The concentrations of the $NaAsO_2$ (Merck) solution (0.040 mol dm^{-3}) were determined gravimetrically. The NaCl solutions (2.5 mol dm^{-3}) were prepared by dissolving the required amount of dry NaCl (Merck). All reagents were of p.a. quality. The deionized water was used for preparation of the solutions.

For the determination of the composition of the complex using the Job method and by pH metric and conductometric measurements, solutions of $NaAsO_2$ and $H_2C_2O_4$ of initial concentration 0.020 mol dm^{-3} were prepared.

NaCl solutions of initial concentrations 2.5, 0.50 and 0.10 mol dm^{-3} were employed for maintaining the ionic strength of the solutions constant during the pH measurement.

For the pH-metric and conductometric titrations, $H_2C_2O_4$ and $NaAsO_2$ solutions of initial concentration 0.20 and 0.020 mol dm^{-3}, respectively, were used.

Measurements

For the conductometric and pH-metric titrations, a series of experimental solutions in volumetric flasks were made. Each of the solutions contained an aliquot of 0.20 mol dm^{-3} $H_2C_2O_4$ and 25 cm^3 of 0.020 mol dm^{-3} $NaAsO_2$. Deionized water was added to obtain a total volume of 50 cm^3.

The compositions of the complex formed from oxalic acid and $NaAsO_2$ was determined by the Job method[15] using the pH-metric and conductometric measurements described in previous papers.[4,6,7]

The base of these methods is the reaction of complex formation in which H of the ligand is a direct component of the reaction, as in the case of the oxalate complex with Na_2HAsO_4, *i.e.*, with $HAsO_4^{2-}$:

$$HAsO_4^{2-} + 2H^+ + C_2O_4^{2-} \rightarrow HAsO_3C_2O_4^{2-} + H_2O \quad (1)$$

which was cited in previously papers.[1,2,4-7] In this reaction, the change of the H^+ concentration, *i.e.*, pH, is a measure of the amount of formed complex. Also, a change of the solution conductivity is caused by a concentration change of the very mobile H^+, as well as of other ions, *i.e.*, the conductivity change is also a measure of the amount of complex formed.[4,6,7] Since in the reaction solution all the present H^+ exert an influence on the pH and on the conductivity, together with all the other ions present, the change of pH and of conductivity during Reaction (1) can be calculated using measurements of pH and conductivity of the following three solution systems:

a) x cm^3 of the initial $H_2C_2O_4$ solution and $(50 - x)$ cm^3 of the initial $NaAsO_2$ solution,
b) x cm^3 of the initial $H_2C_2O_4$ solution and $(50 - x)$ cm^3 of water and
c) $(50 - x)$ cm^3 of the initial $NaAsO_2$ solution and x cm^3 of water.

In the series of solutions a, b and c, x was varied from 5 to 45 cm^3. In order to calculate the relative stability constant of the complex, the experiments were performed at different ionic strengths. Measuring the pH values of the solutions for ionic strengths of 0.10, 0.20 and 0.50 mol dm^{-3}, Job curves were constructed. The initial solutions of $NaAsO_2$ and $H_2C_2O_4$ were 4.0×10^{-2} mol $dm^{-3}$and that of NaCl 0.50, 1.0 and 2.5 mol dm^{-3}, for the preparation of solutions with ionic strengths 0.10, 0.20 and 0.50 mol dm^{-3}, respectively. Three series of solutions systems were made:

d) x cm^3 $H_2C_2O_4$, 10 cm^3 NaCl and $(25 - x)$ cm^3 $NaAsO_2$,
e) x cm^3 $H_2C_2O_4$, 10 cm^3 NaCl and $(25 - x)$ cm^3 water and
f) $(x + 15)$ cm^3 water, 10 cm^3 NaCl and $(25 - x)$ cm^3 $NaAsO_2$.

In these solutions, x was varied from 2.5 to 22.5 cm^3 and deionized water was added to a final volume of 50 cm^3.

The pH and conductivity were measured after thermostating the solutions for 24 h at 25 °C. Also the pH values were measured for solutions with I = 0.10 mol dm^{-3}, at 20 and 30 °C, to determine the thermodynamic parameters of complex formation.

RESULTS AND DISCUSSION

The results given in Table I show that the solutions of the mixtures of $NaAsO_2$ and $H_2C_2O_4$ (a) have higher pH values than the corresponding $H_2C_2O_4$ solutions (b), analogous to reactions with other complexing agents, as well as oxalate, as explained in previous papers[4,6,7] and Reaction (1). The decrease in the H^+ concentration can be ascribed to the following reaction:

$$Na^+ + AsO_2^- + 2H^+ + C_2O_4^{2-} \rightarrow Na^+ + [AsOC_2O_4]^- + H_2O \quad (2)$$

A reaction occurs between $C_2O_4^{2-}$, AsO_2^- and H^+. This reaction can develop as a third-order reaction, but it is more probable that it develops as two second-order reactions.

TABLE I. pH and conductivity (χ) values of the solution mixtures: $NaAsO_2$ and $H_2C_2O_4$ (a), $H_2C_2O_4$ and H_2O (b) and $NaAsO_2$ and H_2O (c). Concentrations of the stock solutions: $c(H_2C_2O_4) = c([NaAsO_2) = 2\times10^{-2}$ mol dm^{-3}. Total volume: 50 cm^3; t = 25.0±0.1 °C

V / cm^3*	Solution					
	a		b		c	
	pH	χ / mS cm^{-1}	pH	χ / mS cm^{-1}	pH	χ / mS cm^{-1}
5	9.51	1.31	2.80	0.69	10.35	1.29
10	9.01	1.27	2.59	1.30	10.26	1.14
15	8.12	1.20	2.38	1.95	10.20	0.97
20	4.12	1.07	2.29	2.51	10.17	0.80
25	3.15	1.05	2.20	3.09	10.10	0.71
30	2.71	1.74	2.14	3.61	10.02	0.58
35	2.49	2.58	2.09	4.11	9.91	0.40
40	2.37	3.45	2.04	4.62	9.86	0.30
45	2.29	3.97	1.99	5.28	9.69	0.15

*Volume of the oxalic acid solution for mixtures a and b, and volume of deionized water for mixture c

The decrease in the H^+ concentration is proportional, according to Eq. (2), to the quantity of the formed complex and was calculated using the equation:

$$\Delta c(H^+) = c_a(H^+) - (c_b(H^+) + c_c(H^+)) \quad (3)$$

where $c_a(H^+)$, $c_b(H^+)$ and $c_c(H^+)$ are the H^+ concentrations in solutions a, b and c, respectively.

The change in conductivity, $\Delta\chi$, due to the formed H_2O was calculated according to the equation:

$$\Delta\chi = \chi_a - (\chi_b + \chi_c) \quad (4)$$

where χ_a, χ_b and χ_c are the conductivity of solutions a, b and c, respectively.

The dependencies of $\Delta c(H^+)$ and $\Delta\chi$ on the mole fraction of $H_2C_2O_4$ (x) are shown in Figs. 1 and 2, respectively. The Job curves have a maximum at x = 0.5, which indicates the formation of a complex in which the $C_2O_4^{2-}$:AsO_2^- ratio is 1:1. This result is in agreement with Eq. (2). The results obtained for complexes with monobasic acids (HAc) and $NaAsO_2$ in the literature,[7] indicate the formation of complexes in which molar ratio $NaAsO_2$:HAc is 1:2. In the case that only the neutralization reaction occurs:

$$NaAsO_2 + HAc \rightarrow HAsO_2 + Na^+ + Ac^- \quad (5)$$

the molar ratio for monobasic acids, $NaAsO_2$:HAc, must be 1:1 and for dibasic acid, such as oxalic, $NaAsO_2$:$H_2C_2O_4$, 1:0.5.

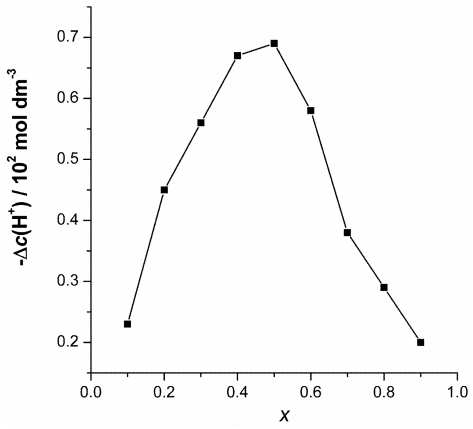

Fig. 1. Job curve obtained by pH-metric measurements.

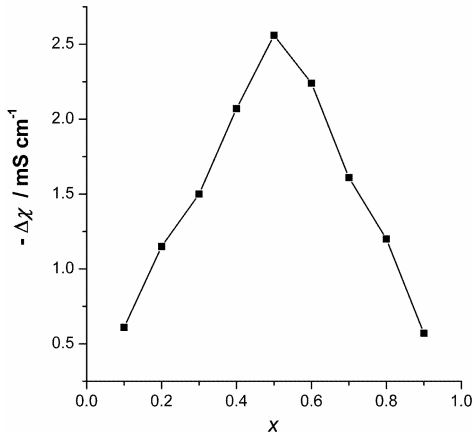

Fig. 2. Job curve obtained by conductometric measurements.

The results of the conductometric titration (Fig. 3) are in agreement with those obtained using the Job curve. An expressed equivalence point at the molar ratio $C_2O_4^{2-}$:$NaAsO_2$ of 1:1 was obtained, indicating the formation of the $AsOC_2O_4^-$ complex.

Second, not expressive, equivalent point which can be observed on the conductometric titration curve (Fig. 3) corresponds to the $NaAsO_2$:$H_2C_2O_4$ = 2:1 molar ratio. The 2:1 molar ratio corresponds to an existence an acid–base reaction:

$$2Na^+ + 2\,AsO_2^- + 2H^+ + C_2O_4^{2-} \rightarrow 2HAsO_2 + C_2O_4^{2-} + 2Na^+ \qquad (6)$$

i.e., the neutralization reaction; it is dominant in excess $NaAsO_2$ but negligible in excess $H_2C_2O_4$, due to complex formation.

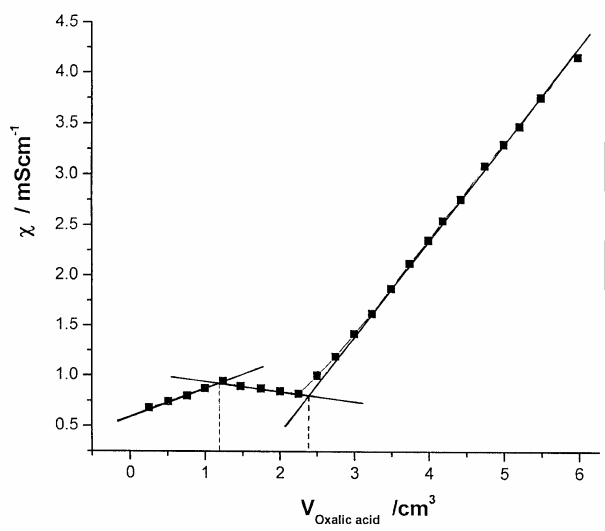

Fig. 3. Conductometric titration of 2.0×10^{-2} mol dm^{-3} $NaAsO_2$ (25 cm^3) with 2.0×10^{-1} mol dm^{-3} $H_2C_2O_4$.

The conductometric titration curve which shows a slight increase in the conductivity of the solution up to the first equivalence point ($V_{\text{oxalic acid}}$ = 1.25 cm^3), corresponding to the formation of the weakly dissociated arsenite acid, indicates the occurrence of this reaction. Since the $NaAsO_2$ salt was used, it is more likely that Reaction (6) occurs with $HAsO_2$.

The decrease in conductivity until the second equivalence point is a consequence of the formation of the $[AsOC_2O_4]^-$ complex, because the number of ions before and after the addition of oxalic acid remains practically the same, while the mobility of $[AsOC_2O_4]^-$ is smaller than that of AsO_2^-. After the second equivalence point, the conductivity of the solution increases because of the surplus $H_2C_2O_4$. If only the acid–base reaction had occurred, the conductivity of the solution would have started to increase immediately after the first equivalence point. The reaction of complex formation (Eq. (2)) is independent of the form of the arsenite acid.[9,10]

On the basis of the above discussion, it can be concluded that arsenite acid is formed when there is more $NaAsO_2$ than $H_2C_2O_4$, whereas a complex formation reaction occurs with increasing acid/arsenite ratio.

A pH-metric titration curve of a solution of $NaAsO_2$ with a solution of $H_2C_2O_4$ is shown in Fig. 4. The equivalence point on the curve occurs when the ratio $NaAsO_2$:$H_2C_2O_4$ is 2:1, which indicates the formation of arsenite acid. This means that, in addition to the complex formation reaction, a neutralization reaction also occurs. This reaction was also evidenced by the results of the conductometric titration.

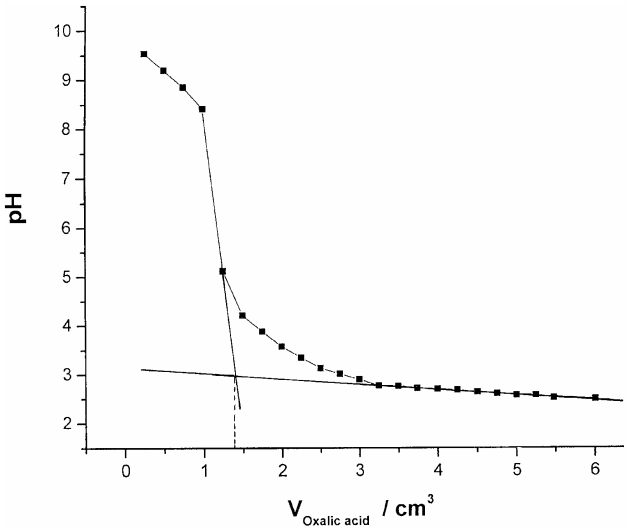

Fig. 4. pH-metric titration of 2.0×10^{-2} mol dm^{-3} $NaAsO_2$ (25 cm^3) with 0.20 mol dm^{-3} $H_2C_2O_4$.

The absence of a second equivalence point, corresponding to complex formation, indicate that the second dissociation constant of $H_2C_2O_4$, k_2, and the equilibrium constant, K_e, of the complex reaction have similar values, resulting

in a relatively long slope of the titration curve after the well-formed first equivalence point (Fig. 4).

Using the calculation method from previous papers[7,14,16–18] and the data obtained by pH measurements in solutions with a molar ratio $H_2C_2O_4$:$NaAsO_2 \geq 1$ ($pH \leq 2.9$), the relative stability constant of the complex was calculated using Eqs. (7)–(12) for different values of the ionic strength, regulated by the corresponding addition of a NaCl solution.

The equilibrium constant of the Reaction (2) is:

$$K_e = \frac{c(AsOC_2O_4^-)c(H_2O)}{c(AsO_2^-)c(C_2O_4^{2-})c(H^+)^2} = K_r \frac{c(H_2O)}{c(H^+)^2} \tag{7}$$

where K_r is the relative stability constant of the 1:1 complex ($[AsOC_2O_4]^-$).

The relative stability constant was calculated according to the equations for the total metal, ligand and H^+ concentrations and for the dissociation constants of the ligand:

$$c_0(H_2C_2O_4) = c(H_2C_2O_4) + c(HC_2O_4^-) + c(C_2O_4^{2-}) + c(AsOC_2O_4^-) \tag{8}$$

$$c(H^+) = c(HC_2O_4^-) + 2c(C_2O_4^{2-}) \tag{9}$$

$$c_0(AsO_2^-) = c(AsO_2^-) + c(AsOC_2O_4^-) \tag{10}$$

$$k_1 = \frac{c(HC_2O_4^-)c(H^+)}{c(H_2C_2O_4)} \tag{11}$$

$$k_2 = \frac{c(C_2O_4^{2-})c(H^+)}{c(HC_2O_4^-)} \tag{12}$$

The total stoichiometric concentrations are marked by the subscript "0".

The dissociation of $HAsO_2$ was neglected since the reaction of complex formation occurs between the arsenite oxygen and the oxalate ion, according to Eq. (2).

The equilibrium constant, K_e, according Eq. (7), depends of the H^+ concentration and can be calculated for the corresponding pH value.

The H^+ activity factor was calculated using the equation:

$$-\log f_{z_\pm} = 0.509z^2\left(\frac{\sqrt{I}}{1+\sqrt{I}} - 0.2I\right) \tag{13}$$

for the employed ionic strength, I.

The H^+ concentration was calculated from the pH and the H^+ activity factor and used for the calculation of the concentration of the corresponding ions and of the complex relative stability constant for three ionic strengths. On the basis of the average values of K_r, acquired from 5 repeated measurements at the given ionic strength of the solutions, on the temperature 25±0.1 °C, the relative stability

constant of the complex at $I = 0$, $K_{r,0}$, was graphically determined using the equation:

$$\log K_r = \log K_{r,0} - S\sqrt{I_c} \quad (15)$$

The obtained results are given in Table II ($\log K_{r,0} = 5.05$).

TABLE II. The average values of relative stability constants of the $[AsOC_2O_4]^-$ complex for different values of the ionic strength, I; $t = 25\pm0.1$ °C ; pH ≤ 2.9; *SD*: standard deviation

I	$(\overline{K}_r \pm SD)\times10^4$	$\log \overline{K}_r$
0.10	4.99±0.08	4.70
0.20	3.22±0.07	4.51
0.50	1.74±0.04	4.24

In order to determine the thermodynamic parameters of the complex, measurements of the pH of the solutions in which the $NaAsO_2$:$H_2C_2O_4$ ratio was 1:1 were made to make complex formation dominant. The thermodynamic parameters of the complex were calculated from the values of relative stability constants at 293, 298, and 303 K as the average value of three measurements. At constant ionic strength of 0.10 these values are $\Delta H = 10.5$ kJ mol^{-1}, $\Delta S = 133$ J mol^{-1} K^{-1} and $\Delta G = -29.0$ kJ mol^{-1} (298 K).

The obtained results are given in Table III and Fig. 5.

TABLE III. The average values of thermodynamic parameters for the complex reaction obtained from three measurements; $c(H_2C_2O_4) = c(NaAsO_2) = 4.0\times10^{-2}$ mol dm^{-3}, $I = 0.10$

T / K	ΔG / kJ mol^{-1}	ΔH / kJ mol^{-1}	ΔS / J mol^{-1} K^{-1}
293	–28.2	10.5	132
298	–29.0	10.5	133
303	–29.8	10.5	133

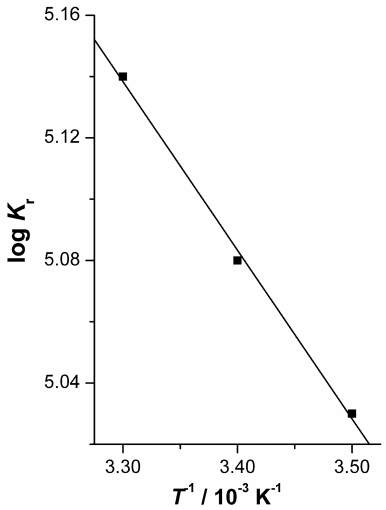

Fig. 5. Temperature dependence of the logarithm of the relative stability constant.

The obtained values for log K_r can be compared to the corresponding values for oxalate complexes of W(VI) (log K_r 7.52 and 6.45 at pH 4.55 and 5.55, respectively),[4] Mo(VI) (log K_r 7.29 and 5.60 at pH 4.55 and pH 5.48, respectively)[4] and As(V) (log K_r 4.85 and 4.56 at pH 3.07 and 2.97, respectively).[6] Since there is no significant difference in the log K_r values, it may be concluded that the interaction of the oxygen from the oxy anions and the H^+ ion from the acid has a greater influence on the reaction than the type of metal in the oxy anion.

ИЗВОД

КОНДУКТОМЕТРИЈСКА И pH-МЕТРИЈСКА ИСПИТИВАЊА РЕАКЦИЈЕ ОКСАЛНЕ КИСЕЛИНЕ И $NaAsO_2$

МИРЈАНА В. ОБРАДОВИЋ[1], СЛАВИЦА М. СУНАРИЋ[2], СНЕЖАНА С. МИТИЋ[1] и ДРАГАН С. ВЕСЕЛИНОВИЋ[3]

[1]Одсек за хемију, Природно–математички факултет, Вишеградска 33/224,Ниш,
[2]Одсек за фармацију, Медицински факултет, Булевар др Зорана Ђинђића 81, Ниш и
[3]Факултет за физичку хемију, п. пр. 550, Београд

Реакција $NaAsO_2$ са оксалном киселином испитана је мерењем pH и проводљивости, методом континуалне варијације и pH-метријским и кондуктометријским титрацијама. Нађено је да оксална киселина гради комплекс $[AsOC_2O_4]^-$. На основу pH-метријских мерења израчуната је релативна константа стабилности комплекса на 25±0.1 °C при јонским јачинама од 0,10 (log K_r = 4,70), 0,20 (log K_r = 4,51), 0,50 (log K_r = 4,24) и 0 (log $K_{r,0}$ = 5,05), као и термодинамички параметри реакције комплексирања на 25±0,1 °C (ΔH = 10,5 kJ mol^{-1}, ΔG = = –29,0 kJ mol^{-1}, ΔS = 133 J mol^{-1} K^{-1}).

(Примљено 10. јануара, ревидирано 15. маја 2008)

REFERENCES

1. M. V. Šušić, D. S. Veselinović, D. Ž. Sužnjević, *J. Serb. Chem. Soc.* **29** (1964) 311 (in Serbian)
2. M. V. Šušić, D. S. Veselinović, D. Ž. Sužnjević, *J. Serb. Chem. Soc.* **29** (1964) 121 (in Serbian)
3. D. Ž. Sužnjević, M. V. Šušić, D. S. Veselinović, *J. Serb. Chem. Soc.* **31** (1966) 221 (in Serbian)
4. M. V. Obradović, D. S. Veselinović, S. S. Mitić, *J. Serb. Chem. Soc.* **59** (1994) 669
5. D. S. Veselinović, M. Jelikić-Stankov, *Mikrochim. Acta* **1** (1989) 329
6. M. V. Obradović, S. S. Mitić, S. M. Sunarić, D. S. Veselinović, *J. Serb. Chem. Soc.* **64** (1999) 39
7. M. V. Obradović, D. S. Veselinović, S. S. Mitić, *J. Serb. Chem. Soc.* **60** (1995) 1135
8. C. S. Neuberger, G. E. Heltz, *App. Geochem.* **20** (2005) 1218
9. R. T. Sanderson, *Inorganic Chemistry*, Arizona State University, Reinhold Publishing Corporation, New York, 1967, p. 190
10. *Stability constants*, Special publication No. 17, The Chemical Society, London, 1964
11. V. P. Zakaznova-Herzog, T. M. Seward, O. M. Suleimonov, *Geochim. Cosmochim. Acta* **70** (2006) 1928
12. J. Raposo, J. Sanz, O. Zuloaga, M. Olazabal, J. Madariaga, *J. Sol. Chem.* **32** (2003) 253

13. M. V. Obradović, S. S. Mitić, D. S. Veselinović, D. C. Nasković, *J. Serb. Chem. Soc.* **63** (1998) 869
14. P. Job, *Ann. Chim*. **9** (1928) 113
15. M. V. Obradović, D. S. Veselinović, Z. Grahovac, *J. Serb. Chem. Soc.* **59** (1994) 21
16. M. V. Obradović, D. S. Veselinović, S. S. Mitić, *J. Serb. Chem. Soc.* **59** (1994) 1135
17. M. Jelikić-Stankov, D. Veselinović, *Analyst* **114** (1989) 719
18. R. A. Lindin, L. L. Andreeva, V. A. Molocka, *Spravochnik po neorganicheskoj khimii*, Khimiya, Moskva, 1987 (in Russian).

www.shd.org.rs

Journal of the Serbian Chemical Society

JSCS@tmf.bg.ac.yu • www.shd.org.rs/JSCS

J. Serb. Chem. Soc. 73 (11) 1123–1135 (2008) UDC 57.012.2.000.57:66.022.34.002.2:541.183
JSCS–3791 *Original scientific paper*

Microstructured surfaces engineered using biological templates: a facile approach for the fabrication of superhydrophobic surfaces

DUŠAN LOŠIĆ*

University of South Australia, Ian Wark Research Institute, Mawson Lakes Campus, Adelaide, SA 5095, Australia

(Received 2 March, revised 27 May 2008)

Abstract: The fabrication of microstructured surfaces using biological templates was investigated with the aim of exploring of a facile and low cost approach for the fabrication of structured surfaces with superhydrophobic properties. Two soft lithographic techniques, *i.e.*, replica moulding and nano-imprinting, were used to replicate the surfaces of a biological substrate. Leaves of the Agave plant (*Agave attenuate*), a cost-free biological template, were used as a model of a biosurface with superhydrophobic properties. The replication process was performed using two polymers: an elastomeric polymer, poly(dimethylsiloxane) (PDMS), and a polyurethane (PU) based, UV-curable polymer (NOA 60). In the first replication step, negative polymer replicas of the surface of leaves were fabricated, which were used as masters to fabricate positive polymer replicas by moulding and soft imprinting. The pattern with micro and nanostructures of the surface of the leaf possesses superhydrophobic properties, which was successfully replicated into both polymers. Finally, the positive replicas were coated with a thin gold film and modified with self-assembled monolayers (SAMs) to verify the importance of the surface chemistry on the hydrophobic properties of the fabricated structures. Wetting (contact angle) and structural (light microscopy and scanning electron microscopy) characterisation was performed to confirm the hydrophobic properties of the fabricated surfaces (> 150°), as well as the precision and reproducibility of the replication process.

Keywords: superhydrophobic surfaces; lotus-effect; replica moulding; nano-imprinting; *Agave attenuate*.

INTRODUCTION

The fabrication of three-dimensional (3-D) nanostructured materials exhibiting well-defined and controllable nanometre-scale features is one of the greatest challenges that has faced chemists and materials scientists in last two decades.[1] A

* Correspondence: e-mail, dusan.losic@unisa.edu.au
doi: 10.2298/JSC0811123L

wide range of very expensive fabrication techniques have been developed in the microelectronics industry, including deep and extreme UV photolithography, phase shift photolithography, electron beam writing, focused ion beam lithography and X-ray lithography.[2] To broaden the accessibility and diversify the capability of nanofabrication techniques, alternative, simple and cost-effective techniques, such as imprint lithography, soft lithography, capillary force lithography and polymer transfer printing, have been developed.[3–4] In particular, soft lithography, which is based on a soft polymer mould, such as poly(dimethylsiloxane) (PDMS), has been widely adopted for transferring patterns onto various surfaces and for the easy replication of complex nanostructures (replica moulding) with a variety properties. It has also been applied in the manufacture of electronic and microfluidic devices, optics and biosensors.[5–6]

Wettability is one of the fundamental properties of solid surfaces and controlling the wetting of surfaces is an important problem relevant to daily life, agriculture, industry and fundamental research.[7–9] It is generally accepted that superhydrophobic and self-cleaning properties are based on the hierarchical roughness of the surface on a micro and nano scale, combined with the chemistry of low surface energy compounds.[10–12] Water forms spherical droplets on such surfaces with a high contact angle (> 150°), and can easily roll of the surface taking with it dust particles.[1,10,13] Fabrications of synthetic superhydrophobic surfaces based on polymers, metals, metal oxides, carbon nanotubes and waxes, which mimic the properties of "lotus" surface, have been reported in recent years.[8,14–18] Electrochemical oxidation, chemical etching, chemical and electrochemical deposition, plasma etching, plasma deposition, laser ablation, chemical vapour deposition (CVD) and sol–gel processing were the techniques commonly employed.[14,19–21] The general approach of these methods was the fabrication of micro- to nano-structured surfaces combined with chemistry to decrease the surface energy. However, processing through many of these methods is expensive, time consuming, with problems of structural instability, difficulty in the control the formation of the structure and complexity of scale up.

Biological materials and processes are a relatively new source of inspiration for the design and fabrication of nano-structured materials.[22–23] Many organisms synthesize inorganic structures into intricate architectures with ordered micro-to--nano scale features, which cannot typically be replicated through laboratory synthesis. Therefore, the use of cheap biological materials as templates for the engineering of structures at the nano scale is a promising and cost effective fabrication strategy. The superhydrophobic and self-cleaning properties induced by surface roughness are widely adopted in nature, including plant leaves, butterfly wings, water strider legs *etc*.[8,24–25] Hundreds of different plants having the ability to completely clean their leaves from contamination (dust particle, spores and pathogens) by a simple rain shower or fog have been reported.[24–27] Among them, a

most impressive example is the Lotus plant (*Nelumbo nucifera*) the superhydrophobic properties of which were the first documented and named as the "lotus effect".[11]

In previous studies it was demonstrated that unicellular algae diatoms, as outstanding examples of micro- and nano-structured materials in nature, could be used as templates for nanofabrication.[28–31] The results revealed the possibility of the generation of multiple copies of diatoms based on a replication process that involved the use of the diatom nano-structured silica as a master mould and the transformation of their structure into polymers or metals with unique optical and separation properties.[28–30] In the present work, this bio-inspired approach was extended to the fabrication of micro- to nano-structured surfaces with larger dimensions using other biological substrates. The aim was to demonstrate a facile method by applying biological templates, such as plant leaves, for the rapid fabrication of artificial superhydrophobic surfaces. A schematic diagram of the fabrication is outlined in Fig. 1. The leaves of Agave plant (*Agave attenuate*) were used as a model of a structured biological template. The transference of the pattern of the leaf was performed using a soft-lithography approach with two replication steps for the production of negative and positive replicas using two polymers, *i.e.*, poly(dimethylsiloxane) (PDMS) and a UV-curable polyurethane (PU) polymer (NOA 60). The morphological and wettability properties of the surfaces of the plant and fabricated replicas were investigated using light microscopy, field emission scanning electron microscopy (SEM) and contact angle (CA) measurements.

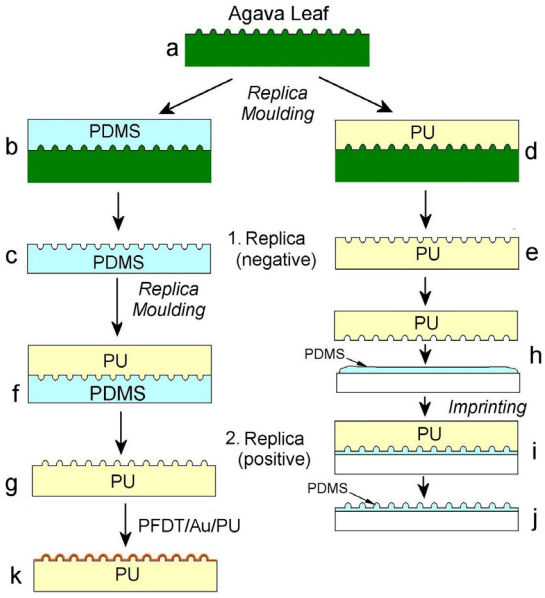

Fig. 1. Schematic outline of the fabrication of highly hydrophobic surfaces by replication from biological templates (Agave leaves). In the first step, the replica moulding process using Agave leaf surface (a) to fabricate negative replicas with two different polymers including PDMS (b–c) and PU polymer (d–e). In the second step, the negative replicas were used to fabricate positive replicas: PDMS was used for the preparation of PU positive replica (f–g) and PU for the preparation of PDMS positive replica where the imprinting process was applied (h–i–j). The positive PU replicas were coated with a thin gold film and modified with 1*H*,1*H*,2*H*,2*H*-perfluorodecanethiol (PFDT) (k) to improve their hydrophobic properties.

EXPERIMENTAL

Materials

The leaves from Agave plant (*Agave attenuate*) were freshly collected from local garden (Flinders University Campus, Adelaide, South Australia). To remove possible contaminants, leaf samples were cleaned by running water, followed by rinsing with a stream of nitrogen. A minimum of 50 mm×50 mm square areas of leaf were cut from several different regions and the top side of the plant surface was used as a template for the replications. The poly(dimethylsiloxane) PDMS replicas were prepared from polymer precursor (Sylgard 184 parts A and B) purchased from Dow Corning (USA). The polyurethane based (mercapto ester type) UV--curable polymer (NOA 60) was obtained from Norland Inc. (USA). 1*H*,1*H*,2*H*,2*H*-Perfluorodecanethiol (PFDT) was supplied from Aldrich (Australia).

Fabrication

The replication process, which combined two soft-lithographic methods, *i.e.*, replica moulding and nano-imprinting, is schematically shown in Fig. 1. In the first step, replica moulding or master processing was performed to replicate the leaf surface (Fig. 1a) into negative replicas using two polymers, *i.e.*, PDMS (Figs. 1b–1c) and UV-curable PU (Figs. 1d–1e). In the second step, both negative replicas were used as masters for the fabrication of the corresponding positive replicas to match the topography of the original plant surface. A replica moulding process was used to prepare a PU positive replica (Figs. 1f–1g) using the PDMS negative replica as the master (Fig. 1c) and a nano-imprinting method was applied to fabricate PDMS positive replicas (Figs. 1h–1j) using a hard PU negative replica as the stamp (Fig. 1e).

The replica moulding fabrication process was adopted from previous studies.[5,28] Briefly, degassed poly(dimethylsiloxane) PDMS prepolymer (Sylgard 184 part A, base) was mixed with a cross-linking catalyst (Sylgard 184 part B, a curing agent which consists of dimethyl, methylhydrogen siloxane) at a 10:1 (w/w) ratio, then poured carefully over leaf samples and cured for at least 6 h at 60 °C. After curing, the cross-linked elastomeric PDMS was peeled from the surface and cleaned by sonication, water, and ethanol to remove any remains of the leaf (Figs. 1b–1c). A second negative replica was prepared by pouring UV-curable prepolymer (NOA 60) over leaf samples and curing under a UV lamp (λ = 365 nm). The precuring process was carried out for 20 min followed by postcuring for at least 3 h. The polymer mould was then peeled off the leaf, yielding the negative relief of the initial leaf surface (Figs. 1d–1e). The negative replicas were cleaned and reused for repeated replications.

A PU positive replica (Figs. 1f–1g) was prepared from a PDMS negative replica (Fig. 1c), which was the mould (master). A PDMS positive replica was prepared by nano-imprinting using a PU negative replica (Fig. 1e) as the stamp employing a previously described procedure.[32] Briefly, the precured PDMS was uniformly dispersed on glass or another supporting substrate. A small pressure of the stamp was applied on the PDMS film after an initial curing for 2 h at room temperature. This was followed by complete curing for at least 8 h at 40 °C (Figs. 1h–1j). When the curing process was completed, the PDMS film was separated from the stamp (Fig. 1j). A thin gold film (≈ 10 nm) was deposited on the positive polymer replica made of PU using the sputter deposition system (Anatech, USA). The gold-coated replica samples were modified with a self-assembled monolayer of 1*H*,1*H*,2*H*,2*H*-perfluorodecanethiol (PFDT) by keeping the samples in 5 mM PFDT solution for 30 min, followed by gentle rinsing with ethanol and drying with a stream of nitrogen.[33]

Characterisations

The static contact angles of water drops on the samples of the leaf surfaces and their replicas were determined with a custom-built contact angle goniometer. Cut samples of 1 cm^2 were affixed to a glass slide and a 5 μl droplet of high purity water (resistivity 18 MΩ cm) was applied to the surface. After 30 s, the droplets had equilibrated; digital images of the drop profile (624×580 pixels, 8-bit monochrome) were captured with a progressive scan CCD camera (JAI CVM10BX). The contact angle was determined by in-house edge detection software by drawing a tangent close to the edge of the droplet. The mean value of the obtained contact angles was calculated from at least 10 individual measurements taken from different locations on the examined substrates. Measurements were made at 22 °C and 40–50 % RH.

An optical microscope (Nikon) with a colour CCD camera and colour monitor, as part of the Nanoscope IV, Multi Mode AFM system (Veeco, USA), was used for primary surface observation of all the fabricated samples. Photographic images were taken by a camera connected to the microscope and a PC. More details of the surface morphology of the prepared samples were obtained by field-emission scanning electron microscopy, Philips XL 30 microscope. The samples were mounted on microscopy stubs with a carbon sticky tape and coated with a thin sputtered platinum layer (3–5 nm) to provide a conducting surface. The SEM images were acquired with accelerating voltages from 5–10 kV.

RESULTS AND DISCUSSION

Morphological and hydrophobic characteristics of Agave plant surface

Agave attenuate, a succulent plant from the large *Agavaceae* family, known as “lion’s tail”, “swan’s neck”, or “foxtail” is one of the most attractive ornamental plants in indoor and outdoor gardens (Fig. 2a). The plant produces large giant rosettes with smooth and pale green leaves of average size of about 10–20 cm in width and 50–80 cm in length. Water droplets in contact with the leaf surface form nearly spherical beads, as shown in Fig. 2b (inset). The static contact angle of a water drop placed on the leaf surface was measured as 155±3°, which confirms their superhydrophobic properties. The water drops easily roll off the surface and the leaf remains completely dry even during rain, suggesting a very low sliding angle and excellent water-repellence. Experiments with powder dirt particles dispersed on leaf surface demonstrated that particulate contaminants could be easily picked up by these water droplets and removed from the leaves when the water droplets roll off, thus showing their self-cleaning properties. The wetting properties of *Agave attenuate* plants have not hitherto been investigated. Hence, this study for the first time provides evidence of their superhydrophobic and self-cleaning properties.

The surface of *Agave attenuate* leaves were characterised by SEM and typical images are presented in Fig. 2c. The images from both sides of the leaf show the same characteristic hill-like topography with structures that represent papilose epidermal cells responsible for the formation of the micro- and nano-structures of the cells. The cells have a hexagonal geometry of irregular size, in range of 20–50 μm. A circular structure, called papillae, with a diameter of 10–15 μm

and an elongated shape was observed on the middle of the each cell (Fig. 2c, inset 1). These structures were surrounded with numerous, irregularly oriented, smaller crystal-like structures (short ribbons) that were dispersed as brushes across the cell surface (Fig. 2c, inset 2). Their average size was estimated to be several hundred nm wide and a few μm long. They most likely represent wax nanocrystals, which in many plants are made from highly hydrophobic organic compounds.[34] The results presented here confirm that the Agava leaf possesses a two-scale structured surface, suggesting their ability to act as a good substrate for replication and the fabrication of artificial superhydrophobic surfaces.

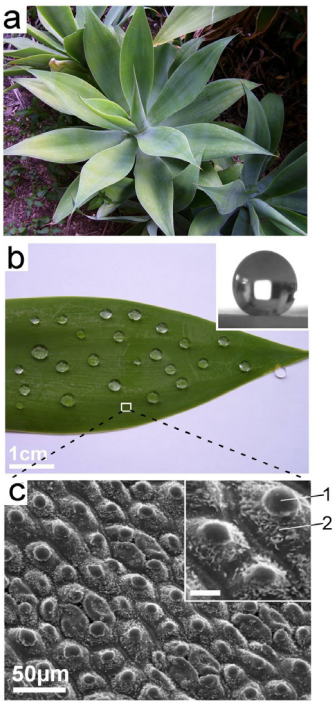

Fig. 2. *Agave attenuate* plant in a garden (a), a plant leaf with water droplets (b), illustrating excellent water repellent and hydrophobic properties and low and high resolution SEM images (c) showing the typical topography of the plant surface, with microstructured features (papilla) (line 1) and nano-structured wax crystals (line 2) marked in the inset.

Morphological and hydrophobic characteristics of the replicated films

Low magnification light microscopy images of the leaf surface and the fabricated replicas with their corresponding contact angle measurements are shown in Fig. 3 and Table I, respectively. Images of the plant surface (Fig. 3a) show an array of sculptured microstructures of epidermal cell, which represent papillae structures, seen in greater detail on previous SEM images (Fig. 2c). Images of the negative polymer replicas (PDMS and PU) prepared by replica moulding are presented in Figs. 3b–3c. The structures seen on the images represent the epidermal cells with papillae structures as holes or depressions on the surface, which are not clearly recognised by optical microscopy. No morphological differences were seen

between the two replicas made from different polymers, which was additionally confirmed by SEM. However, a considerable difference is observed in their static CA values. The water drop on the PU polymer replicas shows a lower CA (113±6°) (Fig. 3c, inset) than on the PDMS replicas (132±8°) (Fig. 3b, inset). This disagreement is explained by the difference in the chemical composition and differences in the surface energy of these two polymers.

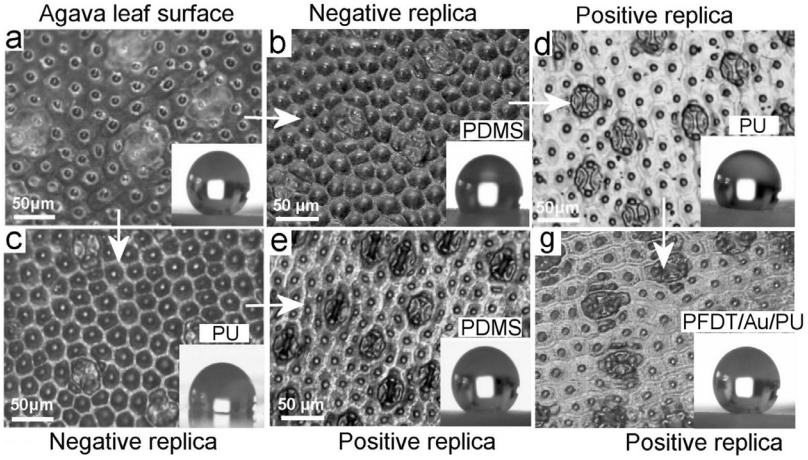

Fig. 3. Low resolution light microscopy images of Agave leaf surface and the corresponding replicas. Typical topography of the leaf surface with papillae microstructures (a); PDMS (b) and PU (c) negative polymer replicas fabricated by replica moulding process of the leaf; positive PU replica fabricated from PDMS (d); positive PDMS replica fabricated by imprinting using PU negative replica as a stamp (e); positive PFDT/Au/PU replica fabricated by coating with a thin gold film modified with 1*H*,1*H*,2*H*,2*H*-perfluorodecanethiol (g). The images of water droplets on all surfaces are presented (right bottom on each image) to quantify their hydrophobic properties.

TABLE I. Values of the static contact angles (mean values±*SD*) measured on Agave leaves, the corresponding negative and positive polymer replicas (PDMS, PU and PFDT/Au/PU) and the corresponding control flat substrates

	Leaf surface	Negative replica		Positive replica			Control (flat surfaces)		
		PDMS	PU	PDMS	PU	PFDT/Au/PU	PDMS	PU	PFDT/Au/PU
Contact angle, deg.	155±3	132±8	113±6	150±6	135±6	152±5	120±5	95±4	118±3

Images of the positive polymer replicas prepared with both polymers (PDMS and PU) are presented in Figs. 3d–3e. The characteristic topography and the cell structures corresponding to the original leaf surface, seen in Fig. 3a, are observed. Again, no morphological differences in these positive replicas were seen between two polymers (Figs. 3d–3e) but a considerable difference was observed in their CA values. The PU positive replica showed a lower CA (135±6°) in comparison with the PDMS positive replica (150±6°), which is caused by the differ-

rences in their surface energies. The very similar CA value of the PDMS replica to that of the original leaf surface (155±3°) clearly demonstrates that it is possible to fabricate a surface with highly hydrophobic properties by a simple and reliable replication of a plant surface. To demonstrate that the hydrophobic properties of the positive replicas are dependent on the surface chemistry, PU replicas were coated with a thin gold film and modified with a self-assembled monolayer of 1*H*,1*H*,2*H*,2*H*-perfluorodecanethiol. A significant increase in the CA value from 135±6 to 152±5° was observed and the hydrophobic properties matched those of the original plant. These results clearly show that modifications using molecules with a lower surface energy increase the contact angle of the surface, which confirms that surface modification is a practical method to alter the wetting properties of a structured surface to obtain the desired hydrophobic properties.

To characterise the precision of the replication process, more detailed SEM images of the fabricated replicas were obtained, which are presented in Figs. 4a–4i. The characteristic topography of the Agave leaf surface with the hierarchical organisation of the structures, which includes the circular papillae microstructures (1) and nanostructured wax crystals (2), is presented in Figs. 4a–4c. The SEM images of the corresponding PU polymer replica are shown in Figs. 4d–4f. The epidermal cell and the 3-dimensional papillae structures seen on the leaf surface (Figs. 4a–4c) were replicated as hexagonal depressions with large circular holes in the middle. The large circular holes (Figs. 4e–4f, line 1) represent the replica of the papillae microstructures (Fig. 4c, line 1). The smaller holes and protrusions around the big holes (Fig. 4e, line 2) represent replicas of the wax nanostructures (Fig. 4c, line 2). The images of the corresponding positive replica (PDMS) fabricated by imprinting using a negative PU replica (Figs. 4d–4f) are presented in Figs. 4g–4i. It is evident that both papillae microstructures (Fig. 4i, line 1) and wax nanostructures (Fig. 4i, line 2) from leaves had been successfully and with excellent precision replicated into PDMS. However, there are a few minor variations in comparison with the original leaf surface. The slightly curved shape of epidermal cells seen on original leaves (Figs. 4a–4b) and positive replica (Figs. 4g–4h) was not fully preserved in the positive replica. In addition, the smaller wax crystal structures were replicated with a lower density around the papillae structures than in the original plant surface, which is not surprising because of the limitations of using PDMS polymers to replicate nanostructures smaller than 50 nm. The slightly lower density of these nanostructured replicas from wax structures observed on both replicas may explain the slight disagreement in the CA between the PDMS polymer replicas (150±6°) and the original plant surface (155±3°).

A schematic model of the surface structures of the plant surface and the corresponding replicas based on SEM images is shown in Figs. 5a–5c to understand better their hydrophobic properties. The two scale geometry and double rough-

ness with micron (papillae) and nano-sized (wax) structures from the leaf surface (Fig. 5a) are replicated into the corresponding negative replica (Fig. 5b) and fully preserved within the positive replica (Fig. 5c). According to both Wenzel and Cassie–Baxter theories, a double roughness surface greatly amplifies the apparent contact angle.[11,12]

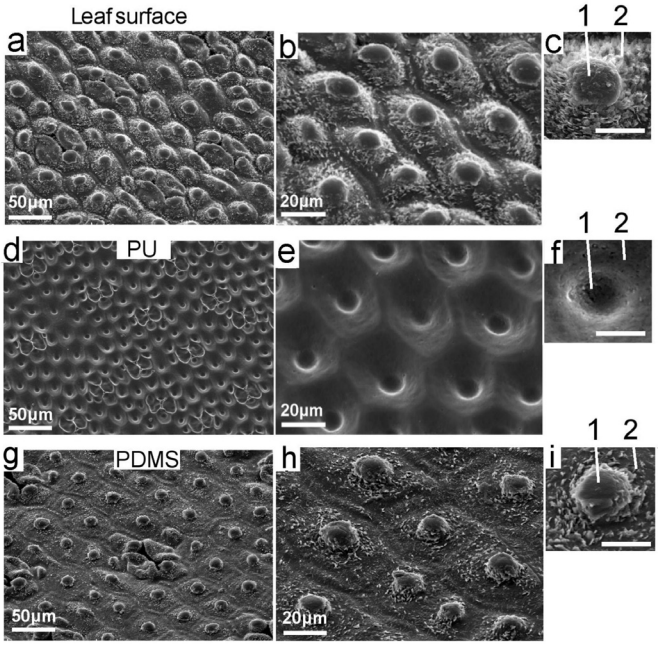

Fig. 4. SEM Images of Agave leaf surface and the corresponding replicas showing the replication process in more detail. Leaf surface(a–c), PU negative (d–f) and PDMS positive (g–i) replicas. Papillae structures with micro (1) and nanofeatures (2) are marked.

In the Wenzel approach, it is assumed that liquid drop fills both the peaks and valley of the rough surface (Fig. 5d). From an energy consideration, the apparent contact angle of the drop θ_w is given by the equation:

$$\cos \theta_w = r \cos \theta \tag{1}$$

where r is the ratio of the actual area of the liquid–solid contact to the projected area on the horizontal plane and θ is the equilibrium contact angle of the liquid drop on a flat surface.

According to the Cassie–Baxter theoretical model, the formation of a spherecal droplet of water on a surface is explained by the state in which air bubbles are trapped in the surface structures and the water drop sits on the bubbles (Fig. 5e). This model assumed that the water drop settles on the peaks of the roughness geometry with the contact angle given by the equation:

$$\cos \theta_{CB} = f_s \cos \theta + f_s - 1 \tag{2}$$

where f_s is the fraction of projected planar area of the drop in contact with a solid. In the limit of $f_s \rightarrow 0$, the contact angle θ_{CB} approaches 180° leading to super hydrophobic behaviour.

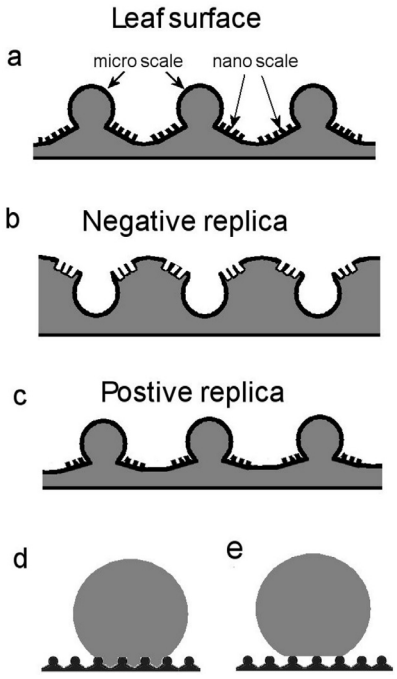

Fig. 5. Model of the two scale structured surface of leaf (a) and the prepared replicas (b–c) showing their micro and nanostructures. Schematic drawing (d, e) of a drop in contact with a surface (a or c) according to the Wenzel and the Cassie–Baxter model.

A significant increase of the CA of fabricated replicas in comparison with flat surface (PDMS, PU and PFDT/Au/PU, Table I) was observed, which clearly demonstrates the central importance of the roughness in the amplification of contact angles. The difference in the CA of the positive replicas with the same topography can be explained by differences in their chemical composition and surface chemistry, which are also important factors defining the CA. The differences in surface energy of PDMS (≈ 20 mN m^{-1}) and PU polymers (≈ 40 mN m^{-1}) is confirmed by the differences in the CA of their flat surfaces.[34,35] However, if it is assumed that the equilibrium CA of water on paraffin waxes is about 110°, which is lower than that for PDMS (120°) and PFDT (118°), then their positive replicas should have a higher CA than agave leaf.[37] This disagreement is explained by the imperfection of the replications of the nano-sized wax structures, previously noted on the SEM images (Fig. 4), which slightly lowered their CA values.

The advantage of this fabrication method in comparison to previous studies where only PDMS was applied is the straightforward separation in both replica-

tion steps (moulding or imprinting), which does not require the application of an anti-stick layer.[38] Experiments with PDMS and an anti-stick agent, could not provide satisfactory and reproducible results, as was also reported in a previous study.[38]

To achieve anti-stick free separation, in this work two polymers with different mechanical (elastic *vs*. hard) and chemical properties were applied, which makes the separation process simple and easy. Additional benefits obtained when using two polymers is the increased flexibility in fabrication and the ability to combine moulding and imprinting techniques. In comparison with the replication of plant leaf surfaces using the recently reported metal and electroforming process, this process with hard polymers is advantageous because polymer moulding is a cheaper, shorter and simpler process.[39] Regarding the robustness of the PU polymer, the prepared negative replica could be reused as a replication master or stamp many times and was comparable to the metal mould. To investigate their robustness for mass fabrication, the replication process using PU negative replicas was repeated several times and no morphological differences were observed in the SEM images of the fabricated positive replica after the moulding and imprinting process. Therefore, the proposed method has potential for application in the mass-production replication of highly hydrophobic surfaces from plant leaves with dimensions possibly exceeding 10 cm×10 cm. The hard polymer replica also has potential to serve as a master for the replication of leaves surface to other materials, including metals, metal oxides and carbons.

To demonstrate the self-cleaning properties of the fabricated polymer films, a larger area (150 mm×150 mm) of a PDMS positive replica was prepared on glass by subsequent imprinting using a PU negative master. The prepared surface was contaminated by alumina particles (size ≈ 1 μm) and then a qualitative self--cleaning test was performed by exposure to artificial rain at an inclination angle of 15°. The water droplets washed away and removed the particles from the surface in a comparable way to natural Agave leaves, which proves the self-cleaning properties of the prepared polymer films. The thin PDMS film could be removed from the underlying glass surface and attached to other substrates which have potential for water repelling applications on specific surfaces (including curved surfaces).

CONCLUSIONS

Two soft lithographic approaches, replica moulding and nano-imprinting were explored for the fabrication of polymer films with microstructured patterns and superhydrophobic properties by replication from plant surfaces (*Agave attenuate*). The replication process using two polymers with different chemical and mechanical properties, *i.e*., elastomeric PDMS and hard, UV-curable, polyurethane based (NOA 60) polymer, was demonstrated. It was shown that the fabricated polymer replicas matched the hierarchical topography of the plant surface

with excellent precision, providing accurate replication of their micro and nanostructures and highly hydrophobic properties, close to those of the original plant. Hydrophobic properties of fabricated replicas were influenced by the surface chemistry of the polymers selected for replication. However, it was shown that these properties could be controlled by further surface modifications of the polymer using self-assembled monolayers based on gold/alkanethiol surface chemistry.

The described method is simple, based on low cost, commercially available materials with the capability to be adapted for rapid and mass fabrication of superhydrophobic and self-cleaning surfaces for use in a variety of applications. The advantages of the method in comparison with existing replication methods were demonstrated. In addition to water repellence, other properties such as transparency, colour, flexibility, anisotropy and breathability could be incorporated into the fabricated superhydrophobic surfaces using these polymers.

Acknowledgments. The financial support from the Australian Research Council (ARC) and the University of South Australia is gratefully acknowledged.

И З В О Д

ПРОЈЕКТОВАЊЕ МИКРОСТРУКТУРИРАНИХ ПОВРШИНА КОРИШЋЕЊЕМ БИОЛОШКИХ МАТРИЦА: ЈЕДНОСТАВАН ПОСТУПАК ИЗРАДЕ СУПЕРХИДРОФОБНИХ ПОВРШИНА

ДУШАН ЛОШИЋ

University of South Australia, Ian Wark Research Institute, Mawson Lakes Campus, Adelaide, SA 5095, Australia

Проучавано је добијање микроструктурираних површина коришћењем биолошких шаблона са циљем да се испита лак и јефтин начин за производњу структурираних површина суперхидрофобних својстава. Да би се добиле реплике из биолошког подлога коришћене су две мекане литографске технике, ливење реплике и нано-утискивање. Лишће биљке Агава (*Agave attenuate*), бесплатна биолошка матрица, употребљено је као модел суперхидрофобне био-површине. Реплика је формирана коришћењем два полимера: еластомерни полимер, пол(диметилсилоксан) (PDMS) и полиуретан (PU) на бази UV осетљивог полимера (NOA 60). У првој фази прављења реплике са површине листа узети су негативи полимерних реплика, који су коришћени као оригинали за добијање позитива полимерних реплика ливењем или меканим утискивањем. Микро- и нано-структуре калупа са површине листова поседују суперхидрофобна својства, што је успешно реплицирано у оба полимера. Најзад, позитиви реплика превучени су танким филмом злата и модификовани самоуређујућим монослојевима (SAMs) да би се потврдио значај хемије површине за хидрофобна својства добијених структура. Одређивањем контактног угла и применом оптичке и електронске скенирајуће микроскопијом окарактерисани су овлаживање и структура, да би се потврдила хидрофобна својства добијених површина (>150°) и прецизност и репродуктивност репликације.

(Примљено 2. марта, ревидирано 27. маја 2008)

REFERENCES

1. M. Geissler, Y. N. Xia, *Adv. Mater.* **16** (2004) 12469
2. M. J. Madou, *Fundementals of Microfabrication,* CRC Press, Boca Raton, FL, 1997

3. Y. Xia, G. M. Whitesides, *Angew. Chem. Int. Ed. Engl.* **37** (1998) 550
4. Y. Xia, J. A. Rogers, K. E. Paul, G. M. Whitesides, *Chem. Rev.* **99** (1999) 1823
5. Y. Xia, G. M. Whitesides, *Annu. Rev. Mater. Sci.* **28** (1998) 153
6. B. D. Gates, Q. Xu, J. Love, D. B Wolfe, G. M. Whitesides, *Annu. Rev. Mater. Res*. **34** (2004) 339
7. D. Quere, *Rep. Prog. Phys.* **68** (2005) 2495
8. T. L. Sun, L. Feng, X. F. Gao, L. Jiang, *Acc. Chem. Res*. **38** (2005) 644
9. A. Lafuma, D. Quere, *Nat. Mater.* **2** (2003) 457
10. M. L. Ma, R. M. Hill, *Curr. Opin. Coll. Inter. Sci.* **11** (2006) 193
11. W. Barthlott, C. Neinhuis, *Planta* **202** (1997) 1
12. A. B. D. Cassie, S. Baxter, *Trans. Faraday Soc.* **40** (1944) 566
13. R. Blosey, *Nat. Mater.* **2** (2003) 301
14. H. Y. Erbil, A. L. Demirel, Y. Avci, O. Mert, *Science* **299** (2003) 1377
15. K. K. S. Lau, J. Bico, K. B. K. Teo, M. Chhowalla, G. A. J. Amaratunga, W. I. Milne, G. H. McKinley, K. K. Gleason, *Nano Lett.* **3** (2003) 1701
16. H. M. Shang, Y. Wang, K. Takahashi, G. Z. Cao, D. Li, Y. N. Xia, *J. Mater. Sci*. **40** (2005) 3587
17. X. D. Wu, L. J. Zheng, D. Wu, *Langmuir* **21** (2005) 2665
18. Z. G. Guo, J. Fang, J. C. Hao, Y. M. Liang, W. M. Liu, *Chem. Phys. Chem* **7** (2006) 1674
19. M. N. Qu, B. W. Zhang, S. Y. Song, L. Chen, J. Y. Zhang, X. P. Cao, *Adv. Funct. Mater.* **17** (2007) 593
20. M. T. Khorasani, H. Mirzadeh, Z. Kermani, *Appl. Surf. Sci.* **242** (2005) 339
21. L. Huang, S. P. Lau, H. Y. Yang, E. S. P. Leong, S. F. Yu, S. Prawer, *J. Phys. Chem. B* **109** (2005) 7746
22. B. Man, G. A. Ozin, *Nature* **382** (1996) 313
23. M. Sarikaya, C. Tamerler, A. K.-Y. Jen, K. Scholten, F. Baneyx, *Nat. Mater.* **3** (2003) 577
24. C. Neinhuis, W. Barthlott, *Ann. Bot.* **79** (1997) 667
25. H. Bargel, K. Koch, Z. Cerman, C. Neinhuis, *Funct. Plant Biol.* **33** (2006) 893
26. A. Otten, S. Herminghaus, *Langmuir* **20** (2004) 2405
27. B. Bhushan, Y. C. Jung, *Nanotechnology* **17** (2006) 2758
28. D. Losic, J. G. Mitchell, R. Lal, N. H. Voelcker, *Adv. Funct. Mater.* **17** (2007) 2439
29. D. Losic, J. G. Mitchell, N. H. Voelcker, *Chem. Commun.* **39** (2005) 4905
30. D. Losic, J. G. Mitchell, N. H. Voelcker, *New J. Chem*. **30** (2006) 908
31. D. Losic, G. Rosengarten, J. G. Mitchell, N. H. Voelcker, *J. Nanosci. Nanotechnol.* **6** (2006) 982
32. Y. S. Kim, N. Y. Lee, J. R. Lim, M. J. Lee, S. Park, *Chem. Mater.* **17** (2005) 5867
33. D. Losic, J. G. Shapter, J. J. Gooding, *Aust. J. Chem.* **54** (2001) 643
34. Norland products, Norland Optica Adhesive 60, http://www.norlandprod.com/adhesives.html, (October 13, 2008)
35. A. D. Tserepi, M. E. Vlachopoulou, E. Gogolides, *Nanotechnology* **17** (2006) 3977
36. R. Furstner, W. Barthlott, C. Neinhuis, P. Walzel, *Langmuir* **21** (2005) 956
37. N. A. Patanakar, *Langmuir* **20** (2004) 8209
38. M. H. Sun, C. X. Luo, L. P. Xu, H. Ji, O. Y. Qi, D. P. Yu, Y. Chen, *Langmuir* **21** (2005) 8978
39. S. M. Lee, T. H. Kwon, *Nanotechnology* **17** (2006) 3189.

www.shd.org.rs

Journal of the Serbian Chemical Society

JSCS@tmf.bg.ac.yu • www.shd.org.rs/JSCS

J. Serb. Chem. Soc. 73 (11) 1137–1138 (2008)
JSCS–3792

UDC *Mendeleev 54(083):930
Book review

BOOK REVIEW

THE PERIODIC TABLE
Its story and its significance

Author: ERIC R. SCERRI

Published by Oxford University Press, 2007. ISBN 0-19-530573-6

(Received 8 October 2008)

The book was written on the jubilee of the 100 years of the death of Dimitrii Mendeleev.*

The book has 346+12 pages, including an Index and Notes collected at the end of the book. The text is divided into ten chapters, covering a very broad selection of facts and ideas.

Eric Scerri is a well known historian and philosopher of science. This book is a large achievement in his work, covering both of his interests. The philosophy and history of chemistry and physics are interlaced throughout the book. It is shown how the abstract definitions of substance and element influenced the advent and subsequent development of the Periodic Table. To the same extent, the underlying information in the Periodic Table prompted a change of philosophical paradigm, too.

For the chemist's community, the book has multiple significances. As a history book, it presents in great details several less successful attempts to organize knowledge about chemical elements. It may give the impression that the works of Charles Gerhardt, Alexandre Emille Beguyer de Chancourtois, John Newlands, William Odling, Gustavus Hinrics and Julius Lothar Meyer are presented in too much details. However, at the end, they serve to emphasize the importance of the philosophical standpoint of Mendeleev, as a key factor that enabled his successful building of the Periodic Table and his marvelous predictions of yet undiscovered elements. The definition of elements as the Basic Substances (not Simple Substances), accepted by Mendeleev, was in recent history challenged several times but it has proved its value.

For all chemists, it will be of interest to find a very simple account of the basic facts in quantum mechanics, which are highly exploited in the explanation of chemical findings. In majority of chemistry (text)books, the presentation of

* 2007 was also the jubilee year of the Serbian Chemical Society – 110th anniversary.

quantum mechanical theories concerning bonding, and structure of atoms and molecules is usually given as a set of bare statements. In a concise manner, all of it is here truly explained. After reading this book, many will reconsider their understanding of orbitals, the Pauli principle, *etc*.

In this book, I admire the interesting passages about the (non)reduction of chemistry to physics. The underlying conclusion is that this question belongs to philosophy, not to science. It is also shown that the chemist's view that elements exist in compounds cannot be denied on experimental grounds.

The book is easy to read for anyone who has elementary knowledge of chemistry and physics. Hence, it can be of interest to anyone who wants to know more on the significance of the Periodic Table. It is valuable for students and teachers in sciences, as well as in the philosophy, and any other discipline that has some reference to chemistry.

Ivan Juranić[#], Professor
Faculty of Chemistry
University of Belgrade, Serbia

[#] Serbian Chemical Society member.